THE EFFECTS OF CURVATURE ON TURBULENT MIXING LAYERS

Thesis by

Chiun Wang

In Partial Fulfillment

of the Requirements for the Degree of

Doctor of Philosophy

California Institute of Technoloty

Pasadena, California

1984

(Submitted 21 May 1984)

To my parents

ACKNOWLEDGMENTS

The author gratefully acknowledges the guidance of his advisor, Professor Donald Coles, who offered generous, invaluable assistance throughout the author's work.

The author is indebted for the help and encouragement rendered by Professor Anatol Roshko. He also wishes to extend his thanks to Dr. Garry Brown, who introduced the author to the subject.

Special thanks are to Mrs. Kathy Eriksen for organizing and typing the manuscript.

Financial support for this work was provided by the Office of Naval Research through contract No. N00014-76-C-2060.

ABSTRACT

Experimental studies have been conducted in a curved mixing layer in which both the velocity ratio and the density ratio were variable. Flow visualization studies and profile measurements covered a wide range of experimental conditions. The structures observed experimentally were examined in the light of three different instability mechanisms which can exist in the same mean flow.

For the case of mixing layers with uniform density, it was found that the normal large spanwise vortex structures can be weakened or inhibited by Taylor-Görtler instability if the inner stream is faster than the outer stream. For the case of mixing layers with different densities, three-dimensionality is greatly enhanced by Rayleigh-Taylor instability if the inner stream is heavier than the outer stream, and especially if the inner stream is also faster. In the former case the growth rate of the mixing layer was found to be insensitive to changes in the velocity ratio.

The effects of curvature on the structure of the curved turbulent mixing layer were explored in terms of length scales and celerity for the large spanwise structures where these structures could be observed. Other things being equal, the celerity of the large structures was found to depend on density ratio and velocity ratio but not on the sense of the mean streamline curvature.

TABLE OF CONTENTS

LIST OF SYMBOLS

Symbol	Description
A	a constant
a	a constant
B	a constant
b	a constant; also, the half-height of the channel
c	celerity
d	gap between two concentric cylinders, $(R_o - R_i)$
e	spacing between streamwise structures
F	neutral stability boundary
f	focal distance
fn	a function
G	equivalent reduced gravity, defined as $\left(\frac{\rho_i - \rho_o}{\rho_i + \rho_o}\right) \frac{U^2}{R}$
g	gravitational acceleration
g'	reduced gravitational acceleration, defined as $g(\rho_2 - \rho_1)/(\rho_2 + \rho_1)$
$\mathbf{i}$	unit vector in x- direction
J_o	gradient Richardson number, same as Ri
K	a constant
k	wave number
L	characteristic length scale
m	mass
Pr	Prandtl number
p	pressure
p_o	stagnation pressure
q	temporal growth rate

R	mean radius of curvature
Ri	gradient Richardson number, defined as $-g\,\frac{d\rho}{dy}/\rho\left[\frac{du}{dy}\right]^2$
r	radial coordinate
S	spacing between spanwise structures
s	a scalar
Ta	Taylor number, defines as $Rd^3(\Omega_i^2-\Omega_o^2)/\nu^2$
t	time
U	nozzle exit velocity; also, characteristic velocity
$U(y)$	velocity profile
u	velocity component
$\mathbf{u}$	velocity vector
V	characteristic velocity
v	velocity component
$\mathbf{v}$	a vector
v^*	cross-stream velocity
W	characteristic velocity; also, a physical quantity
w	velocity component
$\mathbf{X}$	position vector of the origin of the moving coordinates
x	streamwise (tangential) coordinate
x_v	x-coordinate of the virtual origin
y	normal (radial) coordinate
y_v	y-coordinate of the virtual origin
Z	quantity defined by Eq. (7.2.8)
z	spanwise (axial) coordinate
α_i	temporal growth rate
β	a constant
Γ	the product ur

δ	thickness of the mixing layer
δ_{visual}	visual thickness of the mixing layer
ε	a small quantity
ζ	vorticity component in z - direction
η	vorticity component in x - or θ - direction; also, displacement of fluid interface
θ	angular coordinate
Λ	characteristic length scale
λ	wave length
μ	fluid viscosity
ν	kinematic viscosity
ξ	vorticity component in y - or r - direction
ρ	fluid density
φ	velocity potential
Ψ	stream function
ψ	stream function
$\mathbf{\Omega}$	angular velocity vector of the moving coordinates
Ω	angular velocity
$\boldsymbol{\omega}$	vorticity vector
ω	frequency; also, angular velocity

$\overline{(\,)}$	time-averaged quantites
$(\,)'$	perturbation quantities
$(\,)_o$	quantities pertinent to the outer stream
$(\,)_i$	quantities pertinent to the inner stream
$(\,)_{max}$	the maximum of a quantity
$(\,)_{min}$	the minimum of a quantity

I. Introduction

It is well known that the turbulent shearing stress in a curved shear layer depends strongly on the sense of the curvature. If the high-speed stream is on the inside, much higher turbulent shearing stresses occur. This effect has been attributed to centrifugal instability; for example, in the experimental work by Margolis and Lumley (1965) and by Wyngaard (1967). The associated differences in flow structure, however, have not been fully explored.

Density differences can be expected to modify the effects of centrifugal forces. No experimental reports have been found in the literature which deal with combined effects of velocity difference, density difference, and curvature. The general case is therefore an interesting problem from both the academic and the practical point of view. The purpose of this experiment is to study the combined effects of mean streamline curvature and density difference on the structure of turbulent mixing layers. Flow-visualization studies for such flows can be very instructive, and are a major component of the present research.

There are three different mechanisms of instability in a general curved mixing layer. The Kelvin-Helmholtz instability, associated with the free shear layer *per se*, produces spanwise vortical structures. The Taylor-Görtler instability, associated with centripetal and Coriolis accelerations in a curved flow, produces streamwise vortical structures. The Rayleigh-Taylor instability, associated with the effect of a body force opposed to the density gradient, produces three-dimensional mushroom-like structures. The effect of interaction among these instability mechanisms on the structure of a curved turbulent mixing layer with variable density will be discussed in this chapter.

A general curved mixing layer is shown schematically in the accompanying drawing. Two uniform parallel streams, initially separated by a splitter plate for $x < 0$, are guided into a curved channel of half height b and mean radius of curvature R. The velocities of the two streams are uniform at the inlet and are denoted by U_o and U_i, respectively, for the outer and inner flows. The uniform densities of the two streams are ρ_o and ρ_i, respectively.

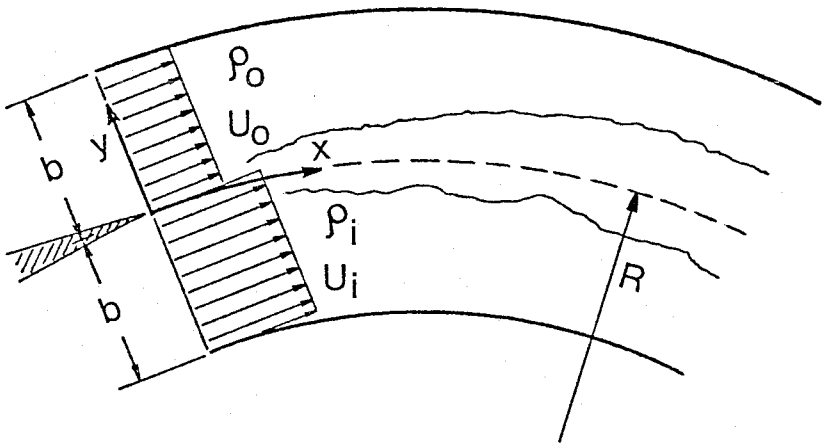

The flow of interest is the mixing zone not too far downstream, where δ, the thickness of the mixing layer, is small compared with the channel height. It is inherent in any definition of a mixing layer that flow quantities like u or ρ are much more uniformly distributed in the free streams than in the mixing zone. As a result, an inflection point must exist in the profile of a particular flow quantity unless this quantity is constant across the mixing layer (neglecting the wake due to the splitter plate).

Under these conditions, three global parameters should suffice to define a curved mixing layer. These may be taken as the density ratio and the velocity ratio of the two incoming uniform streams, and the ratio of layer thickness to mean radius of curvature. Any dependence of the flow on Reynolds number is neglected, on the ground that the flows of interest are fully turbulent. Any suitably normalized time-averaged flow quantity W can thus be expressed as a function of three dimensionless spatial variables and the three global parameters. The parameter space itself may contain one or more surfaces separating different flow regimes, in each of which a distinct flow structure predominates. These surfaces can be represented schematically by, say,

$$F\left(\frac{U_o}{U_i}, \frac{\rho_o}{\rho_i}, \frac{\delta}{R}\right) = 0 \qquad (1.0.1)$$

and are associated with boundaries of neutral stability for various flow structures. It is useful by way of introduction to collect the available analytical evidence on this question for the case of laminar flow.

1.1. Taylor-Görtler Instability

When there is no inflection point in the velocity profile, a constant-density flow is not subject to Kelvin-Helmholtz instability, according to Rayleigh's inflection-point theorem discussed in Section 1.2 below. By studying such flows we may then be able to understand better the phenomena introduced by centripetal and Coriolis accelerations. One flow providing such an opportunity is circular Couette flow, which involves the motion of a viscous fluid of uniform density between two concentric cylinders rotating at constant angular velocity.

In a classic paper, Taylor (1923) formulated the viscous instability problem for circular Couette flow and solved the eigenvalue problem analytically for the case in which the gap d between the two concentric cylinders is small compared to the mean radius. The stability of the flow was found to depend on the dimensionless quantity $Ta = Rd^3(\Omega_i^2 - \Omega_o^2)/\nu^2$, now known as the Taylor number. For the case when the two cylinders rotate in the same direction (the case of interest here), Taylor found the flow to be stable to axisymmetric disturbances when the Taylor number is smaller than a critical value of 1708 (the numerical value cited was obtained by Pellew and Southwell [1940] by a refined calculation). This value is the same as the critical Rayleigh number found for Benard convection. Jeffreys (1928) showed that when the ratio of angular velocity of the two cylinders approaches unity there is an exact analogy between circular Couette flow and the convection instability between two rigid surfaces. Generally, however, the circular Couette flow with both cylinders rotating in the same direction is analogous to the convection flow with streaming. In the latter case, it was proved mathematically by Jeffreys that the convection cells are formed parallel to the streaming direction.

Taylor's 1923 paper also established the stability boundary experimentally. Coles (1965) later showed that several different flow regimes can exist in this simple geometry, depending on the relative rotation of the two cylinders. Roughly speaking, when the inner cylinder is rotating faster than the outer cylinder, instability appears first in the form of axisymmetric Taylor-Görtler vortices. When the difference in rotation speed increases into the non-linear range, the axisymmetric structure turns into a non-axisymmetric wavy mode of motion. When the outer cylinder is rotating faster, the flow is stable in most of the laminar regime. Turbulence emerges in the form of a spiral structure travelling around the cylinders.

Among the wealth of flow structures produced as a result of centrifugal instability, only the axisymmetric Taylor vortices have been thoroughly explored. The physical mechanisms involved in the formation of axisymmetric Taylor vortices have been delineated by Coles (1967). Using a nontrivial algebraic formulation, Coles showed that the essential elements of the flow in the Taylor vortices are (a) the coupling of primary and secondary flows through the action of Coriolis force, and (b) the production of streamwise vorticity through the mechanism of vortex tilting.

1.2. Kelvin-Helmholtz Instability

Simplified forms of the two-dimensional plane stability problem have long been studied, beginning with work by Helmholtz (1868) and Kelvin (1871). Suppose that two horizontal parallel infinite streams of different velocities and densities are in contact with each other, as shown in the sketch. The flow is inviscid and incompressible.

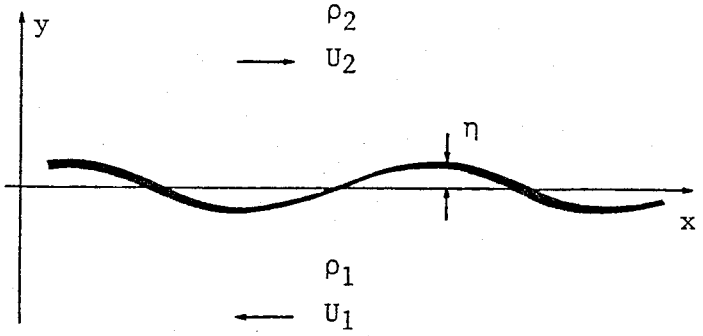

Kelvin assumed that the disturbed flow is two dimensional and irrotational on each side of the interface and studied the growth in time of small disturbances in terms of the velocity potential of the flow. Disturbances of the form $\varphi(z)e^{ikx + qt}$ are sought which satisfy the Laplace equation and the boundary

conditions that the pressure and the vertical velocity are continuous across the disturbed interface. The resulting eigenvalue problem has the solution

$$q = -ik\,\frac{\rho_1 U_1 + \rho_2 U_2}{\rho_1 + \rho_2} \pm k\,\frac{\sqrt{\rho_1\rho_2}}{\rho_1+\rho_2}\,(U_1 - U_2) \qquad (1.2.1)$$

Hence the flow is always unstable, for all wave numbers k, as long as $U_1 \neq U_2$.

The physical mechanism underlying Kelvin-Helmholtz instability has been explained by Landau and Lifshitz (1959) in terms of the pressure field associated with the disturbance. When a small periodic displacement is given to the originally plane interface between the two streams, the pressure disturbance is 180 degrees out of phase with the displacement, and hence the disturbance is amplified. Batchelor (1967) described Kelvin-Helmholtz instability in terms of vorticity dynamics. Since the slip stream in the undisturbed flow is equivalent to a plane vortex sheet, amplification of any displacement of the interface away from its original position results from the self-induced velocity of the vortex sheet and the redistribution of vorticity as a result of convection.

Rayleigh (1880) discussed the inviscid stability of a homogeneous shear layer having a smoothly varying velocity profile instead of a step discontinuity. If the disturbance is small, Euler's equation can be linearized to give

$$\rho\left(\frac{\partial}{\partial t} + U\frac{\partial}{\partial x}\right)\mathbf{u}' + v'\frac{dU}{dy}\mathbf{i} = -\nabla p' \qquad (1.2.2)$$

where $U(y)$ is the basic velocity profile, $\mathbf{i}$ is the unit vector in the x-direction, and $\mathbf{u}'$ and p' are the disturbance velocity and pressure, respectively, for two-dimensional disturbances. The disturbance velocity can be represented by a stream function;

$$u' = \frac{\partial \psi'}{\partial y} \quad , \quad v' = -\frac{\partial \psi'}{\partial x} \tag{1.2.3}$$

Normal mode analysis assumes this stream function to have the form

$$\psi' = \Psi(y) e^{i\alpha(x-ct)} \tag{1.2.4}$$

The linearized Euler equation can then be reduced to an ordinary differential equation. Elimination of the pressure leads to the stability equation of Rayleigh,

$$(U-c)(\Psi'' - \alpha^2 \Psi) - U'' \Psi = 0 \, . \tag{1.2.5}$$

Rayleigh (1880) proved that a necessary condition for instability is that the basic velocity profile $U(y)$ should have an inflection point. Fjørtoft (1950) showed that it is further necessary for instability that the absolute value of vorticity be a maximum at the inflection point. An argument by Tollmien (1935) suggests that neither of these conditions is sufficient for the flow to be unstable.

Michalke (1964, 1965) studied the instability of the hyperbolic-tangent velocity profile for a homogeneous fluid and calculated the growth rate of small disturbances as a function of wave number, using Rayleigh's inviscid stability equation (1.2.5). His result, reproduced in Fig. 1.1, indicates that a wave number exists for which the spatial growth rate is a maximum.

Maslowe and Kelly (1971) studied the inviscid stability of a heterogeneous free shear layer in terms of the Taylor-Goldstein equation, a counterpart of Rayleigh's equation for flow with variable density in an arbitrary gravitational field. For the case of negligible gravity force, they calculated the spatial growth rate for small disturbances as a function of both wave number and density

ratio, as shown in Fig. 1.2. The figure shows that, for a certain range of density ratios, the growth rate is smaller than for a homogeneous shear layer. Davey (1971) and Davey and Roshko (1972) studied the heterogeneous shear layer experimentally and found the theoretical calculations by Michalke and by Maslowe and Kelly to be consistent with their measurements.

The problem of the stability of a free shear layer in a viscous fluid is a generalization of the Kelvin-Helmholtz problem. The linearized mathematical problem leads to the Orr-Sommerfeld equation. For a homogeneous fluid, Curle (1956) considered a hyperbolic-tangent velocity profile and obtained a minimum critical Reynolds number of 8.9. Betchov and Szewczyk (1963) also considered the hyperbolic-tangent profile, but did not find a minimum critical Reynolds number. Physical reasoning led them to predict a minimum critical Reynolds number of 150 for a temporally growing shear layer.

Lessen and Ko (1966) solved the Orr-Sommerfeld equation numerically for a Blasius velocity profile, using the parallel-flow assumption. They found a minimum critical Reynolds number of 3.6. When non-parallelism was taken into account, the minimum critical Reynolds number increased to 12. The stability curves obtained by Lessen and Ko are reproduced in Fig. 1.3 and Fig. 1.4 for the cases of small disturbances to parallel and non-parallel flow, respectively. The curve with $\alpha_i = 0$ represents the curve of neutral stability. Ko and Lessen (1969) revised their earlier calculations and found no minimum critical Reynolds number under the same assumption of parallel flow, and a minimum critical Reynolds number of 10.2 when non-parallelism was considered.

The stability of a heterogeneous shear layer in a viscous fluid has been studied by Baker, Rozenman and Weinstein (1968), who solved the Orr-Sommerfeld equation using Lessen's method (Lessen 1949). Their results do not include a complete neutral stability curve. Maslowe and Thompson (1971) employed

Holmboe's model for the density profile and a hyperbolic-tangent velocity profile and solved the Orr-Sommerfeld equation numerically. The density difference was derived from the temperature difference governed by the energy equation. The neutral stability curve determined by Maslowe and Thompson for the viscous shear layer with density difference, for the case where there is no gravity term, is shown as the curve labelled $J_0 = 0$ in Fig. 1.5. According to this curve, there is no minimum critical Reynolds number. The other curves in the same figure, corresponding to other values of J_0 (the gradient Richardson number $Ri = -\frac{g}{\rho}\frac{d\rho}{dy}\Big/\left[\frac{du}{dy}^2\right]$), are for flows influenced by gravity.

1.3. Rayleigh-Taylor Instability

In a curvilinear motion,the centripetal acceleration imposes an inertial body force acting like gravity on the fluid. The system is then statically stable or unstable according to whether the heavier fluid is on the bottom (the outside) or on the top (the inside). Historically, this problem was first studied by Rayleigh (1883). Taylor (1950) pointed out the equivalence of centripetal acceleration and gravity. For the gravitational case, the mathematical nature of this problem, known generally as Rayleigh-Taylor instability, can be stated as follows, according to Lamb (1932).

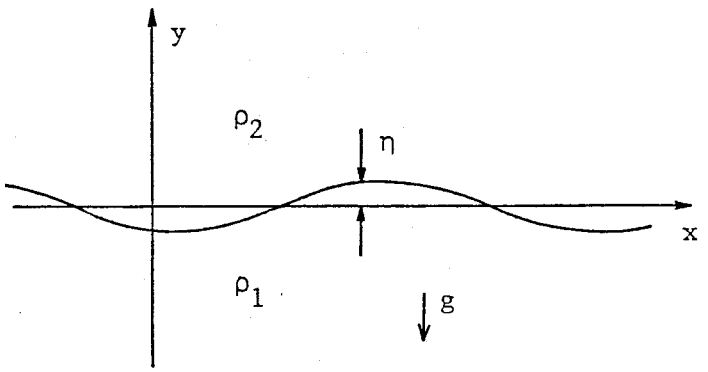

Consider an initially flat interface subjected to a small disturbance, as shown in the accompanying sketch, so that the disturbed surface can be written as

$$\eta = \varepsilon \cos kx \; e^{i\omega t} \tag{1.3.1}$$

Since the fluids are initially at rest, the disturbed flow will be irrotational if viscosity is neglected. For the case when both streams are unbounded, the velocity potential satisfying the condition of unmixed fluids at the interface can be written

$$\varphi_1 = -i\varepsilon \frac{\omega}{k}(\cos kx)e^{ky} \; e^{i\omega t}, \quad y < 0 \tag{1.3.2}$$

and

$$\varphi_2 = i\varepsilon \frac{\omega}{k}(\cos kx)e^{-ky} \; e^{i\omega t}, \quad y > 0. \tag{1.3.3}$$

Across the interface, there can be no difference in pressure. Bernoulli's equation reads

$$\frac{p_1}{\rho_1} = \frac{\partial \varphi_1}{\partial t} - gy, \quad y < 0 \tag{1.3.4}$$

$$\frac{p_2}{\rho_2} = \frac{\partial \varphi_2}{\partial t} - gy, \quad y > 0 \tag{1.3.5}$$

Hence we have $\rho_1(\frac{\omega^2}{k} - g) = \rho_2(-\frac{\omega^2}{k} - g)$ and $\omega^2 = gk\left[\frac{\rho_1 - \rho_2}{\rho_1 + \rho_2}\right]$. When the

lower fluid is heavier; i.e., when $\rho_1 > \rho_2$, ω is real, and the disturbance propagates like a wave. However, when the upper fluid is heavier, ω is imaginary, and the disturbance grows exponentially. Lamb also discussed the case when the fluids are bounded both from the top and from the bottom by horizontal surfaces, and found an expression for ω^2 as a function of kb, where b in the present notation is half the distance between the two bounding surface. Although the formulation given above assumes waves propagating in the x direction, the same result applies to waves propagating in any other direction perpendicular to y.

Experimental studies of Rayleigh-Taylor instability has been performed by Lewis (1950), Emmons, Chang, and Watson (1960), Cole and Tankin (1973) and Ratafia (1973). Bellman and Pennington (1954) investigated the effects of viscosity. Using a model equation in which viscosity is incorporated as a damping term for a second-order system, Plesset and Whipple (1974) found that viscosity is important in determining the wavelength of the fastest growing disturbances, for which $\lambda \propto 4\pi(\nu^2/g')^{1/3}$ where g' is reduced gravity and is defined as $\left(\frac{\rho_2 - \rho_1}{\rho_2 + \rho_1}\right) g$.

A summary by Sharp (1983) shows that the structure produced by Rayleigh-Taylor instability is three-dimensional and can be strongly influenced by the density and viscosity profiles. Typical shapes of the structure at early times are like mushrooms, fingers, or spikes. These shapes soon interact with each other and break up by various mechanisms which are not yet understood. Eventually, however, if the two fluids are immiscible, the heavy fluid will fall completely underneath the light fluid and stay there, as long as the ocean is underneath the sky.

The irreversible process discussed in the last paragraph can be preempted if the density of the falling and rising fluids can be changed by external intervention. For example, if a horizontal layer of fluid bounded by two horizontal rigid surfaces is uniformly heated from below and cooled from above, so that a density gradient is maintained in a direction opposite to the gravitational force, a colder and hence heavier fluid element which has fallen as a result of gravity will be warmed when it comes close to the bottom surface, where it may change roles and become the lighter fluid. This kind of thermal instability problem, originally defined by Bénard (1900), was first investigated mathematically by Rayleigh (1916). The critical Rayleigh number for instability, for the case where both surfaces are rigid, was first calculated by Jeffreys (1928). The value determined by Reid and Harris (1958) is 1707.762. Experiments done with two rigid boundaries, for example by Oertel and Kirchartz (1979) and Oertel (1982), show roll cells with orientation depending on the shape of the container. Since in our experiments, in which the mixing layers are bounded by fluids of different species, the density of a fluid element is not changed except by molecular diffusion (which is rather small), we do not expect the same kind of structure to appear. Hence we will limit our discussion on Benard cells. Detailed discussions of this thermal instability problem can be found in Chandrasekhar (1961) and Drazin and Reid (1981).

1.4. Turbulent Flow

The plane turbulent mixing layer has attracted the attention of many researchers for many years. An important feature in this flow is the organized structure first discovered by Brown and Roshko (1971, 1974). As shown by Brown and Roshko, the plane mixing layer contains large spanwise vortical structures which travel downstream with a definite speed, or celerity. These vortices grow by entrainment of fresh fluid and also by more complex processes such as pairing and tearing. The effects of velocity ratio and density ratio on

the growth of the plane mixing layer have both been studied experimentally. For example, an expression for the growth rate, $\delta_{visual} = const\left(\frac{U_o - U_i}{U_o + U_i}\right)$, was proposed by Sabin (1965). This expression was endorsed by Brown and Roshko (1974), who also found the effect of density difference on the growth of the mixing layer to be small. Brown (1974) and Dimotakis (1984) expressed the growth rate as a function of both velocity ratio and density ratio. The formation of vortices in a laminar free mixing layer has been explained by Michalke (1965a), using stability theory. In *turbulent* mixing layers the large-scale two-dimensional vortices discovered by Brown and Roshko (1974) can presumably still be attributed to the general Kelvin-Helmholtz instability. Even though the laminar stability theory does not apply in turbulent flow, the basic driving mechanism associated with the layer of concentrated vorticity is the same.

The contributions mentioned above all refer to the two-dimensional instability of the plane mixing layer. The experiments of Brown and Roshko indicate, however, that the main structure of the turbulent mixing layer is three-dimensional, although organized structures also exist in the streamwise direction. The interaction of the streamwise structures with the spanwise vortices was shown by Breidenthal (1978) and Bernal (1981) to be important for transition. The three-dimensional instability of the structure of a shear layer has long been considered a topic of vortex dynamics; see, for example, the work of Moore and Saffman (1975), Saffman (1980), Pierrehumbert and Widnall (1982), and Robinson and Saffman (1982).

For free shear layers in a curved channel, with uniform density, most of the existing information is based on hot-wire measurements. Margolis and Lumley (1965) and Margolis (1965) investigated the curved shear layer formed at the exit of an open-circuit wind tunnel. The high-speed stream was supplied by the

tunnel, and the low-speed stream came from entrainment into the high-speed stream. The two streams had different thicknesses, with the low-speed stream thicker by a factor of 4. The radius of curvature of the outer wall of the curved channel was four times the total channel height. Margolis and Lumley reported much stronger Reynolds shearing stresses and turbulence production for the case when the high-speed stream was on the inside. Wyngaard (1967) and Wyngaard, Tennekes, Lumley, and Margolis (1968) repeated the measurements and calculations, using the same basic wind tunnel but improving the small-scale resolving power of their hot-wire instrumentation; they concluded that the turbulence production in the unstable case, with the high-speed stream inside, is actually close to that in the stable case, with the high-speed stream outside. However, the large difference in turbulent shearing stress remains. The Reynolds shearing stress measured by Wyngaard is shown in Fig. 1.6, with the stable and unstable cases together for comparison. It is clear that not only is the maximum shearing stress larger in the unstable case, but also the region of appreciable shearing stress is thicker. This effect has been attributed to centrifugal instability. Hunt and Joubert (1979) proposed a Reynolds-stress re-orientation theory for this phenomenon and found that qualitative agreement was achieved between theory and experimental data obtained in a curved duct flow. Few of the studies mentioned above paid particular attention to the possible effects of bounding curved walls on the turbulent shear layer. Wood and Bradshaw (1982) suggested that the presence of a wall can have large effects on the flow structure. Gibson and Younis (1983), however, concluded otherwise. None of these studies provided any evidence for the structure of the flow by means of flow visualization, which is a main component of the present study.

1.5. The Present Problem

The main purpose of this study is to look for effects of streamline curvature on the structure of the turbulent mixing layer. Discussions in the previous paragraphs have considered the stability and structure of various limiting cases. When both density and velocity are variable in a curved mixing layer, we encounter the general case.

The Taylor-Görtler instability, which is responsible for the formation of streamwise vortices in curved shear flows, can be extended to cover flows with variable density. It is relatively easy to extend Taylor's argument, or Rayleigh's criterion, to inhomogeneous flow. Consider the incompressible motion of an inviscid fluid in a circular path.

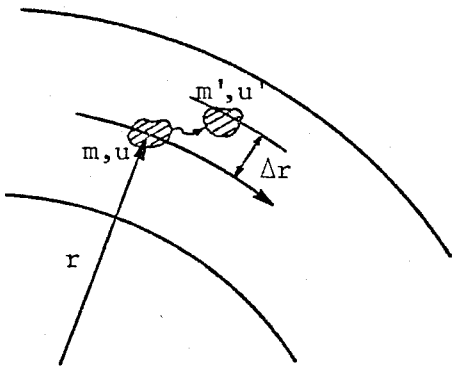

The centrifugal force experienced by a fluid element situated at a radial location r is equal to $mu^2/r = (mur)^2/mr^3$, where mur is the angular momentum and m is the mass of the fluid element. When the flow is in equilibrium, this centrifugal force is balanced by the local pressure force exerted on the fluid element by its surroundings. Suppose that the fluid element is displaced to a new radial

location r', where the local pressure field supplies a net balancing force $(m'u'r')^2/m'r'^3$, as shown in the accompanying sketch. The new centrifugal force experienced by the fluid element becomes $(mur)^2/mr'^3$, because the angular momentum and the mass of the fluid element are both conserved during the displacement.

The fluid element will tend to return to its original location r if the restoring force is greater than the centrifugal force; i.e., if $m'u'^2r'^2 > mu^2r^2$. For two-dimensional curved shear layers involving a density difference, the conclusion is that the basic flow will be stable if $\frac{d}{dr}(\rho u^2r^2) > 0$. This condition has been proved more rigorously by Synge (1933) to be necessary and sufficient for the stability of axisymmetric disturbances, and is called the Rayleigh-Synge criterion.

The success achieved by Taylor (1923) in applying Rayleigh's criterion to account for the appearance of streamwise vortices in circular Couette flow suggests that strong streamwise vortical structures might be produced in a curved mixing layer by making the inner stream heavier or faster, as indicated by the Rayleigh-Synge criterion. That is, the effect of velocity can be supplemented by the effect of density. Accordingly, streamwise vortices might be expected to dominate a curved flow whose inner stream is heavier. However, such a flow may also be subject to Rayleigh-Taylor instability, as argued earlier, with generation of three-dimensional structures.

As far as two-dimensional spanwise disturbances are concerned, the existence of an inflection point in the velocity profile of a general mixing layer suggests the continued relevance of Kelvin-Helmholtz instability. Extensions of Kelvin-Helmholtz instability to gravitational flows involving discontinuous velocity profiles and density differences have been discussed by Chandrasekhar (1961)

and Drazin and Reid (1981), who showed that in the limit of equal velocities Kelvin-Helmholtz instability reduces to Rayleigh-Taylor instability.

The three inter-related instability mechanisms can be distinguished upon inspection of the vorticity equation,

$$\rho \frac{D\boldsymbol{\omega}}{Dt} = \rho(\boldsymbol{\omega}\cdot\nabla)\mathbf{u} + \frac{1}{\rho}(\nabla\rho\times\nabla p) + \mu\nabla^2\boldsymbol{\omega} + \frac{\mu}{\rho}\nabla\rho\times(\nabla^2\mathbf{u}) \qquad (1.5.1)$$

which is valid for an incompressible flow (i.e., $div\,\mathbf{u} = 0$) with constant viscosity μ.

As explained by Batchelor (1967), the Kelvin-Helmholtz instability is associated with convection of vorticity, represented by the first term on the left-hand side of the vorticity equation. The Taylor-Görtler instability, associated with the tilting of vorticity according to Coles (1967), is connected with the first term on the right-hand side. The Rayleigh-Taylor instability, associated with the production of vorticity when the density gradient is not parallel to the pressure gradient (Scorer 1978), is connected with the second term on the right-hand side of the vorticity equation.

Unfortunately, the vorticity equation is coupled to the equation of momentum and the equation of continuity. It is therefore difficult to draw solid conclusions regarding the relative importance of the individual driving mechanisms; i.e., density gradient, velocity gradient, and streamline curvature, without taking into consideration the whole set of governing equations simultaneously. This problem will be attacked in the next section.

II. Algebraic Stability Arguments

2.1. Algebraic Formulation of the Stability Problem

In this section we will attempt to characterize the three instabilities described above, and their combinations, without reducing the differential equations of motion to a formal eigenvalue problem of the conventional kind. The analysis will move in the conventional direction at first, in the sense that we will assume laminar flow and will consider the linearized problem of small perturbations to a particular basic flow. However, the machinery which is eventually used to extract practical results will be algebraic rather than analytic. This machinery will be developed as soon as the mathematical problem has been properly formulated.

The fundamental physical laws governing the flow structure are conservation of mass and conservation of momentum. Density changes will be associated with the presence of different fluids, rather than with effects of heat transfer or compressibility. Thus no energy equation is required. In fact, useful results can apparently be obtained without using equations for diffusion of species. In such a case there are two equations of continuity,

$$\nabla \cdot \mathbf{u} = 0 \tag{2.1.1}$$

and

$$\frac{D\rho}{Dt} = 0 \qquad (2.1.2)$$

For simplicity, because the eventual application is to turbulent flow, the viscosity (but not the density) will be taken as constant; i.e., independent of position. The momentum equation is then

$$\rho \frac{D\mathbf{u}}{Dt} = \rho \left[\frac{\partial \mathbf{u}}{\partial t} + (\mathbf{u} \cdot \nabla)\mathbf{u} \right] = -\nabla p + \mu \nabla^2 \mathbf{u} \qquad (2.1.3)$$

where $\nabla^2 \mathbf{u} = \text{div}(\text{grad } \mathbf{u})$. The transport equation for vorticity $\underline{\omega} = \nabla \times \mathbf{u}$ is obtained by taking the curl of the momentum equation (2.1.3) after dividing by ρ. A useful vector identity is

$$\nabla \times (s\mathbf{v}) = s(\nabla \times \mathbf{v}) + \nabla s \times \mathbf{v} \qquad (2.1.4)$$

where s is a scalar and $\mathbf{v}$ is a vector. The result for vorticity is

$$\rho \frac{D\boldsymbol{\omega}}{Dt} = \rho \left[\frac{\partial \boldsymbol{\omega}}{\partial t} + (\mathbf{u} \cdot \nabla)\,\boldsymbol{\omega} \right]$$

$$= \rho\,(\boldsymbol{\omega} \cdot \nabla)\,\mathbf{u} + \frac{1}{\rho} \nabla \rho \times \nabla p + \mu \nabla^2 \boldsymbol{\omega} + \frac{\mu}{\rho} \nabla \rho \times \nabla^2 \mathbf{u} \qquad (2.1.5)$$

The terms on the right-hand side represent vorticity changes caused by vortex stretching/tilting, by baroclinic (pressure) torque, by viscous diffusion, and by exoclinic (viscous) torque.

We want to examine these equations in cylindrical polar coordinates (r, θ, z). The velocity components will be denoted by (u, v, w) and the vorticity components by (ξ, η, ξ). The equations of continuity become

$$\frac{\partial u}{\partial r} + \frac{u}{r} + \frac{1}{r}\frac{\partial v}{\partial \theta} + \frac{\partial w}{\partial z} = 0. \tag{2.1.6}$$

$$\frac{\partial \rho}{\partial t} + u\,\frac{\partial \rho}{\partial r} + \frac{v}{r}\frac{\partial \rho}{\partial \theta} + w\,\frac{\partial \rho}{\partial z} = 0 \tag{2.1.7}$$

The three components of the momentum equation become

$$\rho\left(\frac{\partial u}{\partial t} + u\frac{\partial u}{\partial r} + \frac{v}{r}\frac{\partial u}{\partial \theta} + w\,\frac{\partial u}{\partial z} - \frac{v^2}{r}\right) = -\frac{\partial p}{\partial r} + \mu\left(\nabla^2 u - \frac{u}{r^2} - \frac{2}{r^2}\frac{\partial v}{\partial \theta}\right) \tag{2.1.8}$$

$$\rho\left(\frac{\partial v}{\partial t} + u\frac{\partial v}{\partial r} + \frac{v}{r}\frac{\partial v}{\partial \theta} + w\frac{\partial v}{\partial z} + \frac{uv}{r}\right) = -\frac{1}{r}\frac{\partial p}{\partial \theta} + \mu\left(\nabla^2 v - \frac{v}{r^2} + \frac{2}{r^2}\frac{\partial u}{\partial \theta}\right) \tag{2.1.9}$$

$$\rho\left(\frac{\partial w}{\partial t} + u\frac{\partial w}{\partial r} + \frac{v}{r}\frac{\partial w}{\partial \theta} + w\frac{\partial w}{\partial z}\right) = -\frac{\partial p}{\partial z} + \mu\nabla^2 w \tag{2.1.10}$$

where

$$\nabla^2 s = \frac{\partial^2 s}{\partial r^2} + \frac{1}{r}\frac{\partial s}{\partial r} + \frac{1}{r^2}\frac{\partial^2 s}{\partial \theta^2} + \frac{\partial^2 s}{\partial z^2} \tag{2.1.11}$$

The vorticity equations, although formally redundant, will be used in what follows to avoid dealing directly with the pressure. The three components of vorticity are

$$\xi = \frac{1}{r}\frac{\partial w}{\partial \theta} - \frac{\partial v}{\partial z} \tag{2.1.12}$$

$$\eta = \frac{\partial u}{\partial z} - \frac{\partial w}{\partial r} \tag{2.1.13}$$

$$\zeta = \frac{1}{r}\frac{\partial}{\partial r}(rv) - \frac{1}{r}\frac{\partial u}{\partial \theta} \tag{2.1.14}$$

and the three components of the vorticity equation are

$$\rho\left(\frac{\partial \xi}{\partial t} + u\,\frac{\partial \xi}{\partial r} + \frac{v}{r}\frac{\partial \xi}{\partial \theta} + w\,\frac{\partial \xi}{\partial z} - \frac{v\eta}{r}\right)$$

$$= \rho\left(\xi\frac{\partial u}{\partial r} + \frac{\eta}{r}\frac{\partial u}{\partial \theta} + \zeta\,\frac{\partial u}{\partial z} - \frac{\eta v}{r}\right) + \frac{1}{\rho}\left(\frac{1}{r}\frac{\partial \rho}{\partial \theta}\frac{\partial p}{\partial z} - \frac{1}{r}\frac{\partial \rho}{\partial z}\frac{\partial p}{\partial \theta}\right) + \mu\left(\nabla^2\xi - \frac{\xi}{r^2} - \frac{2}{r^2}\frac{\partial \eta}{\partial \theta}\right)$$

$$+ \frac{\mu}{\rho}\left[\frac{1}{r}\frac{\partial \rho}{\partial \theta}\nabla^2 w - \frac{\partial \rho}{\partial z}\left(\nabla^2 v - \frac{v}{r^2} + \frac{2}{r^2}\frac{\partial u}{\partial \theta}\right)\right] \tag{2.1.15}$$

$$\rho\left(\frac{\partial \eta}{\partial t}+u\frac{\partial \eta}{\partial r}+\frac{v}{r}\frac{\partial \eta}{\partial \theta}+w\frac{\partial \eta}{\partial z}+\frac{v\xi}{r}\right)$$

$$=\rho\left(\xi\frac{\partial v}{\partial r}+\frac{\eta}{r}\frac{\partial v}{\partial \theta}+\zeta\frac{\partial v}{\partial z}+\frac{\eta u}{r}\right)+\frac{1}{\rho}\left(\frac{\partial \rho}{\partial z}\frac{\partial p}{\partial r}-\frac{\partial \rho}{\partial r}\frac{\partial p}{\partial z}\right)+\mu\left(\nabla^2\eta-\frac{\eta}{r^2}+\frac{2}{r^2}\frac{\partial \xi}{\partial \theta}\right)$$

$$+\frac{\mu}{\rho}\left[\frac{\partial \rho}{\partial z}\left(\nabla^2 u-\frac{u}{r^2}-\frac{2}{r^2}\frac{\partial v}{\partial \theta}\right)-\frac{\partial \rho}{\partial r}\nabla^2 w\right] \qquad (2.1.16)$$

$$\rho\left(\frac{\partial \zeta}{\partial t}+u\frac{\partial \zeta}{\partial r}+\frac{v}{r}\frac{\partial \zeta}{\partial \theta}+w\frac{\partial \zeta}{\partial z}\right)$$

$$=\rho\left(\xi\frac{\partial w}{\partial r}+\frac{\eta}{r}\frac{\partial w}{\partial \theta}+\zeta\frac{\partial w}{\partial z}\right)+\frac{1}{\rho}\left(\frac{1}{r}\frac{\partial \rho}{\partial r}\frac{\partial p}{\partial \theta}-\frac{1}{r}\frac{\partial \rho}{\partial \theta}\frac{\partial p}{\partial r}\right)+\mu\nabla^2\zeta$$

$$+\frac{\mu}{\rho}\left[\frac{\partial \rho}{\partial r}\left(\nabla^2 v-\frac{v}{r^2}+\frac{2}{r^2}\frac{\partial u}{\partial \theta}\right)-\frac{1}{r}\frac{\partial \rho}{\partial \theta}\left(\nabla^2 u-\frac{u}{r^2}-\frac{2}{r^2}\frac{\partial v}{\partial \theta}\right)\right] \qquad (2.1.17)$$

2.2. The Linearized Problem

An inquiry into the stability of a fluid motion normally involves a basic flow subject to small perturbations. The basic flow which is appropriate for the present problem is a spatially growing mixing layer. The perturbations should also be assumed to grow in space rather than in time. The resulting problem, however, is too difficult to treat by the methods used here. Instead, the mixing

layer will be taken as a static flow which grows neither in space nor time, and only the condition of neutral stability will be sought. This restriction is not necessary. If, for example, $u' = f(r)\exp[i\alpha(x - ct)]$, then $\partial u'/\partial t = \alpha c_i u$, and a suitable generalization of the algebraic method is straightforward.

In practice, there are two important perturbations to be considered. One corresponds to Taylor-Görtler instability and requires a disturbance periodic in the axial direction. The other corresponds to Kelvin-Helmholtz instability and requires a disturbance periodic in the tangential direction. The third or Rayleigh-Taylor instability will appear as a bridge between these two inital analyses.

After this introduction, we choose the basic flow as essentially a circular Couette flow having fluid rather than solid walls. In particular, this basic flow is steady, two-dimensional, and axisymmetric;

$$\bar{u} = 0 \tag{2.2.1}$$

$$\bar{v} = \bar{v}(r) \tag{2.2.2}$$

$$\bar{w} = 0 \tag{2.2.3}$$

where the overbar can be understood as denoting a temporal mean value, in anticipation of the later application to turbulent flow. If the density is not constant, the mean value is also assumed to depend only on radius;

$$\bar{\rho} = \bar{\rho}(r) \tag{2.2.4}$$

The radial and tangential momentum equations reduce to

$$\frac{d\bar{p}}{dr} = \bar{\rho}\frac{\bar{v}^2}{r} \tag{2.2.5}$$

and

$$\mu\left(\frac{d^2\bar{v}}{dr^2} + \frac{1}{r}\frac{d\bar{v}}{dr} - \frac{\bar{v}}{r^2}\right) = 0 \tag{2.2.6}$$

respectively. The mean vorticity has only a tangential component;

$$\bar{\xi} = 0 \tag{2.2.7}$$

$$\bar{\eta} = 0 \tag{2.2.8}$$

$$\bar{\zeta} = \frac{1}{r}\frac{d(r\bar{v})}{dr} \tag{2.2.9}$$

For classical circular Couette flow, which is precisely described by Eqs. (2.2.5)-(2.2.9), the integral of Eq. (2.2.6) is often written

$$\bar{v} = A\,r + \frac{B}{r} \tag{2.2.10}$$

where A and B are constants determined by the no-slip condition at the two cylindrical walls. The vorticity $\bar{\zeta} = dr\bar{v}/rdr$ is

$$\bar{\zeta} = 2A \tag{2.2.11}$$

and the angular velocity $\bar{\omega} = \bar{v}/r$ is

$$\bar{\omega} = A + \frac{B}{r^2} \tag{2.2.12}$$

The approximation adopted here is that the shear layer is equivalent to a Couette flow except that there is irrotational flow on both sides of the shear layer, with

$$\bar{v} = \frac{B_o}{r}, \frac{B_i}{r} \tag{2.2.13}$$

Now let small disturbances be superposed on the mean flow defined by Eq. (2.2.10), thus

$$u = u' \tag{2.2.14}$$

$$v = \bar{v}(r) + v' \tag{2.2.15}$$

$$w = w' \tag{2.2.16}$$

$$p = \bar{p}(r) + p' \tag{2.2.17}$$

$$\rho = \bar{\rho}(r) + \rho' \tag{2.2.18}$$

$$\xi = \frac{1}{r}\frac{\partial u'}{\partial \theta} - \frac{\partial v'}{\partial z} = \xi' \tag{2.2.19}$$

$$\eta = \frac{\partial u'}{\partial z} - \frac{\partial \omega'}{\partial r} = \eta' \tag{2.2.20}$$

$$\zeta = \bar{\zeta} + \frac{1}{r}\frac{\partial (rv')}{\partial r} - \frac{1}{r}\frac{\partial u'}{\partial \theta} = \bar{\zeta} + \zeta' \tag{2.2.21}$$

Linearize the equations of motion, and subtract the terms representing the mean flow. The result is, for continuity;

$$\frac{1}{r}\frac{\partial (ru')}{\partial r} + \frac{1}{r}\frac{\partial v'}{\partial \theta} + \frac{\partial \omega'}{\partial z} = 0 \tag{2.2.22}$$

$$\frac{\partial \rho'}{\partial t} + u'\frac{d\bar{\rho}}{dr} + u'\frac{\partial \rho'}{\partial r} + \frac{\bar{v}}{r}\frac{\partial \rho'}{\partial \theta} + \frac{v'}{r}\frac{\partial \rho'}{\partial \theta} + w'\frac{\partial \rho'}{\partial z} = 0 \tag{2.2.23}$$

for momentum;

$$\bar{\rho}\left(\frac{\partial u'}{\partial t} + \frac{\bar{v}}{r}\frac{\partial u'}{\partial \theta} - \frac{2}{r}\bar{v}\,v'\right) - \rho'\frac{\bar{v}^2}{r} = -\frac{\partial p'}{\partial r} + \mu\left[\nabla^2 u' - \frac{u'}{r^2} - \frac{2}{r^2}\frac{\partial v'}{\partial \theta}\right] \tag{2.2.24}$$

$$\bar{\rho}\left[\frac{\partial v'}{\partial t}+\frac{u'}{r}\frac{\partial(r\bar{v})}{\partial r}+\frac{\bar{v}}{r}\frac{\partial v'}{\partial\theta}\right]=-\frac{1}{r}\frac{\partial p'}{\partial\theta}+\mu\left[\nabla^2 v'-\frac{v'}{r^2}+\frac{2}{r^2}\frac{\partial u'}{\partial\theta}\right] \qquad (2.2.25)$$

$$\bar{\rho}\left[\frac{\partial\omega'}{\partial t}+\frac{\bar{v}}{r}\frac{\partial\omega'}{\partial\theta}\right]=-\frac{\partial p'}{\partial z}+\mu\nabla^2\omega' \qquad (2.2.26)$$

and for vorticity;

$$\bar{\rho}\left[\frac{\partial\xi'}{\partial t}+\frac{\bar{v}}{r}\frac{\partial\xi'}{\partial\theta}\right]=\bar{\rho}\bar{\zeta}\frac{\partial u'}{\partial z}+\mu\left[\nabla^2\xi'-\frac{\xi'}{r^2}-\frac{2}{r^2}\frac{\partial\eta'}{\partial\theta}\right]-\frac{\mu}{\bar{\rho}}\frac{\partial\rho'}{\partial z}\frac{\partial\bar{\zeta}}{\partial r} \qquad (2.2.27)$$

$$\bar{\rho}\left[\frac{\partial\eta'}{\partial t}+\frac{\bar{v}}{r}\frac{\partial\eta'}{\partial\theta}+\frac{\bar{v}}{r}\xi'\right]=\bar{\rho}\left[\xi'\frac{d\bar{v}}{dr}+\bar{\zeta}\frac{\partial v'}{\partial z}\right]+\frac{1}{\bar{\rho}}\left[\frac{\partial\rho'}{\partial z}\frac{d\bar{p}}{dr}-\frac{\partial p'}{\partial z}\left[\frac{d\bar{\rho}}{dr}+\frac{\partial\rho'}{\partial r}\right]\right]$$

$$+\mu\left[\nabla^2\eta'-\frac{\eta'}{r^2}+\frac{2}{r^2}\frac{\partial\xi'}{\partial\theta}\right]+\frac{\mu}{\bar{\rho}}\left[\frac{d\bar{\rho}}{dr}+\frac{\partial\rho'}{\partial r}\right]\nabla^2\omega' \qquad (2.2.28)$$

$$\bar{\rho}\left[\frac{\partial\zeta'}{\partial t}+u'\frac{d\bar{\zeta}}{dr}+\frac{\bar{v}}{r}\frac{\partial\zeta'}{\partial\theta}\right]=\bar{\rho}\,\bar{\zeta}\frac{\partial\omega'}{\partial z}+\frac{1}{\bar{\rho}}\left[\frac{1}{r}\frac{\partial p'}{\partial\theta}\left[\frac{d\bar{\rho}}{dr}+\frac{\partial\rho'}{\partial r}\right]-\frac{1}{r}\frac{\partial\rho'}{\partial\theta}\frac{d\bar{p}}{dr}\right]+\mu\nabla^2\zeta'$$

$$-\frac{\mu}{\bar{\rho}}\left[\frac{d\bar{\rho}}{dr}+\frac{\partial\rho'}{\partial r}\right]\left[\nabla^2 v'-\frac{v'}{r^2}+\frac{2}{r^2}\frac{\partial u'}{\partial\theta}\right]+\frac{\mu}{\bar{\rho}}\frac{\partial\rho'}{\partial r}\frac{d\bar{\zeta}}{dr}+\mu\frac{\rho'}{\bar{\rho}}\frac{1}{r}\frac{d}{dr}\left[r\frac{d\bar{\zeta}}{dr}\right] \qquad (2.2.29)$$

where

$$\nabla^2 s' = \frac{\partial^2 s'}{\partial r^2} + \frac{1}{r}\frac{\partial s'}{\partial r} + \frac{1}{r^2}\frac{\partial^2 s'}{\partial \theta^2} + \frac{\partial^2 s'}{\partial z^2} \tag{2.2.30}$$

and

$$\xi' = \frac{1}{r}\frac{\partial w'}{\partial \theta} - \frac{\partial v'}{\partial z} \tag{2.2.31}$$

$$\eta' = \frac{\partial u'}{\partial z} - \frac{\partial \omega'}{\partial r} \tag{2.2.32}$$

$$\zeta' = \frac{1}{r}\frac{\partial (rv')}{\partial r} - \frac{1}{r}\frac{\partial u'}{\partial \theta} \tag{2.2.33}$$

The linearization assumes $v' << \bar{v}$ and $p' << \Delta\bar{p}$, because the two variables $\bar{v}$ and $\bar{p}$ are specified by equations of lower order. However, there is no information available about the density, and the linearization therefore does not yet assume $\rho' << \Delta\bar{\rho}$ in Eqs. (2.2.23), (2.2.28), and (2.2.29).

Eqs. (2.2.22)-(2.2.33) will be specialized for individual problems and will be used repeatedly in the rest of our discussions.

2.3. The Algebraic Model

We will now argue that it is possible to gain some useful physical insight into the mechanics of the motion in the shear layer without undertaking a solution of the formidable equations just derived. The argument is an extension of a method developed by Coles (1967) for the case of circular Couette flow. Specifically, the objective is to replace the differential equations by algebraic equations which are in some sense equivalent. This process might be referred

to, somewhat facetiously, as "D/A conversion." For the most part, the equations should be read almost like Fortran statements; i.e., the meaning of the symbol "=" is essentially that the quantity on the left can be replaced by the quantity on the right. The method is considerably more than dimensional analysis, because it succeeds in establishing interactions between various dimensionless parameters by retaining the main physical content of the equations. At the same time, the method is considerably less than a formulation of an eigenvalue problem. The results obtained are useful mainly as formulas for interpolation and extrapolation. Because the method is heuristic, it has to be used with care. In particular, the derivation is not unique. There is some ambiguity in signs, and an occasional empirical constant is needed to obtain a plausible result. A slow beginning and considerable practice with the method are in order, and different aspects of the method will therefore be approached in order of increasing difficulty. Various rules of the game will be established as they are required.

2.4. Taylor-Görtler Instabilty; Constant Density

We first consider the neutral stability of a curved axisymmetric mixing layer subjected to axisymmetric disturbances. Thus $\frac{\partial}{\partial \theta} = 0$ for both the mean flow and the perturbations. The secondary motion is expected to consist of streamwise vortices which are periodic in the axial or z direction. Each vortex is approximately square in cross section. The condition of neutral stability will be imposed by assuming steady flow, $\frac{\partial}{\partial t} = 0$.

To illustrate the method, we begin with the case of constant density. There are six dependent variables; u', v', w', p', ξ', η'. However, the pressure can be bypassed, so that five equations suffice for the argument. They are the continuity equation,

$$\frac{\partial u'}{\partial r} + \frac{u'}{r} + \frac{\partial w'}{\partial z} = 0 \tag{2.4.1}$$

the tangential momentum equation, which does not contain the pressure;

$$\bar{\rho}\,\bar{\zeta} u' = \mu \left(\nabla^2 v' - \frac{v'}{r^2} \right) \tag{2.4.2}$$

the tangential vorticity equation;

$$\bar{\rho}\bar{\omega}\xi' = \bar{\rho} \left(\xi' \frac{d\bar{v}}{dr} + \bar{\zeta} \frac{\partial v'}{\partial z} \right) + \mu \left(\nabla^2 \eta' - \frac{\eta'}{r^2} \right) \tag{2.4.3}$$

and the two definitions

$$\xi' = - \frac{\partial v'}{\partial z} \tag{2.4.4}$$

$$\eta' = \frac{\partial u'}{\partial z} - \frac{\partial w'}{\partial r} \tag{2.4.5}$$

Before any approximations or substitutions are made, it is convenient to revise Eq. (2.4.3) by noting that

$$\bar{\rho}\bar{\omega}\xi' - \bar{\rho} \left(\xi' \frac{d\bar{v}}{dr} + \bar{\zeta} \frac{\partial v'}{\partial z} \right) = - 2\bar{\rho}\bar{\omega} \frac{\partial v'}{\partial z} \tag{2.4.6}$$

Half of the term on the right-hand side of (2.4.6) originates in rotation of the unit vectors, and half originates in the vorticity-tilting term.

Consider the continuity equation (2.4.1). Let u' and w' be replaced by velocity scales U and W, respectively, which are taken to be positive constants and which play somewhat the same role as eigenfunctions. In a similar spirit, let derivatives like $\partial/\partial r$, $\partial^2/\partial r^2$ be replaced by $1/L$ and $1/L^2$, as required, and let derivatives like $\partial/\partial z$, $\partial^2/\partial z^2$ be replaced by $1/\Lambda$ and $1/\Lambda^2$. Finally, assume for simplicity that the curvature of the flow is small enough so that terms in $1/r$ or $1/r^2$ can be neglected except in the zero-order terms which determine the basic flow. When signs are taken into account, the continuity equation is converted to

$$\frac{U}{L} = \frac{W}{\Lambda} \tag{2.4.7}$$

The radial and axial scales L and Λ are probably best visualized as characteristic radii of curvature for the profiles in question. If the circular-Couette-flow model is taken seriously, these two scales in the r and z directions should be very nearly equal. They will eventually be determined by comparison with more rigorous analyses where these are available. For the present, we assume only that the scales L and Λ are proportional to the corresponding physical scales (d or δ, say, in the case of L; $\lambda/2$, say, in the case of Λ), with the *same* constant of proportionality. Hence Eq. (2.4.7) provides one relationship between the velocity scales U and W.

We propose to model the Laplace operator ∇^2 in Eqs. (2.4.2) and (2.4.3) using two positive constants, a and b, in an effort to provide enough flexibility to cope with the different effects of free or solid boundaries on the profile curvature (see Eqs. (2.4.15) and (2.4.20) below);

$$\nabla^2 = \frac{a}{L^2} + \frac{b}{\Lambda^2} = \frac{1}{L^2}\left[a + b\,\frac{L^2}{\Lambda^2}\right] \tag{2.4.8}$$

We now stipulate, as an implicit rule of the algebraic method, that an effective coefficient of unity should appear before each term representing a particular physical process, unless a different coefficient appears in the differential equations. When this rule is applied by requiring the expression (2.4.8) to reduce to the form $\nabla^2 = 1/L^2$ when $L/\Lambda = 1$, it follows that

$$a + b = 1 \tag{2.4.9}$$

If we somewhat arbitrarily associate constants like a and b with the process of differentiation rather than with the variable being differentiated, the definitions (2.4.4) and (2.4.5) are modeled by equations which call attention to the problem of ambiguity in sign;

$$\xi' = \frac{V}{\Lambda} \tag{2.4.10}$$

$$\eta' = \frac{bU}{\Lambda} + \frac{aW}{L} = \frac{U\Lambda}{L^2}\left[a + b\,\frac{L^2}{\Lambda^2}\right] \tag{2.4.11}$$

Note that the curl operator was applied once as curl **u** in generating Eq. (2.4.5) and thus Eq. (2.4.11). On the other hand, the Laplace operator in Eq. (2.4.8) began life as the vector operator div def **u**, or equivalently - curl curl **u**. Probably because the scales L and Λ are automatically raised to the proper powers, it seems to be sufficient to use the same constants a and b in both cases.

The two dynamical equations (2.4.2) and (2.4.3) now become

$$\bar{\rho}\bar{\zeta}U = \frac{\mu V}{L^2}\left[a + b\,\frac{L^2}{\Lambda^2}\right] \tag{2.4.12}$$

and

$$-2\,\bar{\rho}\bar{\omega}V = \mu\,\frac{U}{L^2}\,\frac{\Lambda^2}{L^2}\left[a + b\,\frac{L^2}{\Lambda^2}\right]^2 \tag{2.4.13}$$

These are hybrid equations. The quantities $\bar{\omega}$ and $\bar{\zeta}$ are still formally functions of r and will eventually have to be replaced by equivalent global constants characterizing the whole layer. Even without this replacement, the last two equations (2.4.12) and (2.4.13) become in some sense an algebraic abstraction of the eigenvalue problem. They are homogeneous in U and V, and the determinant must vanish if a meaningful solution is to exist. That is,

$$-\frac{2\,\bar{\rho}^2\bar{\omega}\bar{\zeta}L^4}{\mu^2} = \frac{\Lambda^2}{L^2}\left[a + b\,\frac{L^2}{\Lambda^2}\right]^3 \tag{2.4.14}$$

The combination of variables on the left in Eq. (2.4.14) is one form of the Taylor number. Rayleigh's inviscid criterion, that the product $\bar{\omega}\,\bar{\zeta}$ (or the derivative $d(r^2\bar{v}^2)/dr$) must be negative for instability, is replaced by the criterion that the product $\bar{\omega}\,\bar{\zeta}$ must be more negative than a specified constant which depends on viscosity, scale, and cell geometry. The expression (2.4.14), with $L/\Lambda = 1$, was originally used by Coles (1967) to show that the effect of geometry can be suppressed for circular Couette flow; i.e., that the two main portions of the stability boundary can be expressed each as a function of two dimensionless variables rather than the usual three.

Circular Couette flow is normally characterized by solid walls, or hard boundaries, at which a no-slip boundary condition is applied. For rotation in the same direction, which is the case of interest here, the minimum critical Taylor number is known to occur for essentially square cells; i.e., for $L/\Lambda = 1$. In order for the right-hand side of Eq. (2.4.14) to have its minimum when $L/\Lambda = 1$, it is necessary that

$$a - 2b = 0 \tag{2.4.15}$$

It follows, in view of Eq. (2.4.9), that $a = 2/3$ and $b = 1/3$. Thus, finally,

$$-\frac{2\bar{\rho}^2\bar{\omega}\bar{\zeta}L^4}{\mu^2} = \frac{1}{27}\frac{\Lambda^2}{L^2}\left[2 + \frac{L^2}{\Lambda^2}\right]^3 \tag{2.4.16}$$

It remains to determine how well this expression represents the effects of cell geometry on the stability boundary. Chandrasekhar (1961, p. 303) recommends a narrow-gap approximation which can be written in the present notation as

$$-\frac{2\rho^2\bar{\omega}\bar{\zeta}L^4}{\mu^2} = \frac{\left(\frac{L}{d}\right)^4 \pi^4 \frac{\Lambda^2}{L^2}\left[1 + \frac{L^2}{\Lambda^2}\right]^3}{1 - \frac{8\frac{L}{\Lambda}\left[1 + \cosh\left(\pi\frac{L}{\Lambda}\right)\right]}{\pi\left[1 + \frac{L^2}{\Lambda^2}\right]^2\left[\pi\frac{L}{\Lambda} + \sinh\left(\pi\frac{L}{\Lambda}\right)\right]}} \tag{2.4.17}$$

where $\bar{\zeta} = 2A$, as in Eq. (2.2.12), with $A < 0$, and where $\bar{\omega} = (\omega_o + \omega_i)/2$. The gap is $d = r_o - r_i$. When we require the minimum critical Taylor numbers to coincide in Eqs. (2.4.16) and (2.4.17), we find that

$$1715\left(\frac{L}{d}\right)^4 = 1 \quad or \quad \frac{L}{d} = 2\,\frac{\Lambda}{\lambda} = 0.155 \tag{2.4.18}$$

where λ is the axial wave length.

Equations (2.4.16) and (2.4.17) are both of the form

$$Ta = -\frac{2A\,\bar{\rho}^2\left(\omega_o + \omega_i\right)d^4}{\mu^2} = fn\left(\frac{2d}{\lambda}\right) \tag{2.4.19}$$

The two versions are compared in Fig. 2.1. The agreement is excellent (within about one percent) for $2d/\Lambda$ from zero to about unity, but deteriorates for large values of $2d/\Lambda$, where the asymptotic behavior is correct but the coefficient of the leading term according to the present model is about 20 percent too small.

A better approximation to a shear layer would be circular Couette flow with soft boundaries, at which a stress-free boundary condition is applied. This problem has apparently not been considered in the literature. However, an analogous problem is Benard convection with two free boundaries. For this case the cells are known to be rectangular at the minimum critical Rayleigh number, with $2d/\Lambda = 1/\sqrt{2}$ (Chandrasekhar, 1961, p. 36). If the right-hand side of Eq. (2.4.14) is required to have its minimum for $L/\Lambda = 1/\sqrt{2}$, it is necessary that

$$a - b = 0 \tag{2.4.20}$$

so that for this case $a = b = 1/2$ and

$$-\frac{2\bar{\rho}^2\bar{\omega}\bar{\zeta}L^4}{\mu^2} = \frac{1}{8}\frac{\Lambda^2}{L^2}\left[1 + \frac{L^2}{\Lambda^2}\right]^3 \tag{2.4.21}$$

In the present notation, Chandrasekhar's exact expression is

$$-\frac{2\bar{\rho}^2\bar{\omega}\bar{\zeta}L^4}{\mu^2} = \pi^4\left[\frac{L}{d}\right]^4\frac{\Lambda^2}{L^2}\left[1 + \frac{L^2}{\Lambda^2}\right]^3 \tag{2.4.22}$$

Comparison of the last two equations shows that

$$8\pi^4\left[\frac{L}{d}\right]^4 = 1 \quad or \quad \frac{L}{d} = 2\,\frac{\Lambda}{\lambda} = 0.189 \tag{2.4.23}$$

The final result in both cases is the same;

$$Ta = -\frac{2A\,\bar{\rho}^2\left(\omega_o + \omega_i\right)d^4}{\mu^2} = \frac{\pi^4\lambda^2}{4d^2}\left[1 + \frac{4d^2}{\lambda^2}\right]^3 \tag{2.4.24}$$

That the present estimate is exact is not entirely an accident. It helps to know the right answer. The form of the exact result was anticipated in choosing the signs in Eq. (2.4.11), although the signs are also consistent with solid-body rotation. The result was also anticipated when the same coefficients a and b were used in Eq. (2.4.8) and in Eq. (2.4.11).

Equation (2.4.24) is included in Fig. 2.1. The effect of the soft boundary condition is felt in the reduction in the critical Taylor number and also in the relaxation of the radii of curvature L/d and Λ/d when $\partial u/\partial r$ is not required to vanish at the boundaries.

2.5. Taylor-Görtler Instability; Different Densities

We now attempt the case of variable density. The pressure p' and density ρ' become variables, and seven equations are needed for the quantities $u', v', w', p', \rho', \xi', \eta'$. With curvature terms omitted, six of these are continuity;

$$\frac{\partial u'}{\partial r} + \frac{\partial w'}{\partial z} = 0 \tag{2.5.1}$$

$$u' \frac{d\bar{\rho}}{dr} + u' \frac{\partial \rho'}{\partial r} + w' \frac{\partial \rho'}{\partial z} = 0 \tag{2.5.2}$$

tangential momentum;

$$\bar{\rho}\, \bar{\zeta} u' = \mu \nabla^2 v' \tag{2.5.3}$$

and tangential vorticity;

$$-2\bar{\rho}\,\bar{\omega} \frac{\partial v'}{\partial z} = \frac{1}{\bar{\rho}} \left[\frac{\partial \rho'}{\partial z} \frac{d\bar{p}}{\partial r} - \frac{\partial p'}{\partial z} \left[\frac{d\bar{\rho}}{dr} + \frac{\partial \rho'}{\partial r} \right] \right]$$

$$+ \mu \left[\nabla^2 \eta' - \frac{\eta'}{r^2} \right] + \frac{\mu}{\bar{\rho}} \left[\frac{d\bar{\rho}}{dr} + \frac{\partial \rho'}{\partial r} \right] \nabla^2 w' \tag{2.5.4}$$

together with the two definitions (2.4.4) and (2.4.5) as before. Once again, the pressure can be bypassed, because the axial momentum equation,

$$0 = -\frac{\partial p'}{\partial z} + \mu \nabla^2 w' \tag{2.5.5}$$

immediately permits cancellation of the combination

$$\frac{1}{\bar{\rho}}\left[\frac{d\bar{\rho}}{dr}+\frac{\partial\rho'}{\partial r}\right]\left[-\frac{\partial\rho'}{\partial z}+\mu\nabla^2 w'\right]$$

in Eq. (2.5.4), which becomes

$$-2\bar{\rho}\bar{\omega}\frac{\partial v'}{\partial z}=\frac{1}{\bar{\rho}}\frac{\partial\rho'}{\partial z}\frac{d\bar{p}}{dr}+\mu\nabla^2\eta' \tag{2.5.6}$$

The various steps taken to obtain Eq. (2.4.14) may now be repeated to obtain

$$-\frac{\bar{\rho}^2L^4}{\mu^2}\left[2\bar{\omega}\bar{\zeta}+\frac{\Lambda}{V}\frac{\bar{\zeta}}{\bar{\rho}^2}\frac{d\bar{p}}{dr}\frac{\partial\rho'}{\partial z}\right]=\frac{\Lambda^2}{L^2}\left[a+b\left(\frac{L^2}{\Lambda^2}\right)^3\right] \tag{2.5.7}$$

There is one new baroclinic term which has so far not been processed. To bring this term under control, we first replace $d\bar{p}/dr$ by $\bar{\rho}\bar{v}^2/r$ according to Eq. (2.2.5). The derivative $\partial\rho'/\partial z$ can be estimated with the aid of Eq. (2.5.2), which implies that derivatives of mean and fluctuating densities are of the same order;

$$U\frac{d\bar{\rho}}{dr}=U\frac{\partial\rho'}{\partial r}=W\frac{\partial\rho'}{\partial z}=U\frac{\Lambda}{L}\frac{\partial\rho'}{\partial z} \tag{2.5.8}$$

Hence

$$-\frac{\bar{\rho}^2L^4}{\mu^2}\left[2\bar{\omega}\bar{\zeta}+\frac{\bar{\zeta}L}{V}\frac{\bar{v}^2}{\bar{\rho}r}\frac{d\bar{p}}{dr}\right]=\frac{\Lambda^2}{L^2}\left[a+b\left(\frac{L^2}{\Lambda^2}\right)^3\right] \tag{2.5.9}$$

We now require our analysis to include Synge's generalization (1933; see also the argument in Section 1 above) for variable density of Rayleigh's inviscid criterion $d(r^2\bar{v}^2)/dr = 0$; namely,

$$\frac{d}{dr}\left(\bar{\rho}r^2\bar{v}^2\right) = \bar{\rho}r^3\left(2\bar{\omega}\bar{\zeta} + \frac{\bar{v}^2}{\bar{\rho}r}\frac{d\bar{\rho}}{dr}\right) = 0 \tag{2.5.10}$$

The corresponding inviscid limit of Eq. (2.5.9) is obtained by setting the quantity in parentheses on the left-hand side equal to zero. For Synge's criterion to be recovered, it is necessary to put

$$V = \bar{\zeta}L \tag{2.5.11}$$

where it is understood that $\bar{\zeta}$ (and $\bar{\rho}$ below) should eventually be replaced by a suitable mean value for the layer. This relationship essentially defines V. The other two velocities are also defined, because from Eq. (2.4.12)

$$U = \frac{\mu}{\bar{\rho}L}\left(a + b\,\frac{L^2}{\Lambda^2}\right) \tag{2.5.12}$$

and from Eq. (2.4.7)

$$W = \frac{\mu}{\bar{\rho}L}\frac{\Lambda}{L}\left(a + b\,\frac{L^2}{\Lambda^2}\right) \tag{2.5.13}$$

The fact that the last three equations emerge from the analysis only when the density is allowed to vary is a consequence of the inhomogeneity of the more general system.

At this point the stability criterion, with part of the radial dependence not yet removed, is

$$-\frac{\bar{\rho}^2 L^4}{\mu^2}\left[2\bar{\omega}\,\bar{\zeta}+\frac{\bar{v}^2}{\bar{\rho}R}\,\frac{d\bar{\rho}}{dr}\right]=\frac{\Lambda^2}{L^2}\left[a+b\,\frac{L^2}{\Lambda^2}\right]^3 \qquad (2.5.14)$$

where R is a mean radius. This expression (2.5.14) can be interpreted as a relationship between frequencies or times. The prefix $\bar{\rho}^2L^4/\mu^2$ is the square of a diffusion time. The quantities $\bar{\omega}$ and $\bar{\zeta}$ are rotation rates. The quantity $(\bar{v}^2/\bar{\rho}R)\,d\bar{\rho}/dr$ is the square of a Brunt-Väisälä frequency, with the variable body force per unit mass $d\bar{p}/\bar{\rho}dr = \bar{v}^2/r$ playing the role normally played by the gravitational acceleration g.

Finally, we note that a positive radial density gradient $d\bar{\rho}/dr > 0$ is stabilizing, because it moves the stability boundary to higher (absolute) magnitudes for $\bar{\omega}$ and/or $\bar{\zeta}$, other things being equal. A negative radial density gradient can destabilize a flow (for example, irrotational flow) which would be stable for constant density. These observations will be important in the interpretation of the experimental data of the present research in Section 8.

2.6. Kelvin-Helmholtz Instability; Constant Density

Consider next the Kelvin-Helmholtz instability, for which the secondary motion is periodic in the θ direction and two-dimensional ($w = 0$, $\partial/\partial z = 0$). For the case of constant density, the dependent variables are u', v', p', ζ', and the four equations required, with curvature terms omitted, are

$$\frac{\partial u'}{\partial r}+\frac{\partial v'}{\partial x}=0 \qquad (2.6.1)$$

$$\bar{\rho}\left[\frac{\partial v'}{\partial t}+\bar{\zeta}u'+\bar{v}\,\frac{\partial v'}{\partial x}\right]=-\frac{\partial p'}{\partial x}+\mu\nabla^2 v' \tag{2.6.2}$$

$$\bar{\rho}\left[\frac{\partial \zeta'}{\partial t}+u'\,\frac{d\bar{\zeta}}{dr}+\bar{v}\,\frac{\partial \zeta'}{\partial x}\right]=\mu\nabla^2\zeta' \tag{2.6.3}$$

$$\zeta'=\frac{\partial v'}{\partial r}-\frac{\partial u'}{\partial x} \tag{2.6.4}$$

where dx is written for $r\,d\theta$. Note that the term in $d\bar{\zeta}/dr$ is retained in Eq. (2.6.3), in spite of the fact that the derivative vanishes for the basic profile (2.2.10). The reason is that this is the term which incorporates the extreme sensitivity of the flow to the presence of an inflection point in the mean profile.

The secondary motion, and the methods used to describe it, are quite different from the ones of the previous section. We anticipate a long, thin cat's-eye pattern, periodic in the θ- or x-direction and stationary in a coordinate system translating with the phase velocity c. The nonsteady terms are disposed of by observing that any function φ, say, which depends on the composite argument $(x-ct)$ satisfies $\partial\varphi/\partial t+c\,\partial\varphi/\partial x=0$. Hence

$$\frac{\partial\varphi}{\partial t}+\bar{v}\,\frac{\partial\varphi}{\partial x}=(\bar{v}-c)\,\frac{\partial\varphi}{\partial x} \tag{2.6.5}$$

In the continuity equation, the derivatives $\partial/\partial r$ and $\partial/\partial x$ are not expected to have the same scale, and are again represented by $1/L$ and $1/\Lambda$, respectively, as in the case of the Taylor-Görtler problem. The pressure perturbation can be left unattended in Eq. (2.6.2). We represent the continuity equation by

$$\frac{U}{L} = \frac{V}{\Lambda} \tag{2.6.6}$$

but we choose to use different constants in the Laplacian and in the axial vorticity;

$$\nabla^2 = \frac{A}{L^2} + \frac{B}{\Lambda^2} = \frac{1}{L^2}\left[A + B\,\frac{L^2}{\Lambda^2}\right] \tag{2.6.7}$$

and

$$\zeta = \frac{aV}{L} + \frac{bU}{\Lambda} = \frac{U\Lambda}{L^2}\left[a + b\,\frac{L^2}{\Lambda^2}\right] \tag{2.6.8}$$

with no constraint on a, b, A, B for the present except that these quantities are all positive. There is obtained

$$\bar{\rho}\left[U\,\frac{d\bar{\zeta}}{dr} + \frac{U(\bar{v}-c)}{L^2}\left[a + b\,\frac{L^2}{\Lambda^2}\right]\right] = \mu\,\frac{U\Lambda}{L^4}\left[a + b\,\frac{L^2}{\Lambda^2}\right]\left[A + B\,\frac{L^2}{\Lambda^2}\right] \tag{2.6.9}$$

This equation is intended to characterizes the Kelvin-Helmholtz instability without second-order curvature effects, although these could be included with a little more effort. The two quantities $d\bar{\zeta}/dr$ and $(\bar{v} - c)$ have to be disposed of. The first can be treated normally, say by putting

$$\frac{d\bar{\zeta}}{dr} = \frac{\Delta\bar{v}}{L^2} \tag{2.6.10}$$

where $\Delta\bar{v} = (\bar{v}_o - \bar{v}_i)$. The quantity $(\bar{v} - c)$ is antisymmetric about the

midplane; it is measured by $(\bar{v}_o - c)$ on one side and by $(c - \bar{v}_i)$ on the other. An estimate will be made in Section 7 of the celerity c, showing how this quantity depends on density ratio. In the meantime, $(\bar{v} - c)$ should be well enough measured by its arithmetic mean, $(\bar{v}_o - \bar{v}_i)/2$, and we therefore put

$$\bar{v} - c = -\frac{\Delta\bar{v}}{2} \tag{2.6.11}$$

The sign in Eq. (2.6.11) is chosen to be negative, in anticipation of the fact that the left-hand side of Eq. (2.6.9) must vanish when $\mu = 0$. At this stage, Eq. (2.6.9) has become

$$\frac{\bar{\rho}\Delta\bar{v}L}{\mu}\left[\left(1 - \frac{a}{2}\right) - \frac{b}{2}\frac{L^2}{\Lambda^2}\right] = \frac{\Lambda}{L}\left[a + b\,\frac{L^2}{\Lambda^2}\right]\left[A + B\,\frac{L^2}{\Lambda^2}\right] \tag{2.6.12}$$

There are several constants to be accounted for; a, b, A, B, L. One well-established property of the neutral stability curve, at least for a mean profile given by a hyperbolic-tangent function, is that the flow is stable if

$$\alpha = \pi\,\frac{\delta}{\lambda} = \pi\,\frac{L}{\Lambda} > 1 \tag{2.6.13}$$

when δ is defined as the maximum-slope thickness (because the cells are not counter-rotating, there is no factor of two). We want our algebraic model to reproduce the asymptotic form of the stability boundary near the upper branch (Drazin and Reid 1981, especially Fig. 4.28 and Prob. 4.13); i.e.,

$$\mathrm{Re}\,(1 - \alpha) = 8\pi \tag{2.6.14}$$

Note that the Reynolds number $\mathrm{Re} = \bar{\rho}\Delta\bar{v}\,\delta/\mu$ used here is larger by a factor of four than the Reynolds number used by Drazin and Reid. Let Eq. (2.6.12) be rewritten as

$$\frac{\bar{\rho}\Delta\bar{v}\,\delta}{\mu}\left[1-\left(\frac{b}{2-a}\right)^{\frac{1}{2}}\frac{\alpha}{\pi}\right]=\frac{\delta}{L}\,\frac{\left[a+b\,\frac{\alpha^2}{\pi^2}\right]\left[A+B\,\frac{\alpha^2}{\pi^2}\right]}{\left[1-\frac{a}{2}\right]\frac{\alpha}{\pi}\left[1+\left(\frac{b}{2-a}\right)^{\frac{1}{2}}\frac{\alpha}{\pi}\right]} \tag{2.6.15}$$

The left-hand side will reduce to the form $\mathrm{Re}\,(1-\alpha)$ provided that

$$\pi^2\left[\frac{2-a}{b}\right]=1 \tag{2.6.16}$$

and the right-hand side (with $\alpha = 1$) will then reduce to the constant 8π provided that

$$\frac{\left[\pi^2 A+B\right]}{4b}=\frac{L}{\delta} \tag{2.6.17}$$

It remains to consider the existence of a minimum critical Reynolds number and the value of the wave number α for which it occurs. For the temporal problem, with a hyperbolic-tangent profile, Betchov and Szewczyk (1963) found a neutral boundary passing through the origin. Thus there was no finite minimum critical Reynolds number and no lower branch. Lessen and Ko (1966) used the Blasius profile and found a minimum Reynolds number of 9.1 (i.e., 3.6/.395 when the thickness δ is rescaled to put the asymptote for the upper branch at $\alpha = 1$) at a wave number of about 0.13 (i.e., 0.05/.395). The analytical evidence is therefore unclear at this stage of the argument.

We need some estimates. Suppose that we require a balance between the two terms in Eq. (2.6.8) which contribute to the vorticity by assuming $a = b$. as in the case of the Taylor-Görtler flow with free boundaries. It then follows from Eq. (2.6.16) that

$$a = b = \frac{2\pi^2}{\pi^2 + 1} \tag{2.6.18}$$

and from Eqs. (2.6.15) and (2.6.17) that

$$\mathrm{Re} = \frac{16\pi(\pi^2 + \alpha^2)(\pi^2 A + B\alpha^2)}{(\pi^2 + 1)(\pi^2 A + B)\,\alpha\,(1 - \alpha^2)} \tag{2.6.19}$$

This expression has only one disposable constant, the ratio B/A. It turns out to be possible to choose this constant so that both the minimum critical Reynolds number and the corresponding wave number agree well with the results in Fig. 3 of Lessen and Ko (1966). The condition for a minimum is

$$\frac{B}{A} = \frac{\pi^2}{\alpha^2}\left[1 - \frac{4(1 + \pi^2)\alpha^2}{\pi^2 + (\pi^2 + 3)\,\alpha^2 - \alpha^4}\right] \tag{2.6.20}$$

If we estimate $\alpha = 1/8$ (i.e., close to 0.13), then B/A is nearly $64\pi^2 >> 1$, and Re from Eq. (2.6.19) is about 4π. These values for α and Re are satisfactory. As the last condition to be imposed, we choose the same one used to measure the magnitude of the Laplacian for the Taylor-Görtler problem; namely,

$$A + B = 1 \tag{2.6.21}$$

Given that B is nearly unity, and much larger than $\pi^2 A$, Eq. (2.6.17) becomes

approximately $L/\delta = 1/4b = (\pi^2 + 1)/8\pi^2$, or about $1/8$. This value is also satisfactory.

After some experimentation, the values $\alpha = 0.097$, $B/A = 1006$, $\mathrm{Re} = 9.0$, $A = 0.001$, $B = 0.999$, and $L/\delta = 0.139$ have been used to construct the stability boundary which is compared in Fig. 2.2 with the boundary proposed by Lessen and Ko. The fit is at least amiable, in view of the difficulty of the problem.

The results just obtained need some discussion. The enormous discrepancy between the constants A and B seems at first to be against nature, especially since the algebraic representation for the Laplace operator in Eq. (2.6.7) reduces in the limit $A \to 0$ to the form $\partial^2\zeta'/\partial x^2$, rather than the form $\partial^2\zeta'/\partial y^2$ which would emerge from a boundary-layer approximation. Note that the formula obtained from Eq. (2.6.19) with $A = 0$; namely,

$$\mathrm{Re} = \frac{16\pi\alpha\,(\pi^2 + \alpha^2)}{(\pi^2 + 1)(1 - \alpha^2)} \tag{2.6.22}$$

requires the curve $\mathrm{Re}\,(\alpha)$ to pass through the origin. The lower branch is lost, as in the calculations by Betchov and Szewczyk (1963). Their results are compared in Fig. 2.2 with the curve defined by Eq. (2.6.22); note that the latter equation, unlike Eq. (2.6.19), has no adjustable constants.

The relative magnitude of the terms $\partial^2\zeta'/\partial x^2$ and $\partial^2\zeta'/\partial y^2$ is not discussed by any of the authors whose stability calculations have been cited. However, this question can be studied in terms of Stuart's closed-form expression (1967) for an inviscid motion of the type considered here. Stuart's stream function for perturbations of small amplitude is of the form

$$\psi = \frac{\cos x}{\cosh y} \tag{2.6.23}$$

so that

$$\frac{\partial^2 \zeta}{\partial x^2} = \cos x \left[\frac{\sinh^2 y}{\cosh^3 y} \right] \tag{2.6.24}$$

$$\frac{\partial^2 \zeta}{\partial y^2} = \cos x \left[\frac{2 - 9 \sinh^2 y + \sinh^4 y}{\cosh^5 y} \right] \tag{2.6.25}$$

Our algebraic approach deals with characteristic values for the whole layer, values perhaps best visualized as integrals from $y = 0$ to $y = \infty$, say. Because $\partial\zeta/\partial y$ vanishes at infinity and also at $y = 0$ for the asymmetric tanh profile, the integral of $\partial^2\zeta/\partial y^2$ is zero, whereas the integral of $\partial^2\zeta/\partial x^2$ is $\pi/4$. We believe that this observation explains why Betchov and Szewczyk, working with the hyperbolic-tangent profile, found no lower branch ($A \neq 0$), whereas Lessen and Ko, working with the not-quite-asymmetric Blasius profile, did find a lower branch and a minimum critical Reynolds number ($A = 0$ but $A << B$). This behavior suggests a singular-perturbation problem. There is a non-uniform validity of the neutral boundary for long waves or small α. The lower branch is a boundary layer, and is lost when one of the highest-order terms in the equations ceases to play a role. It is because of the exquisite sensitivity of the minimum critical Reynolds number to the departure of the basic profile from perfect antisymmetry that we have chosen to emphasize wave number rather than Reynolds number in our fit to the analytic results obtained by Lessen and Ko.

2.7. Kelvin-Helmholtz Instability; Different Densities

The last and most difficult element of the algebraic method is inclusion of the effects of a density difference in the neutral-stability condition (2.6.19) for the Kelvin-Helmholtz problem. The new variable is ρ', making five dependent variables in all. The new equation is the linearized continuity equation, Eq. (2.2.23), which is most conveniently written as

$$u' \left(\frac{d\bar{\rho}}{dr} + \frac{\partial \rho'}{\partial r} \right) + (\bar{v} - c) \frac{\partial \rho'}{\partial x} = 0 \tag{2.7.1}$$

The linearized equations (2.6.1), (2.6.2), and (2.6.4) are unchanged, but the spanwise vorticity equation (2.6.3) becomes much more complicated. With curvature terms omitted, this equation is

$$\bar{\rho} \left[u' \frac{d\bar{\zeta}}{dr} + (\bar{v} - c) \frac{\partial \zeta'}{\partial x} \right] = \mu \nabla^2 \zeta' - \frac{1}{\bar{\rho}} \frac{\partial \rho'}{\partial x} \frac{d\bar{p}}{dr}$$

$$+ \frac{1}{\rho} \left(\frac{\partial p'}{\partial x} - \mu \nabla^2 v' \right) \left(\frac{d\bar{\rho}}{dr} + \frac{\partial \rho'}{\partial r} \right) + \frac{\mu}{\rho} \left(\frac{\partial \rho'}{\partial r} \frac{d\bar{\zeta}}{dr} + \rho' \frac{d^2 \bar{\zeta}}{dr^2} \right) \tag{2.7.2}$$

The transformation to moving coordinates according to Eq. (2.6.5) has already been carried out. When various variables are replaced by constants according to Eqs. (2.6.6)-(2.6.11), but no other steps are taken, Eq. (2.6.12) becomes

$$\frac{\bar{\rho} \Delta \bar{v} L}{\mu} \left[\left(1 - \frac{a}{2} \right) - \frac{b}{2} \frac{L^2}{\Lambda^2} \right] = \frac{\Lambda}{L} \left(a + b \frac{L^2}{\Lambda^2} \right) \left(A + B \frac{L^2}{\Lambda^2} \right) - \frac{L^3}{\bar{\rho} \mu U} \frac{\partial \rho'}{\partial x} \frac{d\bar{\rho}}{dr}$$

$$+ \frac{L^3}{\bar{\rho}\mu U}\left[\frac{\partial p'}{\partial x} - \mu \nabla^2 v'\right]\left[\frac{d\bar{\rho}}{dr} + \frac{\partial \rho'}{\partial r}\right] + \frac{L^3}{\bar{\rho} U}\left[\frac{\partial \rho'}{\partial r}\frac{\Delta \bar{v}}{L^2} + \rho' \frac{d^2\bar{\zeta}}{dr^2}\right] \tag{2.7.3}$$

The pressure perturbation $\partial p'/\partial x$ in the third term on the right-hand side of this equation can be eliminated with the aid of Eqs. (2.6.2) and especially (2.6.6). With an appropriate choice of sign,

$$\frac{\partial p'}{\partial x} - \mu \nabla^2 v' = \frac{1}{2}\frac{\bar{\rho} U \Delta \bar{v}}{L} \tag{2.7.4}$$

Note that this term represents a vorticity source which is partly baroclinic and partly exoclinic, according to Eq. (2.1.5).

The baroclinic density perturbation $\partial \rho'/\partial x$ in the second term can be eliminated with the aid of Eq. (2.7.1). With an appropriate choice of sign and with a disposable constant k inserted to allow adjustment of the gradient Richardson number toward the critical value $Ri = 1/4$, the relationship wanted is

$$\frac{\partial \rho'}{\partial x} = k \frac{U}{\Delta \bar{v}}\left[\frac{d\bar{\rho}}{dr} + \frac{\partial \rho'}{\partial r}\right] \tag{2.7.5}$$

The other constants of the problem have already been assigned specific values, either in Eq. (2.6.18) or in the preparation of Fig. 2.2 for the case of constant density.

Suppose now that the derivative $\partial \rho'/\partial r$ in Eqs. (2.7.3) and (2.7.5) is small compared with $\partial \bar{\rho}/dr$. The rationalization proposed here is that each fluid is confined mainly to one side of the layer in a cat's-eye pattern, rather than circulating freely from one side of the layer to the other, as in the case of Taylor-Gortler cells. In the event that the derivatives are actually of the same order,

the rules of the algebraic method require them to be treated together and combined into a single term.

Finally, it is necessary to account for the last term in Eq. (2.7.3). This viscous term represents the remainder of the exoclinic vorticity source in Eq. (2.1.5). If the two contributions are of the same nature and the same order, it is sufficient to keep only the first. After replacing $\partial\rho'/\partial r$ by $(\Lambda/L)\partial\rho'/\partial x$ and using Eq. (2.7.5), our conclusion is that this term is of the same order as terms which appear for the case of constant density and should not be neglected.

At this stage, the left-hand side of the generalization of Eq. (2.6.12), with $\bar{\rho}\bar{v}^2/R$ substituted for $d\bar{\rho}/dr$ and (temporarily) $d\bar{v}/dr$ substituted for $\Delta\bar{v}/L$, has become

$$\frac{\bar{\rho}\Delta\bar{v}L}{\mu}\left[\left(1-\frac{a}{2}\right)-\frac{b}{2}\frac{L^2}{\Lambda^2}-k\,\frac{\bar{v}^2/R}{(d\bar{v}/dr)^2}\,\frac{1}{\bar{\rho}}\,\frac{d\bar{\rho}}{dr}-\frac{1}{2}\,\frac{\Delta\bar{\rho}}{\bar{\rho}}\right]$$

or, after multiplying through by $2/(2-a)=\pi^2+1$,

$$\frac{\bar{\rho}\Delta\bar{v}L}{\mu}\left[1-\alpha^2+k(\pi^2+1)\,Ri-\frac{(\pi^2+1)}{2}\,\frac{\Delta\bar{\rho}}{\rho}\right]$$

where

$$Ri=\frac{\bar{v}^2/R}{(d\bar{v}/dr)^2}\,\frac{1}{\bar{\rho}}\,\frac{d\bar{\rho}}{dr}=\frac{N^2}{(d\bar{v}/dr)^2} \tag{2.7.6}$$

is the Richardson number and N is the Brunt-Väisälä frequency. The sign is opposite to the one normally found because the body force here is in the direction of increasing r rather than decreasing r.

For large Reynolds numbers, the upper branch of the neutral stability boundary has an asymptote which can be obtained from

$$\alpha^2 = 1 - k(\pi^2 + 1)Ri - \frac{(\pi^2 + 1)}{2}\frac{\Delta\bar{\rho}}{\bar{\rho}} \qquad (2.7.7)$$

If the last term is ignored for the moment, as in most dicussions of the formal eigenvalue problem, the constant k is determined by the condition that an inviscid flow is unconditionally stable if $Ri > 1/4$ (e.g., Drazin and Reid 1981, p. 327). Hence we put

$$k = \frac{4}{\pi^2 + 1} \qquad (2.7.8)$$

We have, finally, for the heterogeneous flow

$$\mathrm{Re} = \frac{16\pi\left[(\pi^2 + \alpha^2)(\pi^2 A + B\alpha^2) - 2\pi^2\alpha^2\frac{\Delta\bar{\rho}}{\bar{\rho}}\right]}{(\pi^2 + 1)(\pi^2 A + B)\alpha\left[1 - \alpha^2 - 4Ri - \frac{(\pi^2 + 1)}{2}\frac{\Delta\bar{\rho}}{\rho}\right]} \qquad (2.7.9)$$

(need to discuss static case of Rayleigh-Taylor instability)

This result can be compared approximately with exact calculations by Maslowe and Thompson (1971). These authors derived their density distribution from a temperature distribution, and their calculations are for $Pr = 0.72$ (our formulation corresponds to $Pr = \infty$). Moreover, a Boussinesq approximation was made, with density variations being neglected except in the gravity term which generates the Richardson number; i.e., the term in $\frac{\partial\rho'}{\partial x}\frac{d\bar{p}}{dr}$ in our Eq. (2.7.3). For compatibility, the two terms in $\Delta\bar{\rho}/\bar{\rho}$ should be dropped from Eq.

(2.7.9). Finally, the parameter J_o of Maslowe and Thompson is the maximum value of the local Richardson number, but is presumably equivalent here to a value based on the maximum slope of the velocity and density distributions.

With these reservations, neutral curves have been calculated for various Richardson numbers. They are compared with the curves obtained by Maslowe and Thompson in Figure 2.3. The agreement is only qualitatively acceptable, given the difficulty with small wave numbers discussed above in connection with Kelvin-Helmholtz instability for the case of constant density. A serious problem is that Eq. (2.7.9) requires the lower branch to be asymptotic to the line $\alpha = 0$ as $\mathrm{Re} \to \infty$, independent of the value of Ri.

III. Experimental Facility and Instrumentation

The experiments were conducted in the gas shear-layer facility designed by Brown and Roshko (1971, 1974). Slight modifications were made to the nozzle blocks and splitter plate in order to install the curved channel walls for this experiment. The resulting configuration is shown in Fig. 3.1.

Two gas streams from bottles are brought into the nozzles through pressure regulators, metering valves, settling chambers, and honeycombs and screens. The two streams meet at the end of the splitter plate and there the mixing layers start to develop.

Due to space limitations in the basic facility, the nozzle section used for this experiment is non-symmetric. The splitter plate is curved for the first 10.8 centimeters, as shown in Fig. 3.2. The downstream part of the splitter plate (9 cm long) is straight until it meets the sharp trailing edge, which is 0.01 cm thick and subtends an angle of 4 degrees. To permit photography in two directions, two curved channel walls, with radii of curvature 27.9 and 33.0 cm, respectively, are made from transparent lucite plates 0.25 cm thick. The two curved walls are hinged to the nozzle blocks and the gap is sealed with plastic tape.

To keep effluent gases away from the light path during flow-visualization experiments, curved aluminum guide vanes connect the curved walls to the exit port of the channel. With the splitter plate pointing at the center of the inlet, the curved test section is 5.08 cm high and 10.16 cm wide, with a mean radius of curvature of 30.5 cm. The channel is 23 cm long and turns 43 degrees.

The curved lucite walls were made by a heat forming process. An oversized flat lucite sheet (without backing paper) was clamped at the ends within a four-roller fixture, as shown in Fig. 3.3. The correct radius of curvature was obtained by adjusting the rollers, which applied a pure moment to the center part of the plate. The whole assembly was then heated in an oven and held at a temperature of 93 ~ 96 °C for ten hours to release the stress within the lucite material. The center part of the product obtained was optically and mechanically satisfactory and was cut out for use.

Three bottled gases were used during this experiment. They are helium, nitrogen, and a mixture of 67.2 percent argon and 32.8 percent helium by volume. The first and second gases have a molar weight ratio of 6.999 and were used for experiments with different densities. The second and third gases have a molecular weight ratio of 1.006 and were used for experiments with equal densities. In both cases, the difference in index of refraction makes flow visualization possible by shadowgraph or schlieren methods. During the experiments, the test section is covered by two glass walls. The entire channel is then enclosed in a tank and pressurized to four atmospheres by house air. The elevated pressure provides high Reynolds numbers and enhances the difference in index of refraction which is exploited for flow-visualization purposes. Visual access to the test section is provided through two round glass windows 19 cm in diameter installed in the tank wall.

The experimental study emphasizes flow visualization. Conventional shadowgraph methods were employed in some of the experiments, using the arrangement shown in Fig. 3.4. Space limitations prevented installing mirrors at 45 degrees on both sides of the curved channel, as was done by Konrad (1976) and Bernal (1981). As a result, only one 45-degree mirror was used, and the plan view was exposed on a separate sheet of negative film inserted next to the

curved channel. The experiments were carried out in absolute darkness and were not very enjoyable. Several pictures obtained using this arrangement will be presented in Section 5 below. The quality of the side-view pictures is good, especially because of the short exposure obtained from a spark gap light source. However, most of the plan-view pictures obtained using this arrangement are poor. The close proximity of the plan-view negative film to the flow significantly reduces the distance travelled by the light which has passed through the flow. Hence less shadowgraph effect is obtained.

An additional incentive for development of a new optical arrangement was the need to take motion pictures of the flow. It goes without saying that a movie carries much more information about the motion than a still picture. With the arrangement shown in Fig. 3.4, however, motion pictures are not possible.

A double-pass focussed shadowgraph system was thus developed, as shown in Fig. 3.5. An image of a short-arc light source is placed at the focal point of the spherical mirror (focal distance 1270 mm), and parallel light is directed into the test section. Two flat mirrors are mounted inside the facility at the positions where the negatives were located in the original set-up. These mirrors reflect the incoming light so that it passes through the flow a second time and makes conventional photography possible. The spherical mirror collects the returning light and brings it to a focus. The flat mirrors are tilted slightly, by 0.15 degrees, so that the returning light is focused slightly away from the original focal point. The separation of the two focal points allows a small flat mirror to be inserted so that light is directed into the camera.

In contrast to ordinary photography, in which the object emits diffused light, shadowgraph images are mostly formed by undeflected parallel light. It is necessary to position the camera lens as close to the small deflecting mirror as possible, in order to cover the whole field of view with camera lenses

commercially available. However, the real image of the flow formed by the spherical mirror is behind the camera. Camera lens mounts are not normally designed for such an application, and cannot bring the image into focus without some correction. In the present case the correction is provided by inserting a negative lens (f = - 70 mm) in front of the camera lens (f = 25 mm). The focal length of the camera lens is thus increased. In other words, the camera was myopic, or near-sighted, until it was given the negative lens as a spectacle.

In the original shadowgraph method the negative film was placed against the test-section windows, and the contrast was sometimes low if there was little variation in the gradient of index of refraction. In such circumstances the contrast can be increased by placing the negative away from the test section, in order to increase the displacement of the deflected light. The best location for the negative has to be determined by trial and error. In the present system the focal plane of the camera lens is adjustable, and the contrast of the shadowgraph pictures can be varied by placing the object plane at a suitable distance from the test section. Tests were carried out for several of the curved mixing layers. Depending on the flow, it appears that the best location for the object plane is not on the test section window, but at a distance of 10 to 20 cm on the camera side of the window.

Flow conditions for our experiments are described by using the flow speed at the nozzle exit as reference. Prior to each experiment, pitot-static tubes connected to a pressure transducer (Datametrics Barocel, range 10 mm Hg) were inserted into the test section to measure this reference speed. The mean-velocity distributions across the nozzle exits were found to be uniform to within one percent.

Detailed concentration profiles and dynamic-pressure profiles were also measured for several of the flow cases studied. Gas aspiration probes used for

the concentration measurements were made as shown in Fig. 3.6. The basic design of this probe is similar to that of Brown and Rebollo (1972). A glass micro-sampling pipet (Corning, 10 microliters) with an inside diameter of 0.4 mm is first pierced with a bright-hot tungsten wire to form a through hole normal to the axis of symmetry on the centerline. One end of the pipet is then trimmed and fused, using a Bunsen burner, until the inner diameter shrinks to about 0.05 mm and forms a small nozzle. The exterior of the nozzle end is then ground to improve the slenderness ratio, and a piece of Wollaston wire (Pt-10% Rh) is inserted into the through hole. After attaching conductors to both ends, the Wollaston wire is etched by sucking nitric acid thorugh the nozzle with a Venturi-tube aspirator to remove the silver coating. The etched wire in the concentration probe is 2.5 μm in diameter. The response time of the probe is less than 0.1 msec. Overall accuracy of the probe after static calibration is within one percent.

The same Barocel pressure transducer and pitot-static tube were used for measurement of dynamic-pressure profiles. The variation of tunnel pressure and flow temperature were monitored by a second pressure transducer (Daystrom-Wiancko Model P2-1251, range 300 psig) and a thermocouple (copper-constantan, 0.05 mm dia.). The Joule-Thompson effect caused the temperature of the gases coming out of the high-pressure bottles to be generally different from the bottle temperature. This temperature difference is especially significant for the nitrogen used in our experiments. However, the pipelines and reservoirs downstream from the pressure regulators provide a considerable volume, in which the pressure is generally much lower than the bottle pressure. Thermal masses associated with the pipelines also help to reduce the temperature departure. It was found that the temperature drop in nitrogen in our facility was less than 2°C if the running time at 4 atmospheres was shorter than 6 seconds and the mean flow speed was lower than 700 cm/sec. The temperature

variation can cause errors in the concentration measurements through its effect on the hot-wire inside the aspiration probe. The same is true for tank pressure variations. Fortunately, the tank pressure was quite constant, and minor variations of 0.3 psi are not harmful to the concentration-probe measurements.

The concentration probe, the pitot-static tube, and the thermocouple were mounted on a traversing mechanism during the profile measurements. The outputs of all the transducers were sampled by computer through an A/D converter. The computer also controlled the motion of the traversing mechanism, so that sampling was done only when the probes were stationary at predetermined radial locations. During each run, 15 radial stations were traversed. At each station, 4096 data words were obtained for the concentration signal and for the dynamic-pressure signal at a sampling rate of 33.3 kHz per channel, with the two signals multiplexed. Together with 16 flow-temperature and 16 tank-pressure measurements interleaved with the high-speed data records, the whole experiment ran no longer than 5.75 seconds. The information obtained was stored on magnetic tape after the flow was turned off by the computer. The profiles of mean concentration and dynamic pressure reported in Section 6 were calculated from these data.

IV. Organization of the Experiment

A two-dimensional curved turbulent mixing layer can be described by three independent parameters. These are the ratio of inlet speeds, U_o/U_i, the ratio of densities, ρ_o/ρ_i, and the geometric factor b/R, where b is the half-height of the channel and R is the mean radius of curvature, as shown in the sketch at the beginning of Section 1. For consistency with the existing literature, the notation used in the remainder of this thesis is different from the notation used in Section 2 above. We will denote the streamwise (tangential) coordinate by x and the normal (radial) coordinate by y. The x-component of velocity will be represented by U or u, and the y-component of velocity by V or v.

End effects might be minimized by making the channel long enough so that the mixing layers do not leave the channel until the two streams are well mixed. However, due to large variation in flow parameters for the various mixing layers studied here, together with the limitation of space in the existing facility, this requirement cannot be satisfied for some flows in which the mixing layers grow too slowly. For this reason, none of the flow-visualization and profile measurements of the present experiments covered more than the first 60 percent of the flow field.

If viscosity is neglected, any mean flow property W can be represented by the functional relationship

$$W = W\left(\frac{x}{R}, \frac{y}{b}; \frac{U_o}{U_i}, \frac{\rho_o}{\rho_i}, \frac{b}{R}\right). \qquad (4.0.1)$$

The available speed ratios are limited primarily by the flow capacity of the tunnel at high speed and by unsteadiness of the downstream pressure-regulator valve at low speed. As a result, the range of speed ratios achievable is roughly from 1/4 to 4. Three gases were used and gave three possible density ratios; 7, 1, and 1/7. Except for one special sequence of measurements, described in Section 7.1, b/R was fixed throughout the experiment at the value 1/12.

The flow conditions can therefore be represented on a two-dimensional plane with $\left[\frac{U_o}{U_i}\right]$ as horizontal axis and $\left[\frac{\rho_o}{\rho_i}\right]$ as vertical axis, as shown in Fig. 4.1. Capital letters are used as symbols to indicate the flow conditions selected for this study. The flow conditions for these experiments are also listed in Table 1. All of the experiments were carried out at 4 atmospheres. Pairs like B and $\tilde{B}$ are flows having the same speed and density combinations. The dashed line in Fig. 4.1 corresponds to the condition $\rho_i U_i^2 = \rho_o U_o^2$. Flows for which high-speed movies were taken are denoted by enclosing the flow symbol in a circle. Flows for which profiles of mean velocity and mean concentration are available are denoted by enclosing the flow symbol in a square.

The flow Reynolds number depends on the fluid kinematic viscosity and a characteristic length scale, the thickness of the mixing layer. Neither of these two quantities can be uniquely determined in the present case. For a general mixing layer composed of two streams of different fluids, the kinematic viscosity is not a constant. The mixing-layer thickness, no matter how it is defined, grows with downstream distance. Hence there is a certain arbitrariness in any estimate of the Reynolds number. If the kinematic viscosity is taken to be the average of the kinematic viscosities for the two fluids, and the characteristic length scale is taken to be the visual thickness of the mixing layer 10 cm downstream of the splitter plate, the Reynolds numbers in this experiment covered the range

$1 \times 10^3 \sim 7 \times 10^4$. Figure 4.1 and Table 1 are central to the discussion of the experiment and are referred to frequently in what follows.

V. Visual Characteristics of Curved Mixing Layers

High-speed movies at 2000 frames per second have been taken of several of the flows cataloged in Fig. 4.1, using the double-pass focused shadowgraph system developed for the curved mixing layer and described in Section 3. A high-speed camera (Hycam model K2054E) with a 25-mm lens was employed for this purpose. Some of the pictures presented in this thesis are individual frames from these high-speed movies. The rest of the pictures were obtained using the traditional shadowgraph method. The latter pictures contain more detail in the side view of the flow, due to better resolution and shorter exposure. The negative size of these pictures is 12.7 x 17.8 cm, while the movie films are 1.6 cm wide, with actual image size roughly 0.6 cm in diameter. A photographic montage of the various flows studied here is presented in Figs. 5.1(a)-5.1(i). These flows will now be discussed systematically, with one parameter in the discussion changing at a time.

5.1. Flows With Uniform Density

The simplest case has a density ratio equal to unity. A picture of a flow with a velocity ratio also equal to unity is shown in Fig. 5.1(e) (middle). The inner stream is nitrogen and the outer stream is a helium-argon mixture which has the same density as nitrogen. Both streams are flowing at 400 cm/sec at 4 atmospheres. Except for slight departures from uniform velocity as a result of variation in the potential flow external to the mixing layer, the only major disturbance in the flow is the wake downstream from the splitter plate. According to the high-speed movies, the two sides of this curved wake behave differently. There seems to be more activity on the inner side of the layer. The outer side is

less active, and the outer pattern seems to convect downstream with little change. The main role of the streamline curvature appears to be the introduction of instabilities of Taylor-Görtler type in the inner half of the mixing layer, where the sense of the mean vorticity is opposite to the sense of the angular velocity.

The problem is less trivial if the densities of the two streams are the same, but the velocities are different. It is known for plane mixing layers that the structure is roughly anti-symmetrical if the density is constant; see, for example, Konrad (1976). When the velocity difference is large enough, the wake of the splitter plate becomes less important, and the principal source of instability is the shear between the two streams. The Kelvin-Helmholtz instability associated with the shear layer produces spanwise vortical structures which travel downstream.

For curved mixing layers with equal density, the flow pictures indicate the persistence of the large two-dimensional vortices, provided that the outer stream is faster. A photograph of flow J, with U_o/U_i = 1000/380, is shown in Fig. 5.1(h) (middle). A picture copied from one frame of the movie for this flow is shown in Fig. 5.2, and a picture sequence is shown in Fig. 5.3. The two-dimensional vortical structures are quite similar to the ones in the plane mixing layer; cf. Fig. 5.4, taken from Konrad (1977). The faint horizontal lines in the plan view correspond to the edges of the large structures. These lines are used in Section 7 as references for determining the spacing and celerity of the structures.

These vortical structures appear to be much less two-dimensional if the inner stream is faster. Photographs of flow $\tilde{J}$, with U_o/U_i = 380/1000, are shown in Fig. 5.1(b) (middle) and Fig. 5.5. The difference between the vortical structures here and in Fig. 5.2 is best seen in the side view. Several bridges (braids) can be seen

lying parallel to each other in the right half of Fig. 5.5. This structure is common throughout the high-speed movies taken of this flow. The implied loss of two-dimensionality might be associated with the mechanism described earlier for the curved wake. In the present case, the vorticity and the angular velocity are of opposite sense throughout the whole mixing layer, and the Taylor-Görtler instability is probably responsible for the increase of three-dimensionality. The three-dimensional boundary layers adjacent to the two side walls could also be distorted by the curvature, and could contribute to the multiple bridges seen in the side view. However, the streamwise velocity in the boundary layer is smaller than that in the free stream. Hence patterns due to side-wall boundary layers would not be expected to be always moving along with the main structure, as is the case in the movies of this flow.

A few adjacent frames from the movie for flow $\tilde{J}$ are included in Fig. 5.6. What is surprising is the profound influence of the curvature on the pairing behavior of the vortices. It is known that the vortices undergo frequent pairing in straight mixing layers. Pairing is also noticeable in Fig. 5.3, which is copied from the movie taken for flow J, in which U_0/U_i = 1000/380. For the companion flow $\tilde{J}$, with U_o/U_i = 380/1000, little if any evidence of pairing phenomena can be found. The details of the growth process cannot be seen clearly from the movies. It seems that the interaction of the large vortices is three-dimensional and is much more complicated than the usual pairing process. The vortices lose their identity gradually, by interacting with their neighbors in a three-dimensional manner, and there is a smoother overall spreading of the mixing region, as shown in the associated still picture, Fig. 5.1(b) (middle).

5.2. Flows With Different Densities

For curved mixing layers between streams having different densities, effects of centrifugal forces come from two basic causes. One is the difference in velocity. Taylor-Görtler instability can occur when the inner stream is faster than the outer stream, even in the case of mixing layers with equal densities. The other is the Rayleigh-Taylor instability, which can occur when the heavier gas is on the inside. We begin with the simplest case of equal velocities and different densities.

When the velocities are equal, we can simplify the problem by employing a moving coordinate system attached to the mean flow. This coordinate system rotates at constant angular velocity around the center of curvature of the channel, as shown in Fig. 5.7. In this moving coordinate system, the x-component of the mean flow velocity is identically zero. The equations of motion of the flow can be written, neglecting viscosity, as

$$\rho\left[\frac{D\mathbf{u}}{Dt} + 2\,\mathbf{\Omega} \times \mathbf{u} + \mathbf{\Omega} \times (\mathbf{\Omega} \times \mathbf{X})\right] = -\nabla\, p \tag{5.2.1}$$

where $\Omega = |\mathbf{\Omega}| = U/R$ is the angular velocity of the moving coordinates, and $\mathbf{X}$ is the position vector of the center of coordinates.

If we write down the x- and y-components of the momentum equation, we have

$$\rho\left[\frac{Du}{Dt} - 2\Omega v\right] = -\frac{\partial p}{\partial x} \tag{5.2.2}$$

$$\rho\left[\frac{Dv}{Dt} + 2\Omega u + \Omega^2 (R - y)\right] = -\frac{\partial p}{\partial y} \tag{5.2.3}$$

On assuming small perturbations, we have

$$\rho \frac{Du}{Dt} = -\frac{\partial p}{\partial x} \tag{5.2.4}$$

$$\rho \frac{Dv}{Dt} = -\frac{\partial p}{\partial y} - \rho\Omega^2 R \tag{5.2.5}$$

These are the equations of motion in cartesian coordinates for a flow subject to a radial body force $\Omega^2 R$. The approximation is valid if the effect of the wake of the splitter plate is small.

In the moving coordinates, the system is statically unstable if the heavy fluid is on top of the light fluid; i.e., if the density gradient is opposite to the body force. This situation is the origin of Rayleigh-Taylor instability. For curved mixing layers in which the two streams have equal velocities, therefore, we can associate the flow with an equivalent static system in a gravity field. If the heavy fluid occupies the outer part of the channel, the system is stable. A picture for this case, flow U, is shown in Fig. 5.1(e) (top). Both streams are moving at 400 cm/sec, with nitrogen on the outside and helium on the inside.

If the heavy fluid is on the inside, the companion mixing layer, $\tilde{U}$, appears as shown in Fig. 5.1(e) (bottom). Both streams are still at 400 cm/sec, but now with nitrogen on the inside and helium on the outside. It is clear that Rayleigh-Taylor instability plays a dominant role in this flow. It can be noticed from the picture that the mixing region grows smoothly, with the growth governed mostly

by structures of small scale, rather than by the large vortical structures which dominate the ordinary shear layer. Movies taken of this flow indicate that the flow is quite steady, and there are few low-frequency fluctuations.

Even though no large-scale vortical structures are observed in this particular flow, there still seem to be certain preferred structures having finer scales. These fine-scale structures can best be seen in the plan view of Fig. 5.8. They look more or less like the cells in a kind of cloud known as 'mamma' (Scorer 1978). Movies taken of this flow suggest that these structures emerge from roughly fixed locations on the splitter plate. Similar structures appear at about the same time at all such locations. Both in the streamwise direction and in the spanwise direction, these fine-scale structures appear to remain aligned with each other as they move downstream.

According to the flow-visualization results, the ultimate effect of a large density difference is a different kind of structure from either large spanwise vortices or large streamwise vortices. The basic mechanism for the fine structures is probably Rayleigh-Taylor instability. It should be noted that when a stratified shear flow is non-steady, local streamlines are in general curved and changing with time. It is possible that Rayleigh-Taylor instability can then also occur in those places where the curvature of the streamlines and the density gradient have the right combination, as proposed by Konrad (1976).

We have discussed up to now the simple case of equal density and the simple case of equal velocity. There are two ways to consider the general case of curved mixing layers having both a density difference and a velocity difference. We may either add density difference to the flow with pure shear, or add shear to the flow with pure density difference.

Since only three density ratios, 7, 1, or 1/7, were used in our experiments, there are not enough results for presenting the effects of gradually increasing density difference. We therefore follow the second strategy and consider the general case by looking at flows with greater and greater velocity difference, starting from the case of equal velocity.

If we begin with the case $\rho_o/\rho_i = 1/7$, i.e., inner stream heavier, and with $U_o/U_i = 1.0$, and gradually increase the speed of the outer stream, the sequence of flows is as shown in Fig. 5.1(e) (bottom) to Fig. 5.1(i) (bottom). The large spanwise vortices become more and more pronounced. The three-dimensional nature of these structures is best represented by Fig. 5.9. The streaks in the streamwise direction in the plan view seem to have a preferred spacing. Experiments carried out by Bernal (1981) on straight mixing layers in water have shown that these streamwise structures in cross-section look like mushrooms. Konrad (1976) argued that such streamwise vortices are caused by Taylor-Gortler instability and are similar to Taylor vortices. Aryshev, Golovin, and Ershin (1981) indicated that an instability of colliding streams can produce streamwise vortices. Such a collision occurs near the internal stagnation points of a shear layer according to Coles's model (1981) discussed in Section 7 below. In any event, the spacing of such streamwise structures has been measured for most of our flows from the movies and is a main topic in Section 7.

In the side view of Fig. 5.9 it can be seen that the bridges between the vortices are relatively thick when compared with the straight mixing layer in Fig. 5.10, taken from Konrad (1976). The thickening of the bridges is associated with enhanced three-dimensional motions. In Fig. 5.9 the ρU^2 product is the same for both streams. The flow should therefore be neutrally stable to streamwise disturbances according to the Rayleigh-Synge criterion defined by Eq. (2.5.10). The enhanced three-dimensionality cannot be explained by considering free-

stream conditions alone, however. Because the local flow is nearly irrotational in the vicinity of the bridges, the velocity distribution is essentially continuous, but the density distribution is not. Hence locally we have an unstable interface due to mean streamline curvature and density difference. The Rayleigh-Synge stability criterion is violated, because $\frac{d}{dr}(\rho u^2) = u^2 \frac{d\rho}{dr} < 0$ when the heavier gas is inside. The implied change in the characteristics of the flow can be properly accounted for only after a detailed study of the local behavior of the unsteady flow.

Suppose we increase the speed of the inner stream, so that the $\frac{U_o}{U_i}$ ratio decreases gradually from 1 to $\frac{1}{4}$, but $\frac{\rho_o}{\rho_i}$ is still $\frac{1}{7}$. The sequence of events is shown in Fig. 5.1(e) (bottom) to Fig. 5.1(a) (bottom). If we were anticipating larger and larger vortical structures in the pictures, we would be disappointed. The side views of the mixing layers show that the flow is dominated mostly by three-dimensional small-scale structures, with the two-dimensional vortical structures taking on diminishing importance.

The growth rate of these flows, measured from long-time-exposure pictures described in Section 7.1 below, is shown in Fig. 7.5. The figure suggests that, although the speed ratio has changed from 1 to roughly 1/4, the growth rate of these mixing layers has changed only slightly. The presence of small structures and the constancy of growth rate imply that the dominant role is probably played by Rayleigh-Taylor instability.

As mentioned earlier in this section, the flow $\tilde{P}$ in Fig. 5.1(b) (bottom) can be realized from the flow $\tilde{J}$ in Fig. 5.1(b) (middle) by reducing the density of the fluid in the outer stream. Since the large vortical structures in $\tilde{J}$ exhibit strong three-dimensionality, the same three-dimensionality ought to exist also

in the flow $\tilde{P}$, because there is no stabilizing mechanism to stop it. There are at least three mechanisms causing instability in this latter flow $\tilde{P}$. These are the Kelvin-Helmholtz instability, the Rayleigh-Taylor instability, and the Taylor-Görtler instability. As expected, our flow pictures show that the interface between the two streams becomes very complicated.

One difficult question is whether or not an unstable density distribution helps to drive the flow in favor of Taylor-Görtler instability in such a way that helical structures appear in each of the roll cells, which therefore resemble those existing between cylinders rotating in the same direction. Such a flow pattern cannot be *steady* and *axisymmetric* simultaneously, unless the individual fluid particles can change their properties - density, velocity, temperature, etc. - with time periodically as they move around, so that these properties are consistent with the stationary properties of the fluid on the boundary. Such behavior is possible in circular Couette flow, in which the speed of the fluid particles can be changed by viscosity. It is also possible in Bernard convection, in which the temperature can be changed by heat transfer. When the density difference is not due to change of temperature but to difference in species, no density balance can be expected, because species are convected with the fluid. In turbulent flows, molecular diffusion, like viscosity, is unimportant. The absence of a mechanism which allows each species to affect the density of the other in a mixing layer hence rules out steady axisymmetric flow as a possible solution.

Apart from this observation, there is no apparent reason why helical structures cannot exist in a mixing layer with the heavy fluid on the inside. Unfortunately, such structures have not been identified in our flow visualization pictures so far. The fact that the three instability mechanisms may all be effective at the same time has made the flow too complicated to show a clear pattern.

The picture for flow $\tilde{A}$, shown in Fig. 5.9, suggests that the streamwise disturbances are much stronger then in a plane mixing layer. However, the Rayleigh-Synge criterion is not able to explain this phenomenon satisfactorily if we consider the mean flow alone, for reasons discussed earlier.

Some experiments have also been done for curved mixing layers with the heavy gas in the outer stream. Figs. 5.1(a) (top) to 5.1(i) (top) show the sequence as the speed ratio U_o/U_i increases gradually from $\frac{1}{4}$ to 4. In all of these pictures, the interfaces between the fluids are relatively sharp, and the thickness of the bridges is quite close to that in a straight mixing layer. The plan views of these pictures (for example, Fig. 5.11) indicate weaker three-dimensionality (compared with Fig. 5.9, say).

Two-dimensional vortical or spanwise structures can be defined very well throughout this flow regime. However, the growth rate of the mixing layer appears to be greatly reduced when the outer, heavier stream is moving faster.

VI. Profiles of Mean Concentration and Mean Velocity

A general point of interest in turbulent flow studies is the property of self-similarity. For plane mixing layers, there is no preferred length scale in the flow, so that self-similarity is suggested by intuition and is usually confirmed by experiment. In a curved mixing layer, the radius of curvature is a new length scale in the flow. For mixing layers of constant density, the extra rate of strain due to curvature is proportional to $\frac{\delta}{R}$. Thus the turbulent flow will be self-preserving only if the ratio $\frac{\delta}{R}$ is kept constant. For mixing layers with a large density difference, the effects of centripetal acceleration may be more important. The gradient Richardson number, $\frac{g}{\rho}\frac{d\rho}{dy}\Big/\left(\frac{du}{dy}\right)^2$, where $g \approx \frac{u^2}{R}$, may become an important parameter, and again suggests the desirability of keeping $\frac{\delta}{R}$ constant in order to keep the mixing layer self-similar. However, both the thickness of the mixing layer and the radius of curvature are unknown prior to experiments, and in any event both quantities are difficult to define.

Since the main concern of the present research is with the effects of curvature on coherent structures in mixing layers, no attempt was made to achieve a constant ratio of $\frac{\delta}{R}$. The question of whether or not self-similarity exists in our curved mixing layers therefore cannot be resolved from the profile measurements about to be described. Nevertheless, our measurements allow the thickness and the virtual origin for each mixing layer to be determined and used as a reference for other variables as well as for future experiments on curved mixing layers.

Profile measurements have been made for six flow cases, denoted in Fig. 4.1 and Table 1 by the symbols B , A , $\tilde{A}$, P , $\tilde{P}$, and $\tilde{U}$. All have density ratios different from 1; i.e., either 7 or 1/7. For each flow, traverses were made at four downstream angular positions located 10, 15, 20 and 25 degrees from the trailing edge of the splitter plate. The mixing layer in the flow $\tilde{P}$ grew so fast that it touched the curved walls somewhere between 20 and 25 degrees downstream, and no profile measurements were made for the last downstream location in that flow. Each traverse consisted of measurements at 15 radial stations. The first and last stations were always located well outside of the mixing layer. At each station, 4096 samples were collected at 33.3 kHz for each of the two probes, the concentration probe and the pitot-static probe. The elapsed time of the measurements for each station was 0.12 seconds. For the typical flow covered in our measurements, this elapsed time corresponds to the passage of roughly twenty vortices over the probes.

Mean concentration data were obtained by averaging the 4096 concentration values inferred from the voltage signals, using the calibration polynomial for the concentration probe. The mean concentration was used to determine the mean density according to the experimental conditions. The mean velocity was finally calculated from the mean density and the mean dynamic pressure, the latter obtained by averaging the 4096 pitot-static-probe measurements. Some features of these mean profiles will be discussed in this chapter.

Despite the fact that $\frac{\delta}{R}$ varies in our experiment, mean concentration profiles at different down-stream locations for a given flow are usually quite similar to each other. In order to establish the thickness of the mixing layer, points of 10-percent and 90-percent concentration of helium were used to determine the mixing boundaries. Since the measurements were made at discrete radial locations, the actual mixing boundaries had to be determined by

interpolation. A cubic-spline interpolation routine was used for that purpose. The two boundaries determined in this way for each mixing layer were then fitted by a straight line, using a least-mean-square method, and finally the virtual origin of each mixing layer was determined.

After collapsing profiles for the same flow onto a single picture, with the independent variable r or y normalized by the local thickness of the mixing layer as determined from the fitted boundaries, it was found that a straight-line fit through the boundaries was usually satisfactory. For a typical example, see Fig. 6.1. The same remark applies to the majority of the flow cases studied. Hence straight lines were adopted for the mixing-layer boundaries determined from the profiles of mean concentration.

The same approach was followed in dealing with the mean-velocity profiles. However, it was first found that the velocity did not approach a constant in either free stream of the mixing layers, especially if the velocities were higher toward the center of curvature. Inasmuch as the flow outside of the mixing layer is irrotational, we expect the velocity to vary like $1/r$ if the irrotational flow in the curved channel is well developed. On the other hand, the flow right at the exit of the nozzles is supposed to be uniform except for possible deviations due to the influence of the curved channel downstream. Therefore, there is a transitional region near the channel entrance in which the irrotational flow changes from a uniform inlet flow into a vortex-like flow. Since the measurements are all for locations more than one channel height downstream of the channel entrance, there is some hope that they are out of the transitional region. Profiles of ur were therefore plotted, and there was substantial improvement. Hence ur profiles, rather than velocity profiles, are used in the rest of our study.

The growth of the mixing boundary as determined from the ur profiles was also determined by a straight-line fit; see, for example, Fig. 6.2. The virtual origins determined from the concentration and ur profiles are different, although the difference is small for most of our flows. For such flow cases, the average of the two virtual origins was taken, and revised mixing boundaries were calculated by forcing the fitted straight lines to pass through the average origin for the concentration and the ur data. The final profiles of mean concentration and ur product are plotted in Figs. 6.3 to 6.6 for various flow cases as functions of $\frac{y-y_v}{x-x_v}$, where x_v and y_v are the tangential and normal coordinates of the virtual origin, respectively. It appears that the profiles for a given flow coincide quite acceptably, and a common profile can be drawn to represent the mean distribution for both concentration and ur-product.

Two flow cases do not lend themselves to this treatment. The first flow giving trouble is $\tilde{P}$. This is a case in which the mixing layer grew so rapidly that it touched the curved walls about 11 cm downstream of the splitter plate. It also happens that the velocity profiles for this flow have significant overshoot above the velocity of the highspeed stream, and the scheme discussed above for collapsing velocity profiles does not work. The result, shown in Fig. 6.7b, was a virtual origin located downstream of the splitter plate. This virtual origin is also significantly different from the virtual origin determined by using concentration profiles, as shown in Fig. 6.7a. The other flow giving trouble is $\tilde{U}$, for which the concentration profile is shown in Fig. 6.8. Again the problem originates in the profile of ur. Since the free-stream velocities in this case are roughly equal, a different scheme was needed for determining the mixing-layer boundaries using the profiles of ur. Two runs at different Reynolds number were available for this flow. The ur profiles from the run at lower Reynolds number show significant wake behavior in the mixing layer. However, the defect velocities

cannot be determined with accuracy because the number of data points is too small. The other run, at higher Reynolds number, gave ur profiles having double peaks along with the wake deficit. These results cast some doubt on the accuracy of the pitot-static measurement as a reference for velocity. Two questions arise. First, the pitot-static probe may have picked up a contribution to dynamic pressure from velocity components not parallel to the probe. Second, cross-correlations such as $\overline{\rho u'^2}$, $\overline{\rho' u'^2}$ and $\bar{u}\ \overline{\rho' u'}$, which were neglected in calculating mean velocity from average data for dynamic pressure and density, may be important. However, it is then not clear why there is less difficulty with the remaining flows.

VII. Length Scales and Celerity

Our flow visualization results, reported in the previous section, indicate that the dominant structures in curved turbulent mixing layers are spanwise and streamwise secondary structures, just as in plane mixing layers. The present section will discuss some observed differences in the structure of different flow cases when the sense of the curvature is changed.

Two quantities of interest for the large vortical structures can be derived from the high-speed movies. These are the spacing between adjacent structures and the speed of movement, or celerity, of the structures. The vortical structures are not symmetrical in shape. The leading edges are relatively diffuse, and it is very difficult to establish their location. However, the trailing edges are normally quite sharp and can be located with good accuracy. The trailing edges of the large vortices were therefore used for locating each structure. Additional guidance is provided by the plan view of the flow, in which the trailing edges of the vortices appear as faint horizontal lines, as seen, for example, in Fig. 5.9. These lines are the major references used in determining the trajectories of the trailing edges. All of the measurements discussed in this chapter were carried out manually, by projecting the high-speed movies on a screen and scrutinizing the pictures frame by frame. For each flow, one thousand continuous frames were sampled. The elapsed time is 0.5 seconds in the real flow, since the movies were taken at two thousand frames per second. For calculating the speed of the trailing edges, timing marks on the edges of the movie film were used as a time base. Several small black rectangles were attached to the flat mirrors during the flow-visualization experiments. The images of these marks helped to

determine the scale between the pictures and the real flow.

7.1. Length Scales of Spanwise Structures

The locations of all trailing edges of all large vortices in a frame were recorded on graph paper, as shown in Fig. 7.1, with horizontal axis representing downstream distance x and vertical axis representing frame number. To calculate the spacing of these large structures at a given downstream location, the distances between all pairs of adjacent trailing edges which passed over that location were averaged. The variation of the spacing S along the x direction is shown in Fig. 7.2 for various flow cases. Although one thousand frames were sampled, the average number of useful samples for each spacing calculation is only about two hundred. Given the fact that a particular vortex can be observed for several, say ten, frames of the movie, only about twenty individual vortices are considered in the calculations. The resulting curve of the average distribution of the spacing between vortices therefore shows considerable scatter. Standard deviations as large as 30 percent are common. Much of this scatter is caused by the pairing phenomenon between vortices. A given vortex does not grow smoothly; instead, the spacing roughly doubles at every pairing process.

Another dimension of interest for the spanwise structures is the thickness of the structures. This quantity can be inferred from the thickness of the mixing layer as measured on photographs obtained with a long time exposure, using schlieren techniques. Fig. 7.3 shows an example of such a picture, exposed for one second for the flow P. The picture was taken with a Hasselblad 500 EL/M camera equipped with a 1:5.6 lens (f = 250 mm) together with a negative meniscus lens (1.75 diopter, f = - 571.4 mm) for focus correction. The little white rainy spots visible in the plan view of the flow are due to tiny gas bubbles in a defective lens located next to the light source of the imaging system, and are not related to the flow itself. The side view of the mixing layer has good contrast

and was used in determining the visual growth rate.

The boundaries of the mixing layer were first marked with many little dots, as exemplified by Fig. 7.3. Care was taken so that these dots were clearly distinguishable, yet tended to merge into the dark background of the mixing layer. These dots were fitted with the aid of a French curve. The thickness of the mixing layer was then measured radially at several downstream locations for which the downstream distance was determined along the centerline of the curved channel. A sheet of transparent plastic engraved with the geometry of the curved channel and the center-line, together with several radii going through their common center of curvature, was employed as a template and was found to be very helpful for measuring the mixing-layer thickness. Depending on the flow, however, the mixing-layer boundary sometimes is not sharp; for example, see Fig. 7.4, which depicts flow $\tilde{D}$. Hence the visual thickness measurements obtained this way can serve only a qualitative purpose. The distribution of the thickness of the mixing layers in the streamwise direction is shown in Fig. 7.5 for several cases. It is clear from this figure that the growth rates for the flow cases $\tilde{P}$, $\tilde{A}$, $\tilde{D}$, and $\tilde{U}$, all with unstable stratification, are not very different, even though they have drastically different velocity ratios. On the other hand, for the flows with stable stratification, the velocity ratio has a large effect on the growth rate. In an attempt to separate these influences, a small separate study was made to determine how the spreading rate depends on curvature and density difference for the case of equal velocities.

If we look at the problem of growth in laboratory coordinates, we note that the growth rate $h = \frac{d\delta}{dx}$ is dimensionless. The velocity ratio $\frac{U_o}{U_i}$, being equal to unity, does not enter the problem. The density ratio $\frac{\rho_o}{\rho_i}$ is an independent parameter. The growth rate can thus be written

$$\frac{d\delta}{dx} = fn\ (b/R, \rho_o/\rho_i) \tag{7.1.1}$$

Suppose that the outermost boundary of the layer marks the location of fluid elements which have penetrated the other stream with the fastest speed. Let the fastest cross-stream velocity be v^*, so that v^*/U is the tangent of the angle between the trajectory of the fastest penetrating particle and the direction of the mean flow. This angle must be proportional to the spreading angle of the mixing layer. Hence we have

$$\frac{d\delta}{dx} \sim v^*/U = fn\left(\frac{b}{R}; \frac{\rho_o}{\rho_i}\right) \tag{7.1.2}$$

Consider now the same problem in moving coordinates, as indicated in Fig. 5.7 . The important physical quantities are v^*, G , and b , where G is the equivalent reduced gravitational acceleration,

$$G = \left(\frac{\rho_i - \rho_o}{\rho_i + \rho_o}\right) \frac{U^2}{R} \tag{7.1.3}$$

For this new problem, the only new dimensionless group is the Froude number v^{*2}/Gb, which must be a physical constant; i.e.,

$$v^{*2}/\left(\frac{\rho_i - \rho_o}{\rho_i + \rho_o}\right) \frac{U^2}{R} b = constant \tag{7.1.4}$$

From this relation it follows that the growth rate should be inversely proportional to the square root of the radius of curvature,

$$\frac{d\delta}{dx} \sim \frac{v^*}{U} = K \sqrt{\left[\frac{\rho_i - \rho_o}{\rho_i + \rho_o}\right]} \frac{b}{R} \qquad (7.1.5)$$

To obtain the proportionality constant, K, a few experiments were carried out using channels with different radii of curvature. The spreading rate measured from long-time-exposure pictures is shown in Fig. 7.6. The proportionality constant K is plotted against $\sqrt{\left[\frac{\rho_i - \rho_o}{\rho_i + \rho_o}\right]} \frac{b}{R}$ in Fig. 7.7. The value of K approaches asymptotically a constant value of 0.85 as the curvature increases, showing that Eq. (7.1.5) is valid when $\sqrt{\left[\frac{\rho_i - \rho_o}{\rho_i + \rho_o}\right]} \frac{b}{R}$ is large. The observed departure as the curvature decreases may be explained as a consequence of the wake left by the splitter plate. When there is no curvature, the turbulent wake should grow like the square root of the downstream distance. This effect should persist to some degree when the curvature is small. The relative importance of the body force increases with down-stream distance, while the importance of the wake decreases. The role of the body force becomes dominant after a certain distance x, depending on the radius of curvature. As shown in Fig. 7.6, a linear region in the growth boundaries is more evident when the ratio $\frac{b}{R}$ is larger. The value of K reported in Fig. 7.7 is derived from the linear portions of the curves in Fig. 7.6.

The ratio of the thickness of the mixing layer to the spacing of the spanwise structures is representative of the geometry of the structures. In Fig. 7.6 this ratio has been plotted against the variable $\frac{\sqrt{\frac{\rho_1}{\rho_2}}\frac{u_2}{u_1} + 1}{\sqrt{\frac{\rho_1}{\rho_2}} + \frac{u_2}{u_1}}$, which is the same variable used in the next paragraphs in the analysis of celerity data. It is

evident in Fig. 7.8 that, except for the flows $\tilde{A}$ and $\tilde{D}$, which have unstable stratification, all the rest of the data fall close to a flat straight line, indicating that the geometrical shape is essentially constant. However, the cases $\tilde{A}$ and $\tilde{D}$ have much thicker, or fatter, vortices than the rest of the flows. For these flow conditions, in which there is unstable stratification, it seems that changing the velocity ratio has a strong effect on the shape of the spanwise structures.

7.2. Celerity

The same set of motion-picture records was used to determine the celerity of the trailing edges of the large vortices. Average values for the slopes of the trajectories of all vortices which are visible in more than ten adjacent frames gave the celerity values listed in the last column of Table 1. In this table the experiments were all carried out at 4 atmospheres, with the flow-speed settings indicated in the second or the third column. The fourth and fifth columns of the table show, respectively, the velocity ratio and the density ratio for each run. Capital letters in the first column identify the various runs for easy reference. For some of the runs, no value of celerity is given. The reason is either that the spanwise vortices in these flows are too close together, especially when the velocity ratio is close to unity, or that the two-dimensional spanwise vortices are overshadowed by strong three-dimensional structures of finer scales, and it is almost impossible to determine the location of the large vortices.

The standard deviations listed with the celerities are in the range from 5.5 percent to 13.5 percent. Part of this scatter is due to error in the measurements. However, most of the scatter reflects the natural variation of the speed of the trailing edges of the structures. This variation is especially large when neighboring vortices are involved in the pairing process, as shown in Fig. 7.1. The largest scatter for the celerity data is found in the first and last entries in the table. These two flows have the largest velocity ratio, and the mixing layers

spread faster than for the remaining flows. Thus these two mixing layers may have been subjected to stronger wall effects than the others. Apart from these two cases, the standard deviation in the celerity measurements is less than 10 percent.

Celerity measurements have been reported in the past only for a few flow cases in straight mixing layers. The convective velocity given by Brown and Roshko (1974) for a straight mixing layer having velocity ratio 0.38 and density ratio 7 is $c/U_1 = 0.53$ (cf. the entries for flows A and $\tilde{A}$ in Table 1). As pointed out by Brown and Roshko, this value is significantly lower than the average velocity of the two streams.

A simple argument can be found to estimate the celerities of the large spanwise vortices in the present flows. This argument is based on Coles's conjecture (1981) for the mean particle paths near a vortical structure in the mixing layer, as shown in Fig. 7.9. In this figure, S is a saddle point; i.e., an internal stagnation point in the flow. The picture represents the streamline pattern that would be seen by an observer travelling at the celerity, which is the speed of the critical points in laboratory coordinates. One stream of the mixing layer is moving to the right at a velocity $(U_1 - c)$, and the other stream is moving to the left at $(c - U_2)$. The densities are ρ_1 and ρ_2, respectively, for the two streams.

Given that the flow pattern is steady in celerity coordinates, Bernoulli's theorem should apply along the converging separatrix. Thus

$$\frac{1}{2}\rho_1 (U_1 - c)^2 + p_1 = p_{01} \qquad (7.2.1)$$

$$\frac{1}{2}\rho_2 (c - U_2)^2 + p_2 = p_{02} \tag{7.2.2}$$

where p_{01} and p_{02} are the stagnation pressures on the two sides of the interface at S. Under equilibrium conditions,

$$p_{01} = p_{02}. \tag{7.2.3}$$

Within the boundary-layer approximation, there is no difference between the static pressures p_1 and p_2 in either coordinate system. Finally, therefore,

$$\frac{1}{2}\rho_1 (U_1 - c)^2 = \frac{1}{2}\rho_2 (c - U_2)^2 \tag{7.2.4}$$

This result has also been argued independently by Dimotakis (1984). An obvious choice of sign $(U_1 > c > U_2)$ gives

$$\frac{U_1 - c}{c - U_2} = \sqrt{\frac{\rho_2}{\rho_1}} \tag{7.2.5}$$

The solution for c in its most symmetrical form is

$$c = \frac{\sqrt{\rho_1} U_1 + \sqrt{\rho_2} U_2}{\sqrt{\rho_1} + \sqrt{\rho_2}} \tag{7.2.6}$$

This estimate of celerity is based on the model proposed by Coles for straight mixing layers. When the mixing layers are curved, we expect the expression to be still valid provided that the curvature is mild.

To compare our experimental results with Coles's model, we note that Eq. (7.2.6) implies

$$\frac{2c}{u_o + u_i} = \frac{2}{1 + Z}, \tag{7.2.7}$$

where u_o and u_i are the estimated free-stream velocities in the curved mixing layer and

$$Z = \frac{\sqrt{\frac{\rho_o}{\rho_i}}\,\frac{u_i}{u_o} + 1}{\sqrt{\frac{\rho_o}{\rho_i}} + \frac{u_i}{u_o}}. \tag{7.2.8}$$

Experimental values of celerity are plotted in Fig. 7.10, with Z as abscissa and $2c/(u_o + u_i)$ as ordinate. Closed symbols correspond to data for flows which are unstable according to the Rayleigh-Synge criterion expressed by Eq. (2.5.10). Both kinds of symbols appear to lie below the the theoretical curve, perhaps because the presumably slightly higher celerities of the leading edges are not taken into account. This result shows that some effect of streamline curvature on the celerity of the large two-dimensional vortices may exist. Nevertheless, the overall agreement between the experimental data and the theory based on Coles's model is quite good.

7.3. Length Scales of Streamwise Structures

The length scale in the spanwise direction is also of interest. The streamwise streaks in the plan view of our flow pictures presumably correspond to the edges of ridges of fluid whose crossections look like mushrooms, as shown schematically in Fig. 7.11. One such ridge introduces a group of bright or dark streaks into the plan view of our pictures. For regions close to the trailing edge of the

splitter plate, these patterns are directly associated with the flow structure in the streamwise direction. In these regions the length scale, i.e., the spacing of the streamwise structures, can therefore be determined by measuring the spacing between groups of streaks.

Farther downstream, the information carried by the streamwise patterns is twofold. On the one hand, the patterns are directly traceable to structures formed upstream and convected with the fluid. On the other hand, new structures may appear, or old structures coalesce, as the flow travels downstream. The new structures introduce new length scales and may modify the patterns created earlier. A typical series of pictures showing the evolution of the streamwise structures is shown in Figure 7.12. The streamwise streaks which emerge from the top of the pictures are more or less equally spaced. The same number of streaks can be followed for a long distance downstream as they are convected with the flow. The spacing between these streaks, however, is no longer uniform as it was before. The change in the spacing is more or less periodic in the spanwise direction. This suggests the existence of a new structure in the streamwise direction. The spacing of this new structure is equal to the period of the changes and is different from the spacing between the streaks.

In our measurement for the spacing of the streamwise structures, the longest average period of repeatable patterns of streaks was determined for six downstream locations, frame by frame, using the same section of high-speed movies employed in our former measurements. The streaks are highly visible in the bridges, which were centered on specified downstream stations in the frames in which the spacing was measured. The percentage of the movie frames which show distinct length scales, as exemplified by Fig. 7.12, is, on the average, small. Depending on the flow and on the downstream location where the measurements were made, this number ranges from 1 to 40 percent with mean value at roughly

5 percent. The rest of the movie frames either do not show the patterns at the places where measurements were made, or suggest different length scales in repeated measurements, or show different spacing at different spanwise locations. For example, in the upper part of the first picture in Fig. 7.12, four pairs of streamwise streaks are clearly visible. They are more or less equally spaced, and hence are considered to comprise a good sample for the measurement made at that downstream location. The span from the first pair to the last pair of streaks was divided by three to give the average spacing for this sample picture at the appropriate downstream location. The same was done for the upper and middle part of the second picture and the middle and lower part of the third picture. On the contrary, no distinct length scales are visible in the middle and lower part of the first picture. Hence no measurements were taken from these portions of the first picture during the measurements made for these downstream locations.

Some streamwise patterns seem to appear in the upper part of the third picture and the lower part of the second picture. However, it is hard to establish how many pairs of structures exist. To avoid subjective judgements as much as possible, all such samples which might lead to ambiguous length scales were dropped. Results from the rest of the pictures were then averaged to give the data shown in Figs. 7.13(a) to 7.13(j). For convenience, data for each pair of flows with the same velocity ratio and density ratio are displayed in the same figure. The only difference between the two flows in each figure is the sense of curvature of the mixing layer. Open symbols correspond to data for flows which are stable, while closed symbols are for flows which are unstable according to the Rayleigh-Synge criterion. The abscissa in these figures represents downstream distance normalized with respect to channel height. The ordinate is the average spacing of the streamwise structures.

Due probably to the limited number of samples available, especially for measurements at locations far downstream, some of these figures do not show a monotonic trend of increasing length scales with increasing x; see, for example, Figs. 7.13(d), 7.13(e), and 7.13(f). In general, however, an increase of spacing with increasing downstream distance is quite apparent. Throughout these figures, the closed symbols (unstable flow) almost unanimously lie above the open symbols (stable flow). The rate of increase of spacing is faster for the runs represented by the closed symbols. Hence the effect of curvature appears to be strong in changing the spacing of the streamwise three dimensional structures. Adverse curvature tends to create large-scale three-dimensional structure in the streamwise direction.

In principle, using the results of length-scale measurements for the streamwise structures, virtual origins can be determined. Whether or not these virtual origins coincide with the virtual origins determined from the growth of the two-dimensional spanwise structures is a pertinent question. Unfortunately, the limited number of available length-scale measurements, at only six downstream locations, and the significant scatter of sampled data, prohibit us from fitting straight lines to the length-scale distribution with meaningful accuracy. However, the results of the transverse length-scale measurements, as shown in Figs. 7.13(a) to 7.13(j), suggest that almost all the virtual origins determined accordingly would be located upstream of the trailing edge of the splitter plate.

Virtual origins based on profile measurements have been obtained for flows A, $\tilde{A}$, P, $\tilde{P}$ and B, as discussed in Section 5 above. Apart from flow $\tilde{P}$, the virtual origins determined from concentration profiles and from velocity profiles are quite close together. Hence averaged virtual origins for these five flows have been marked in Figs. 7.13(a) to 7.13(c). For purposes of comparison, straight lines passing through these virtual origins were drawn to fit the length-scale

data for each experiment. Taking into consideration the significant uncertainty involved in the length-scale measurements, especially around the trailing edge of the splitter plate, where the flow is not yet self-similar, or around the end of the test section, where the number of available samples is very small, the correlation shown in Figs. 7.13(a) to 7.13(c) appears to be reasonably consistent. This finding suggests that the scale of the streamwise structures shares the virtual origin obtained from the profile measurements.

VIII. Discussion

For curved mixing layers with uniform density, the sense of the channel curvature has a large effect on the coherent structure of the layer, as pointed out in Section 5.1. The effect can evidently be attributed exclusively to Taylor-Görtler instability. The effect on the structure of the flow is two-fold. First, three-dimensionality is enhanced if the faster stream is on the inside. Multiple bridges (braids) can be seen in the side views; see, for example, Fig. 5.5. Second, movie sequences like that represented by Fig. 5.6 show that the pairing phenomenon, which is common in the plane mixing layer, is much less common in the curved flow. These observations suggest that growth of such mixing layers is accompanied by three-dimensional interactions among the primary structures.

For mixing layers with different densities, discussed in Section 5.2, three-dimensionality is greatly inhibited if the heavier fluid is on the outside. The growth rate is also reduced, compared with the corresponding plane flow, if the outer stream is faster than the inner stream. On the other hand, if the heavier fluid is on the inside, three-dimensionality is greatly enhanced by effects of Rayleigh-Taylor instability (as a result of the body force) or Taylor-Görtler instability (if the inner stream is also faster) or both. The Rayleigh-Taylor instability often appears to dominate. Many of the flow-visualization pictures show a flow covered by fine-scale structures; see, for example, Fig. 5.1(b) (bottom). Large-scale spanwise structures may still be visible when the velocities of the two streams are sufficiently different.

The concept of coherent structure in turbulence leads in Section 7 to a useful application of the Lagrangian point of view. Coles's model (1981) for the spanwise structures in mixing layers, described in Section 7.2, immediately yields an estimate for the celerity of the spanwise structures. Comparison of this theoretical result with celerity data measured from high-speed movies, as shown in Fig. 7.10, shows excellent agreement over the whole range of velocity ratios and density ratios covered by the experiments. According to these measurements, the sense of curvature does not seem to have much effect on the celerity of the coherent spanwise structures. Coles's model stipulates that there are colliding streams near the saddle points, or internal stagnation points, of a mixing layer. According to Aryshev, Golovin and Ershin (1981), the local streamline curvature associated with such colliding streams can lead to Taylor-Görtler instability. Thus the colliding streams may very well be responsible for the initial formation of streamwise vortices. The additional curvature introduced by the curved channel used in our experiments is mild compared with the local curvature of the colliding streamlines. However, for the constant-density case, discussed in Section 5.1, our experiments show that the sense of the mean streamline curvature strongly affects the three-dimensionality of the mixing layer, and also that the regular pairing process is inhibited when the inner stream is faster than the outer stream.

The growth-rate measurements reported in Section 7.1 show that the flows $\tilde{P}$, $\tilde{A}$, $\tilde{D}$ and $\tilde{U}$, all with the heavier fluid on the inside, grow at about the same rate, although they have drastically different velocity ratios. This result may be peculiar to our experiments, which are constrained to use a very large density ratio; namely, $\rho_o/\rho_i = 1/7$. On the other hand, according to Brown and Roshko (1974) and Dimotakis (1984), the effect of density difference on the growth rate of a plane mixing layer is small, whereas the effect of velocity difference can be large.

The Lagrangian argument in Section 7.1 led to a relation (7.1.5) for the dependence of growth rate on mean radius of curvature for the case of a curved wake with the inner stream heavier. This relation suggests that the height of the channel, b, is an important length scale if the channel is curved. The quantity on the right-hand side of Eq. (7.1.5); i.e.,

$$\sqrt{\frac{\rho_i - \rho_o}{\rho_i + \rho_o}\,\frac{b}{R}}$$

approaches zero as $R \to \infty$, whatever the value of b, as long as b remains much smaller than R. Hence the effect of finite channel height b should not be observable for a plane mixing layer.

This conclusion applies for curved mixing layers with significant density difference. Nevertheless, it brings up two questions. First, the ratio of the height of the two streams in a curved mixing layer may be an important parameter which should be considered in future experiments. Second, the height of the channel may be important for the structure of curved turbulent mixing layers even if the density is uniform, and may have to be considered when experimental results from different facilities are compared with each other.

For mixing layers with different densities, Taylor-Görtler instability should occur if the Rayleigh-Synge stability criterion, $\frac{d}{dr}(\rho u^2 r^2) > 0$, is violated. However, Rayleigh-Taylor instability may also be expected to result from a density difference alone, if the heavy fluid is on the inside. Experimental results for mixing layers with different densities, presented in Section 5.2 above, indicate that the substantial density difference in our experiments produces overwhelmingly strong three-dimensional small-scale structure (resembling that in our curved wake, Fig. 5.1(e) (middle)), when the heavier fluid is on the inside, and

especially when the inner stream is also faster. This property prevented us from observing organized streamwise structures in this flow regime. Nevertheless, the length-scale measurements presented in Section 7.3 suggest that the characteristic length scales in the spanwise direction depend strongly on whether or not a flow is stable according to the Rayleigh-Synge criterion. As shown in Figs. 7.13(a)-7.13(i), streamwise structures of large scale appear in most of the instable cases.

The algebraic formulation in Section 2 leads to two observations. First, for Kelvin-Helmholtz instability, the analysis confirms that the inflection point within a shear-layer velocity profile is responsible for the two-dimensional instability which creates spanwise vortical structures. The minimum critical Reynolds number is so low that Kelvin-Helmholtz instability normally occurs almost immediately in all of our mixing layers. This conclusion is justified by the fact that large spanwise structures appear close to the splitter plate in all of our flows, except the curved wake, despite the wide range of Reynolds numbers, $1.0 \times 10^3 - 7 \times 10^4$, covered by our experiments.

The occurrence of Taylor-Görtler instability is described by Eq. (2.5.14), which provides a means for testing for the production of large streamwise vortices, or, equivalently, the destruction of large spanwise vortices originally arising from Kelvin-Helmholtz instability. Equation (2.5.14) includes the effect of viscosity, and therefore provides an estimate for the critical thickness of the mixing layer where marginal instability first occurs. Thus the equation guides us in looking for a difference in the large structure downstream of a particular location. No such critical thickness is provided by the Rayleigh-Synge criterion, Eq.(2.5.10), which deals only with inviscid flow.

Eq. (2.5.14) refers to laminar flow. However, Lessen and Singh (1974) suggest that turbulent shear flows can be visualized as marginally stable in terms of the

usual kind of stability analysis, provided that the viscosity $\nu = \mu / \rho$ is replaced by a turbulent viscosity ν_T. They further suggest that the Reynolds number R_T formed from the velocity difference, the layer thickness based on maximum slope, and ν_T, has nearly a universal value. They propose a universal value of the order of 150 for the case of a turbulent jet or wake (the thickness used by Lessen and Singh is smaller than our thickness by a factor of four).

Our experiments indicate that the maximum-slope thickness is about half the visual thickness of our mixing layers. Thus we can put

$$\nu_T = \frac{1}{R_T} \mid U_o - U_i \mid \frac{\delta_{vis}}{2} \tag{8.0.1}$$

We can further estimate the various quantities in Eq. (2.5.14) as follows;

$$\bar{\omega} = \frac{\bar{v}}{R} = \frac{U_o + U_i}{2R} \tag{8.0.2}$$

$$\bar{\zeta} = \frac{d\bar{v}}{dr} = \frac{U_o - U_i}{L} \tag{8.0.3}$$

$$\bar{\rho} = \frac{\rho_o + \rho_i}{2} \tag{8.0.4}$$

$$\frac{d\bar{\rho}}{dr} = \frac{\rho_o - \rho_i}{L} \tag{8.0.5}$$

Equation (2.5.14) thus suggests Taylor-Görtler instability if

$$\frac{(U_o + U_i)^2}{(U_o - U_i)^2}\left[\frac{(U_i - U_o)}{(U_i + U_o)} + \frac{1}{2}\frac{(\rho_i - \rho_o)}{(\rho_i + \rho_o)}\right]$$

$$\geq 0.189\ \frac{27\pi^4}{4}\ \frac{1}{R_T{}^2}\ \frac{2R}{\delta_{vis}} \qquad (8.0.6)$$

where L/δ has been replaced by the numerical value 0.189 from Eq. (2.4.23). Equation (8.0.6) can be recognized as an example of the kind of functional relationship originally proposed in Equation (1.0.1) of Section 1 above. This equation shows how a given shear flow may become unstable downstream of a given station, because the left-hand side is constant but the right-hand side decreases with increasing x (increasing δ).

Use of Eq. (8.0.6) requires a knowledge of $\delta_{vis}(x)$, say from long-time-exposure photographs. Typical data for δ_{vis} as a function of x have already been reported in Fig. 7.5. With this information, the x-station for the onset of Taylor-Görtler instability has been determined and marked by small triangles in several of the photographs in Fig. 5.1. In some of the pictures, no marks appear. The flows in question are either completely stable or are unstable only at a downstream distance so large that it is outside of the range of our experiments.

Most of the unstable flows are represented by the the bottom pictures in Figs. 5.1 (a) to 5.1 (i), with $\rho_o/\rho_i = 1/7$. Hence a heavier inner stream is usually associated with the instability. The main evidence for the appearance of Taylor-Görtler instability comes from the observed loss of two-dimensionality for the large spanwise vortices. Upstream of all of the triangular marks in Fig. 5.1, the images of the spanwise vortices are relatively sharp, indicating that two-dimensionality is maintained. The two-dimensionality is consistently lost, however, somewhere downstream of the triangular marks. See, for example, the

photographs of flow $\tilde{D}$, flow B, and flow $\tilde{S}$ in Figs. 5.1 (g), 5.1 (a), and 5.1 (c), respectively, all of which are consistent with destruction of the spanwise vortices by Taylor-Görtler instability. The photographs of the flows which are stable (no triangular marks) typically show persistence of large spanwise vortices far downstream.

These observations are necessarily qualitative. To locate the occurrence of instability, using Eq. (8.0.6), we have invoked the concept of turbulent viscosity, which is generally unsatisfactory for describing turbulent flows, and we have employed the visual thickness, which is itself a qualitative measure. Nevertheless, there is a consistent overall tendency for the large spanwise structures to lose their two-dimensionality earlier in the unstable cases than in the stable cases.

References

Aryshev, Yu.A., Golovin, V.A., and Ershin, Sh.A. 1981 *Stability of colliding flows*, Fluid Dynamics **16**, 755-759. Translated from "Izvestiya Akademii Nauk SSSR, Mekh. Zhidk. i Gaza", No. 5, Sept.- Oct., 143-147.

Baker, R.L., Rozenman, T., and Weinstein, H. 1968 *Stability of shear flow with density gradient and viscosity*, NASA CR-958.

Batchelor, G.K. 1967 " An Introduction to Fluid Dynamics", Cambridge Univ. Press.

Bellman, R. and Pennington, R.H. 1954 *Effects of surface tension and viscosity on Taylor instability*, Quart. J. App. Math. **12**, 151-162.

Bénard, H. 1900 *Les tourbillons cellulaires dans une nappe liquide*, Revue Gén. Sci. Pur. Appl. **11**, 1261-1271.

Bernal, L.P. 1981 *The coherent structure of turbulent mixing layers*, Ph.D. Thesis, California Institute of Technology.

Betchov, R. and Szewczyk, A. 1963 *Stability of a shear layer between parallel streams*, Phys. Fluids **6**, 1391-1396.

Bogdanoff, D.W. 1983 *Compressibility effects in turbulent shear layers*, AIAA J. **21**, 926-927.

Bradshaw, P. 1973 *Effects of streamline curvature on turbulent flow*, AGARDograph No.169.

Breidenthal, R.E. 1978 *A chemically reacting turbulent shear layer*, Ph.D. Thesis, California Institute of Technology.

Brown, G.L. 1974 *The entrainment and large structure in turbulent mixing layers*, in: Proc. Fifth Australasian Conference on Hydraulics and Fluid Mechanics, Christchurch, 352-359.

Brown, G.L. and Rebollo, M.R. 1972 *A small, fast-response probe to measure composition of a binary gas mixture*, AIAA J. **10**, 649-652.

Brown, G.L. and Roshko, A. 1971 *The effect of density difference on the turbulent mixing layer*, in: "Turbulent Shear Flows", AGARD-CP-93, Paper 23.

Brown, G.L. and Roshko, A. 1974 *On density effects and large structure in turbulent mixing layers*, J. Fluid Mech. **64**, 775-816.

Chandrasekhar, S. 1961 "Hydrodynamic and Hydromagnetic Stability", Oxford Univ. Press.

Cole, R.L. and Tankin, R.S. 1973 *Experimental study of Taylor instability*, Phys. Fluids **16**, 1810-1815.

Coles, D. 1965 *Transition in circular Couette flow*, J. Fluid Mech. **21**, 385-425.

Coles, D. 1967 *A note on Taylor instability in circular Couette flow*, J. Appl. Mech. Trans. ASME **E 34**, 529-534.

Coles, D. 1981 *Prospects for useful research on coherent structure in turbulent shear flow*, Proc. Indian Acad. of Sciences **4**, 111-127.

Curle, N. 1956 *Hydrodynamic instability of the laminar mixing region between parallel streams*, ARC Rep. F.M. 2400.

Davey, R.F. 1971 *An experimental investigation of the effect of a density gradient on shear layer instability*, Ph.D. Thesis, California Institute of Technology.

Davey, R.F. and Roshko, A. 1972 *The effect of a density difference on shear-layer instability*, J. Fluid Mech. **53**, 523-543.

Dimotakis, P.E. 1984 *Entrainment into a fully developed, two-dimensional shear layer*, AIAA Paper 84-0368.

Drazin, P.G. and Reid, W.H. 1981 "Hydrodynamic Stability", Cambridge Univ. Press.

Emmons, H.W., Chang, C.T., and Watson, B.C. 1960 *Taylor instability of finite surface waves*, J. Fluid Mech. **7**, 177-193.

Fjørtoft, R. 1950 *Application of integral theorems in deriving criteria of stability for laminar flows and for the baroclinic circular vortex*, Geofys. Publ., Oslo **17**, No. 6, 1-52.

Gibson, M.M. and Younis, B.A. 1983 *Turbulence measurements in a developing mixing layer with mild destabilizing curvature*, Experiments in Fluids **1**, 23-30.

Helmholtz, H. von 1868 *Über discontinuirliche Flüssigkeitsbewegungen*, Monats. Königl. Preuss. Akad. Wiss. Berlin **23**, 215-228. Translated into English by F.

Guthrie as *On discontinuous movements of fluids*, Phil. Mag. (4) **36**, 337-346. (1868)

Hunt, I.A. and Joubert, P.N. 1979 *Effects of small streamline curvature on turbulent duct flow*, J. Fluid Mech. **91**, 633-659.

Jeffreys, H. 1928 *Some cases of instability in fluid motion*, Proc. Roy. Soc. **A 118**, 195-208; also, *Collected Papers* (1975), Vol. 4, 469-484. Gordon and Beach, London.

Kelvin, Lord 1871 *Hydrokinetic solutions and observations*, Phil. Mag. (4), **42**, 362-377; also, *Mathematical and Physical Papers* (1910), Vol. IV, 69-85. Cambridge Univ. Press.

Knight, D.D. and Saffman, P.G. 1978 *Turbulence model predictions for flows with significant mean streamline curvature*, AIAA Paper 78-258.

Ko, S.H. and Lessen, M. 1969 *Low Reynolds number instability of an incompressible half-jet*, Phys. Fluids **12**, 404-407.

Konrad, J.H. 1976 *An experimental investigation of mixing in two-dimensional turbulent shear flows with applications to diffusion-limited chemical reactions*, Ph.D. Thesis, California Institute of Technology; also Project SQUID Technical Report CIT-8-PU, 1976.

Lamb, H 1932 "Hydrodynamics", 6th ed. Cambridge Univ. Press.

Landau, L.D. and Liftshitz, E.M. 1959 'Fluid Mechanics", (translated into English by J.B. Sykes and W.H. Reid), Pergamon Press.

Lessen, M. 1949 *On the stability of the free laminar boundary layer between parallel streams*, NACA TN 1929.

Lessen, M. and Ko, S.H. 1966 *Viscous instability of an incompressible fluid half-jet flow*, Phys. Fluids **9**, 1179-1183.

Lessen, M. and Singh, P.J. 1974 *Stability of turbulent jets and wakes*, Phys. Fluids **17**, 1329-1330.

Lewis, D.J. 1950 *The instability of liquid surfaces when accelerated in a direction perpendicular to their planes, II*, Proc. Roy. Soc. **A 202**, 81-96.

Liepmann, H.W. 1943 *Investigations on laminar boundary layer stability and transition on curved boundaries*, ARC RM 7302; also, NACA Wartime Rep. W-107.

(1943)

Liepmann, H.W. 1979 *The rise and fall of ideas in turbulence*, American Scientist **67**, 221-228.

Margolis, D.P. 1965 *Further studies of the curved turbulent mixing layer*, Final Report, Dept. Mech. Eng., Pennsylvania State Univ.

Margolis, D.P. and Lumley, J.L. 1965 *Curved turbulent mixing layer*, Phys. Fluids **8**, 1775-1784.

Maslowe, D.P. and Kelly, R.E. 1971 *Inviscid instability of an unbounded heterogeneous shear layer*, J. Fluid Mech. **48**, 405-415.

Maslowe, D.P. and Thompson, J.M. 1971 *Stability of a stratified free shear layer*, Phys. Fluids **14**, 453-458.

Michalke, A 1964 *On the inviscid instability of the hyperbolic-tangent velocity profile*, J. Fluid Mech. **19**, 543-556.

Michalke, A 1965a *Vortex formation in a free boundary layer according to stability theory*, J. Fluid Mech. **22**, 371-383.

Michalke, A 1965b *On spatially growing disturbances in an inviscid shear layer*, J. Fluid Mech. **23**, 521-544.

Moore, D.W. and Saffman, P.G. 1975 *The instability of a straight vortex filament in a strain field*, Proc. Roy. Soc. **A 346**, 413-425.

Oertel, H. 1982 In: "Flow Visualization II" (W. Merzkirch, ed.), Hemisphere, Washington, 71-76.

Oertel, H., Jr. and Kirchartz, K.R. 1979 In: "Recent Developments in Theoretical and Experimental Fluid Mechanics" (U. Müller, K.G. Roesner and B. Schmidt, eds.), Springer-Verlag, Berlin, 355-366.

Pellew, A. and Southwell, R.V. 1940 *On maintained convective motion in a fluid heated from below*, Proc. Roy. Soc. **A 176**, 312-343.

Pierrehumbert, R.T. and Widnall, S.E. 1982 *The two- and three-dimensional instabilities of a spatially periodic shear layer*, J. Fluid Mech. **114**, 59-82.

Plesset, M.S. and Whipple, C.G. 1974 *Viscous effects in Rayleigh-Taylor instability*, Phys. Fluids **17**, 1-7.

Ratafia, M. 1973 *Experimental investigation of Rayleigh-Taylor instability*, Phys. Fluids **16**, 1207-1210.

Rayleigh, Lord 1880 *On the stability, or instability, of certain fluid motions*, Proc. London Math. Soc. **11**, 57-70; also, "Scientific Papers" (1899) Vol.I, 474-487. Cambridge Univ. Press.

Rayleigh, Lord 1883 *Investigation of the character of the equilibrium of an incompressible heavy fluid of variable density*, Proc. London Math. Soc. **14**, 170-177; also, "Scientific Papers" (1900), Vol. II, 200-207. Cambridge Univ. Press.

Rayleigh, Lord 1916 *On the dynamics of revolving fluids* Proc. Roy. Soc. **A 93**, 148-154; also, "Scientific Papers" (1920), Vol VI, 447-453. Cambridge Univ. Press.

Reid, W.H. and Harris, D.L. 1958 *Some further results on the Benard problem*, Phys. Fluids **2**, 716-717.

Robinson, A.C. and Saffman, P.G. 1982 *Three-dimensional stability of vortex arrays*, J. Fluid Mech. **125**, 411-427.

Roshko, A. 1980 *The plane mixing layer flow visualization results and three dimensional effects*, in: "The Role of Coherent Structures in Modelling Turbulence and Mixing" (J. Jimenez ed.), Madrid, 207-217.

Sabin, C.M. 1965 *An analytical and experimental study of the plane, incompressible, turbulent free-shear layer with arbitrary velocity ratio and pressure gradient*, Trans. ASME **D 87**, 421-428.

Saffman, P.G. 1980 *Coherent structures in turbulent flow*, in: "The role of Coherent Structures in Modelling Turbulence and Mixing" (J. Jimenez ed.), Madrid, 1-9.

Scorer, R.S. 1978 "Environmental Aerodynamics", Ellis Horwood Limited, London.

Sharp, D.H. 1983 *An overview of Rayleigh-Taylor instability*, Presented at International Conference on Fronts, Interfaces and Patterns, Los Alamos Nat'l. Lab., May 2-6.

Stuart, J.T. 1967 *On finite amplitude oscillations in laminar mixing layers*, J. Fluid Mech. **29**, 417-440.

Synge, J.L. 1933 *The stability of heterogeneous liquids*, Trans. Roy. Soc. Canada **27**, 1-18.

Taylor, G.I. 1923 *Stability of a viscous liquid contained between two rotating cylinders*, Phil. Trans. **A 223**, 289-343; also, "Scientific Papers" (1971), Vol. IV, 34-85. Cambridge Univ. Press.

Taylor, G.I. 1931 *Effect of variation in density on the stability of superposed streams of fluid*, Proc. Roy. Soc. **A 132**, 499-523; also, "Scientific Papers" (1960), Vol. II, 219-239, Cambridge Univ. Press.

Taylor, G.I. 1950 *The instability of liquid surfaces when accelerated in a direction perpendicular to their planes, I*, Proc. Roy. Soc. **A 201**, 192-196; also, "Scientific Papers" (1963) Vol. III, 532-536. Cambridge Univ. Press.

Tollmien, W. 1935 *Ein allgemeines Kriterium der Instabilität laminarer Geschwindigkeitsverteilungen*, Nachr. Wiss. Fachgruppe, Göttingen, Math.-phys. Kl. 1, 79-114; translated as *General instability criterion of laminar velocity distribution*, NACA TM 792 (1936).

Tuzson, J. 1977 *Stability of a curved free streamline*, J. Fluids Engineering, Transactions of the ASME **99**, 603-605.

Weske, J.R. and Rankin, T.M. 1963 *Generation of secondary motions in the field of a vortex*, Phys. Fluids **6**, 1397-1403.

Wood, D.H. and Bradshaw, P. 1982 *A turbulent mixing layer constrained by a solid surface, Part 1. Measurements before reaching the surface*, J. Fluid Mech. **122**, 57-89.

Wyngaard, J.C. 1967 *An experimental investigation of the small-scale structure of turbulence in a curved mixing layer*, Ph.D. Thesis, Pennsylvania State Univ.

Wyngaard, J.C., Tennekes, H., Lumley, J.L., and Margolis, D.P. 1968 *Structure of turbulence in a curved mixing layer*, Phys. Fluids **11**, 1251-1253.

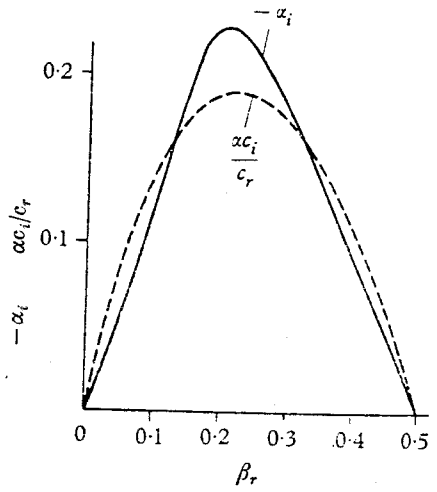

Fig. 1.1 Growth rate $-\alpha_i$ (or $\alpha\, c_i/c_r$) in an inviscid mixing layer as a function of frequency β_r for disturbances of the form exp [i(αx-βt)], ———, spatial case; -----, temporal case (Michalke 1965 b).

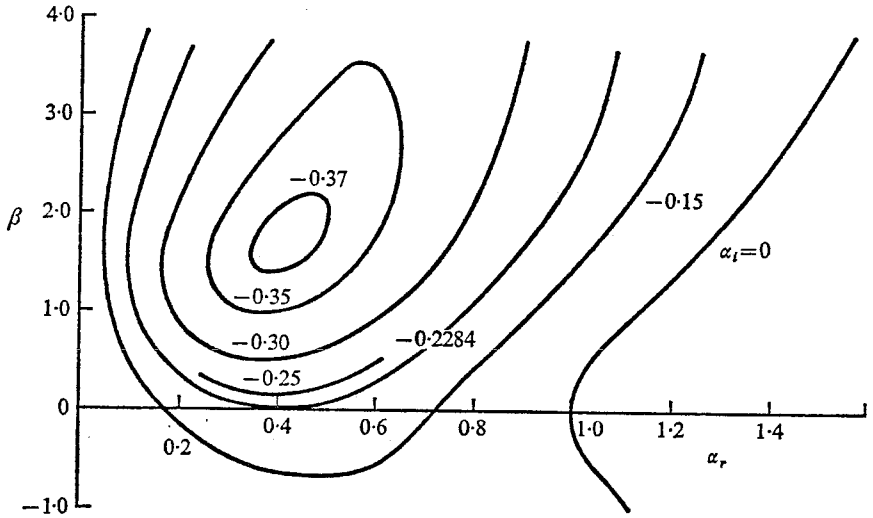

Fig. 1.2 Curves of constant spatial growth rate $-\alpha_i$ in an inviscid mixing layer for disturbances of the form exp [iα(x-ct)]. The density distribution is $\overline{\rho} = \exp(-\beta \tanh y)$ (Maslowe and Kelly 1971).

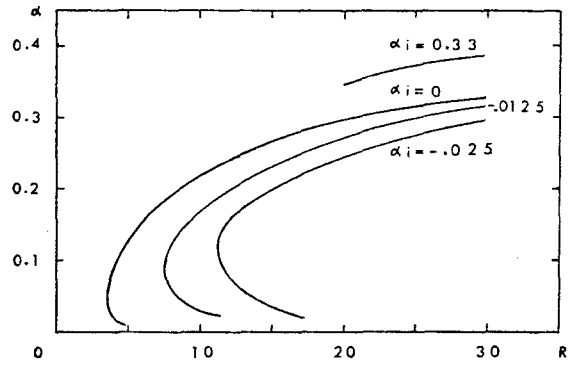

Fig. 1.3 Curves of constant spatial growth rate $-\alpha_i$ in a viscous mixing layer for disturbances of the form $\exp[i\alpha(x-ct)]$ (Lessen and Ko 1966).

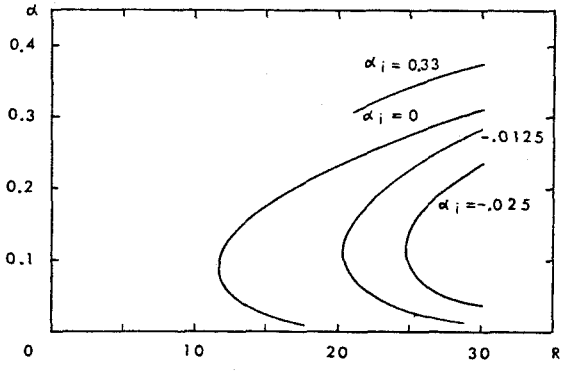

Fig. 1.4 Curves as in Fig. 1.3 after a correction for non-parallel flow (Lessen and Ko 1966).

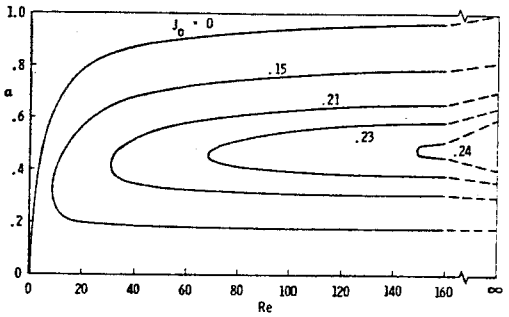

Fig 1.5 Neutral stability curves for viscous flow for various Richardson numbers; temporal growth for disturbances of the form $\exp[i\alpha(x-ct)]$ with real α. The density distribution is $\overline{\rho} = \exp(-\beta \tanh y)$, with $J_o = g\beta$ (Maslowe and Thompson 1971).

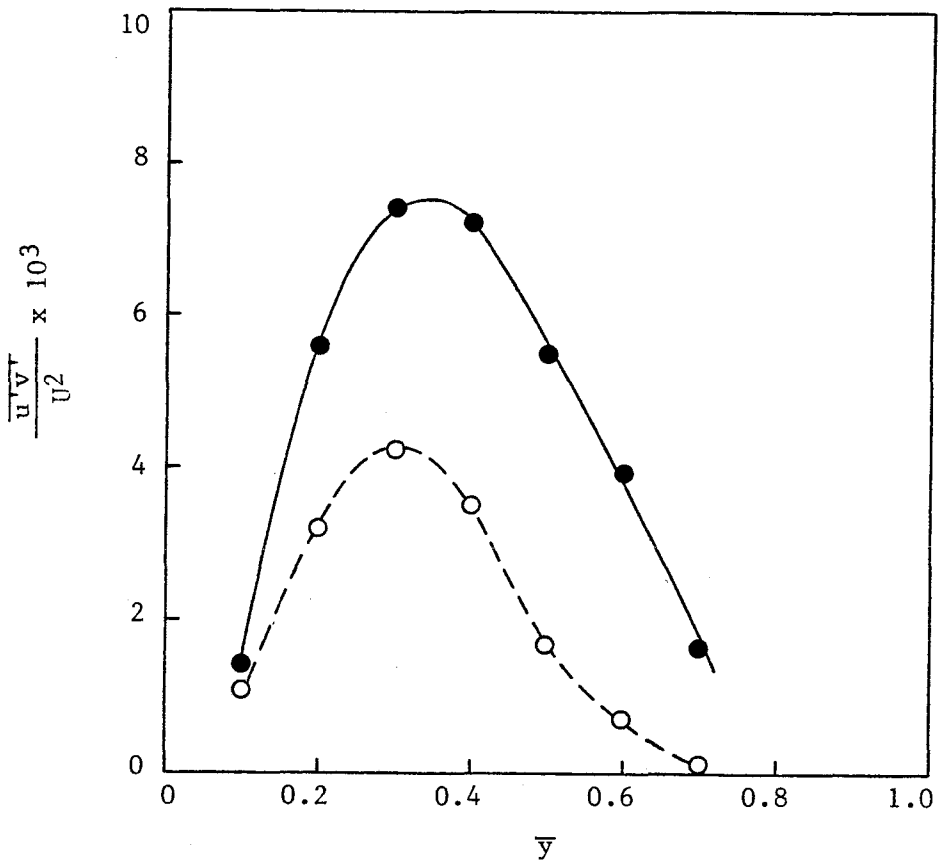

Fig. 1.6 Reynolds stress in a curved shear layer at an angular location $\theta = 60^{o}$. The abscissa $\overline{y}$ is the radial distance normalized by channel height; U is the velocity of the high-speed stream. ● , inner stream faster; ○ , outer stream faster (Wyngaard 1967).

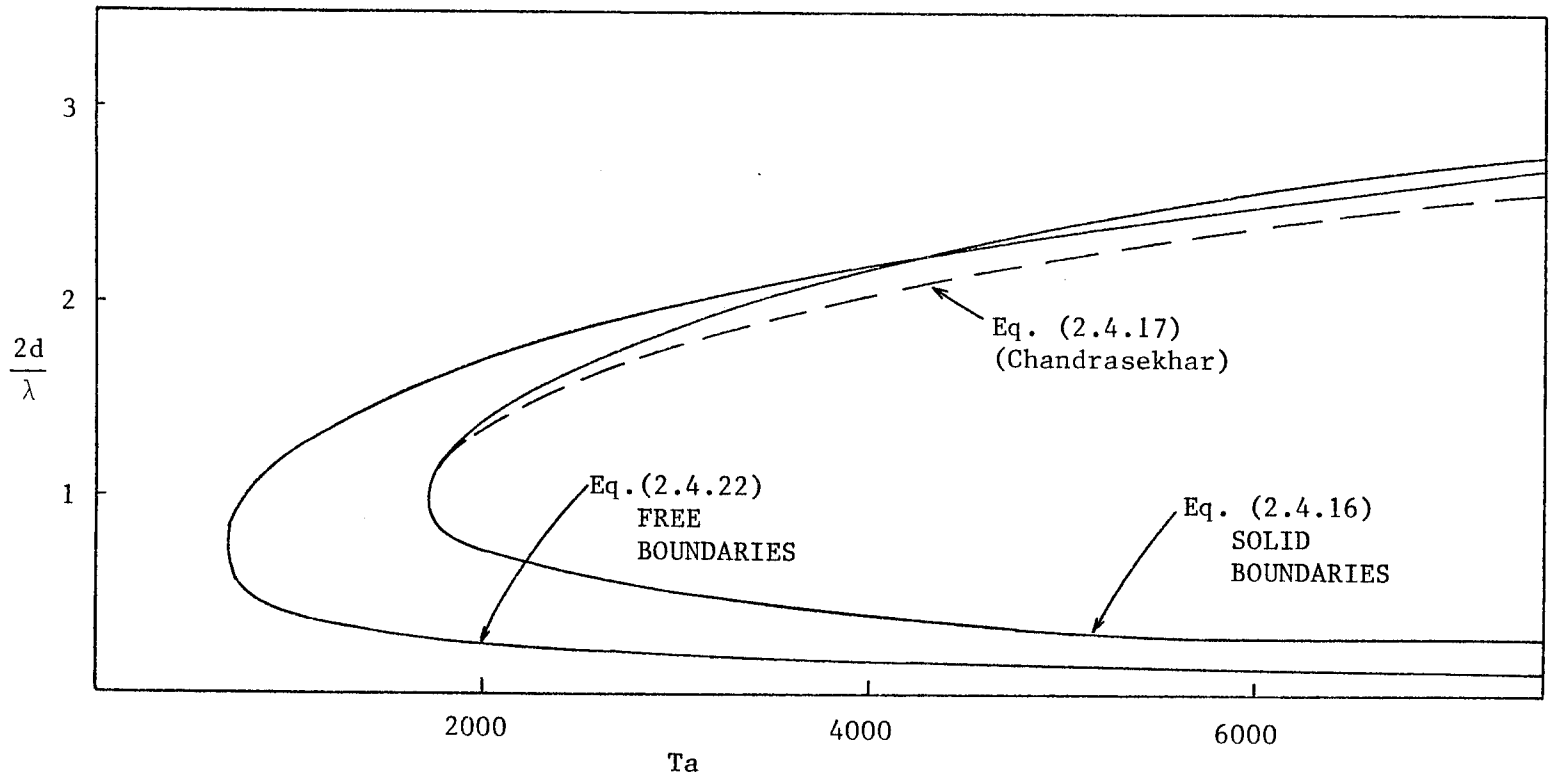

Fig. 2.1 Neutral stability boundaries for Taylor-Görtler instability with constant density. The solid lines are from the present algebraic approximation. The dashed line is from the analytic solution (Chandrasekhar 1961).

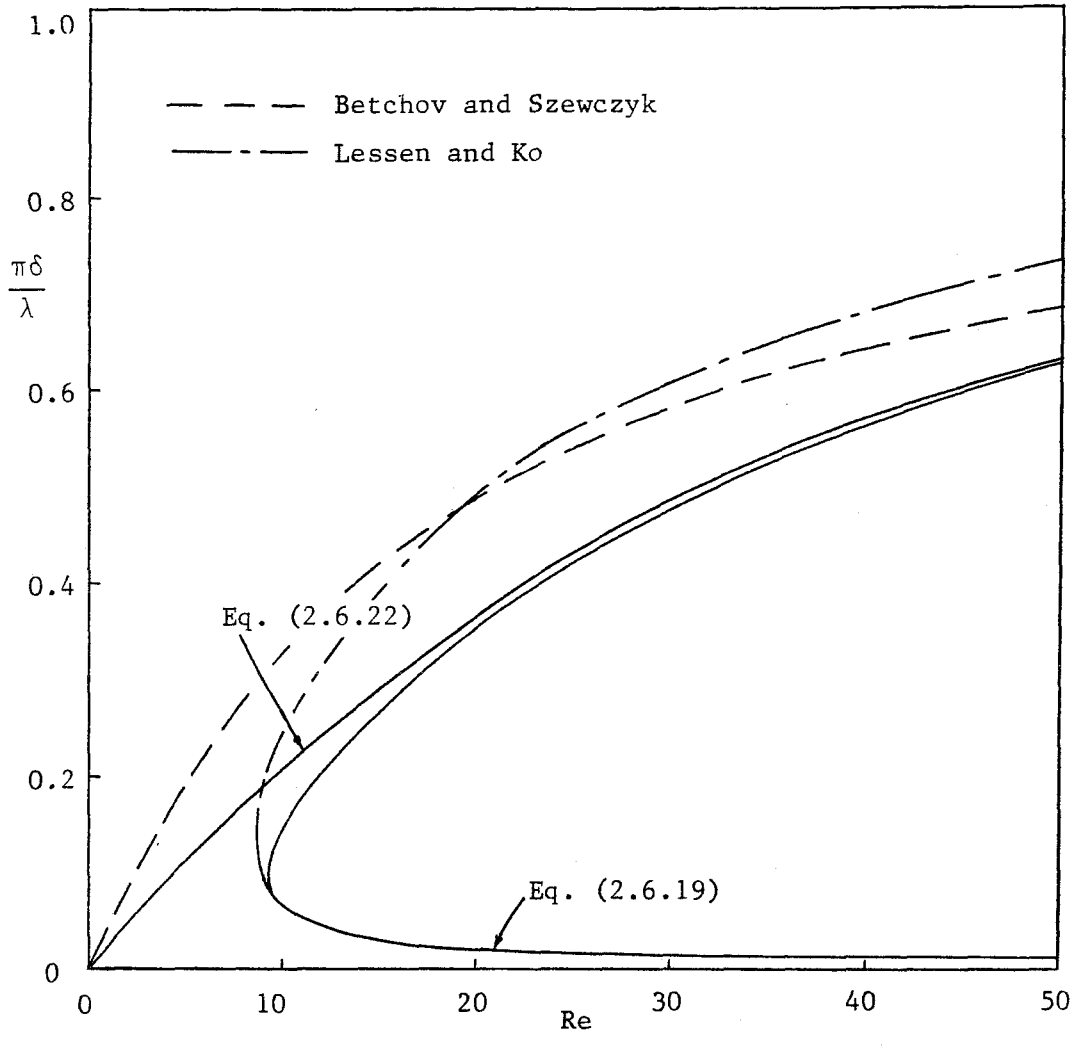

Fig. 2.2 Neutral stability boundaries for Kelvin-Helmholtz instability with constant density. The solid lines are from the present algebraic approximation. The dashed lines are from analytic solutions (Betchov and Szewczyk 1963 and Lessen and Ko 1966).

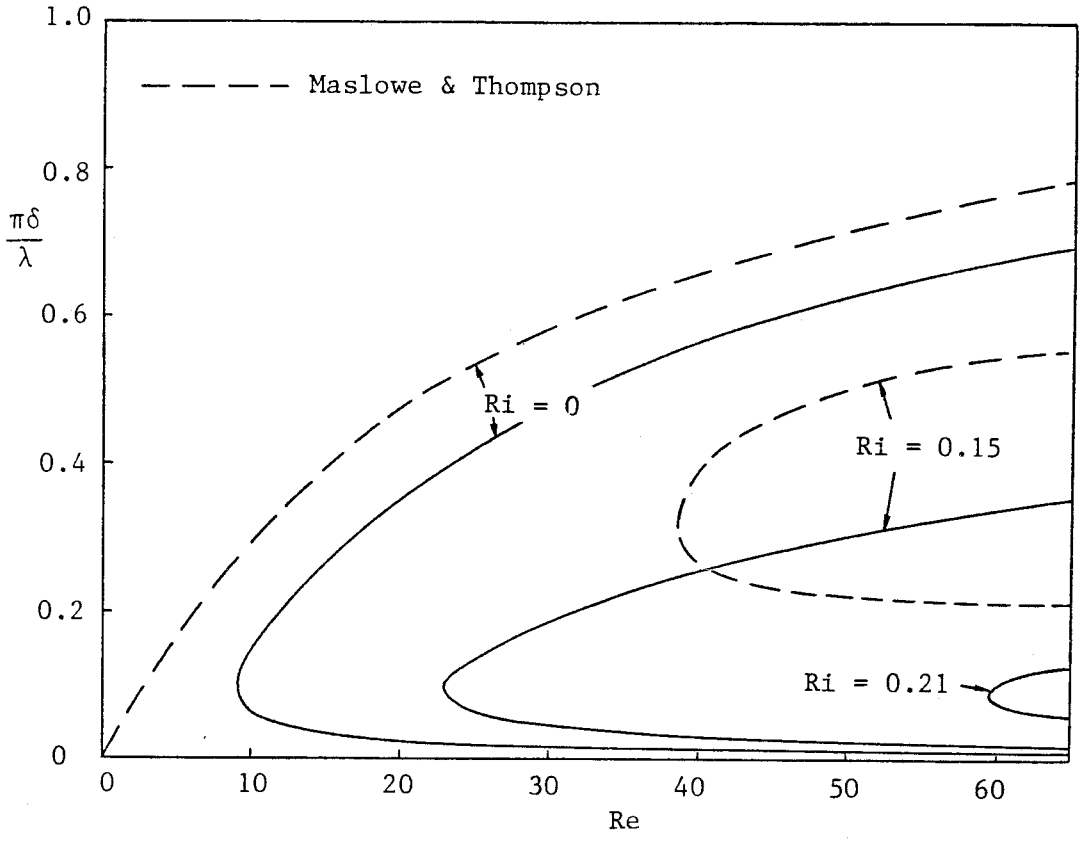

Fig. 2.3 Neutral stability boundaries for Kelvin-Helmholtz instability with density difference. The solid lines are from the present algebraic approximation for Pr = ∞. The dashed lines are from analytical solutions for Pr = 0.72. (Maslowe and Thompson 1971). The Richardson number Ri is defined by Eq. (2.7.6).

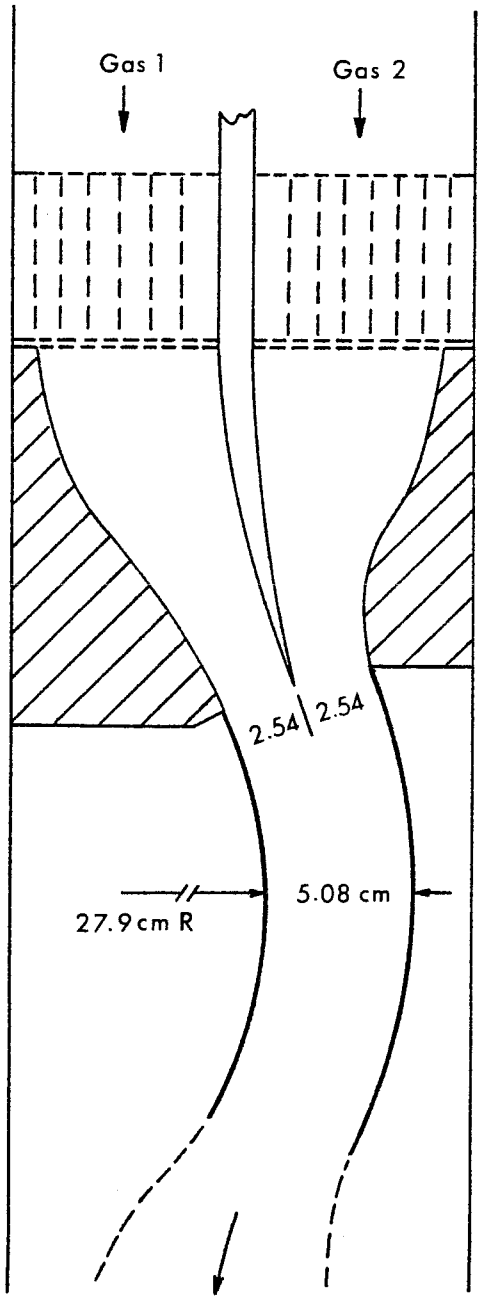

Fig. 3.1 Detail of the nozzle and the curved channel.

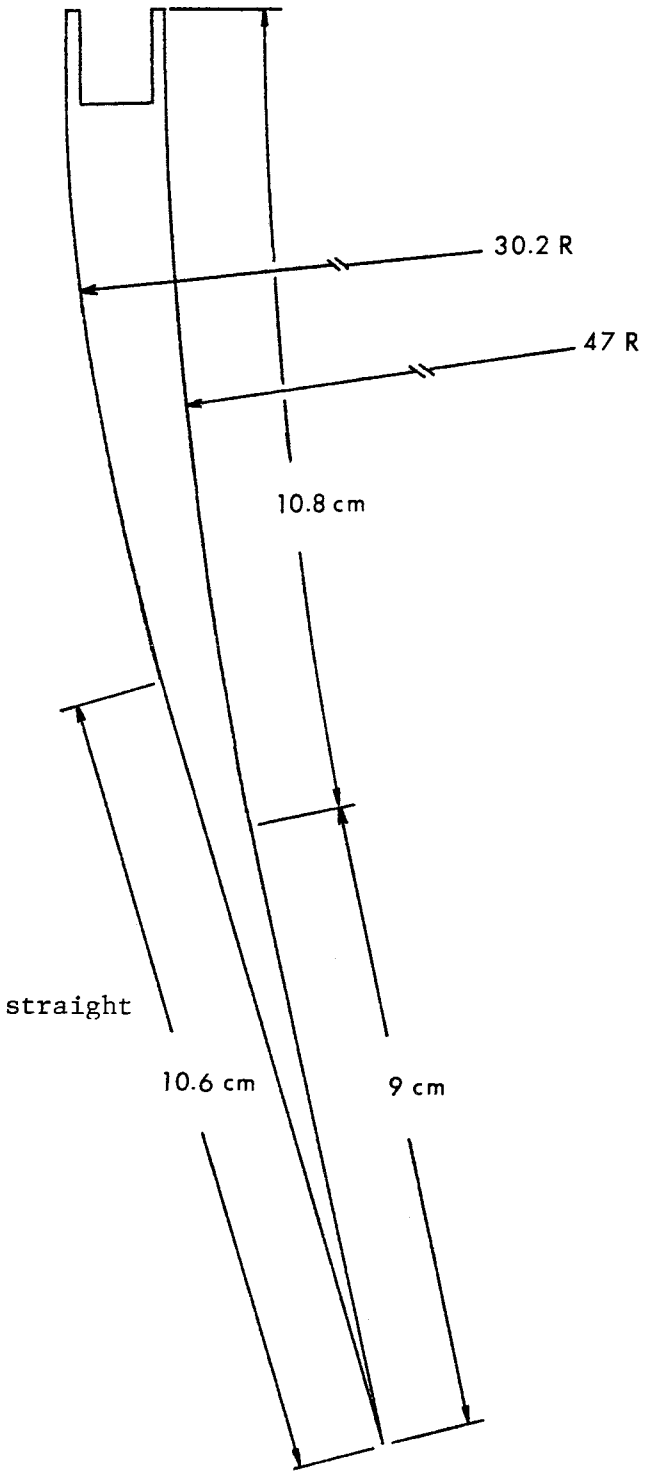

Fig. 3.2 Detail of the splitter plate.

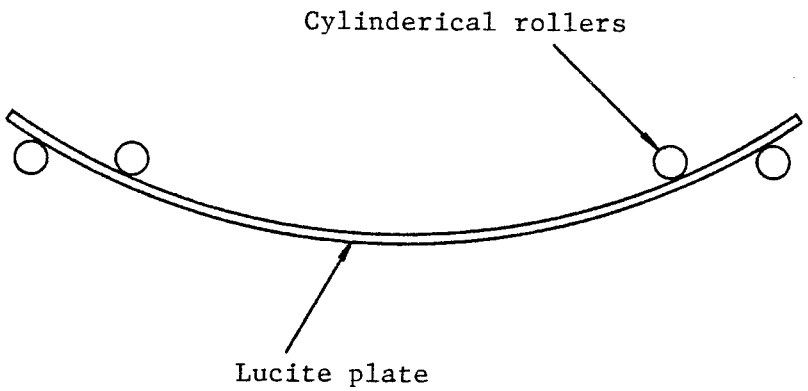

Fig. 3.3 The fixture used for forming the curved walls.

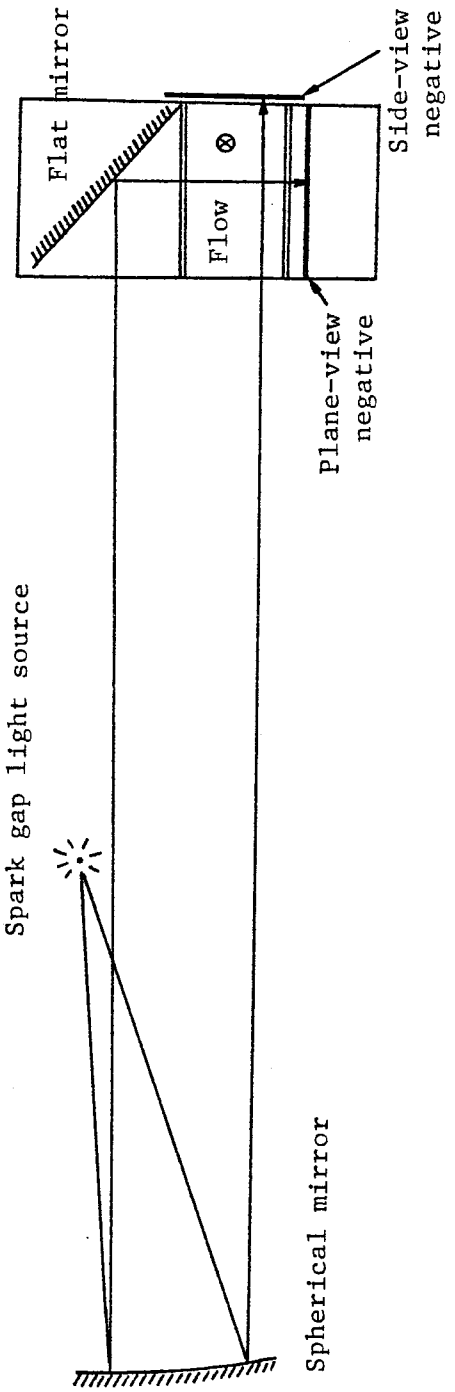

Fig. 3.4 The shadowgraph system; original configuration.

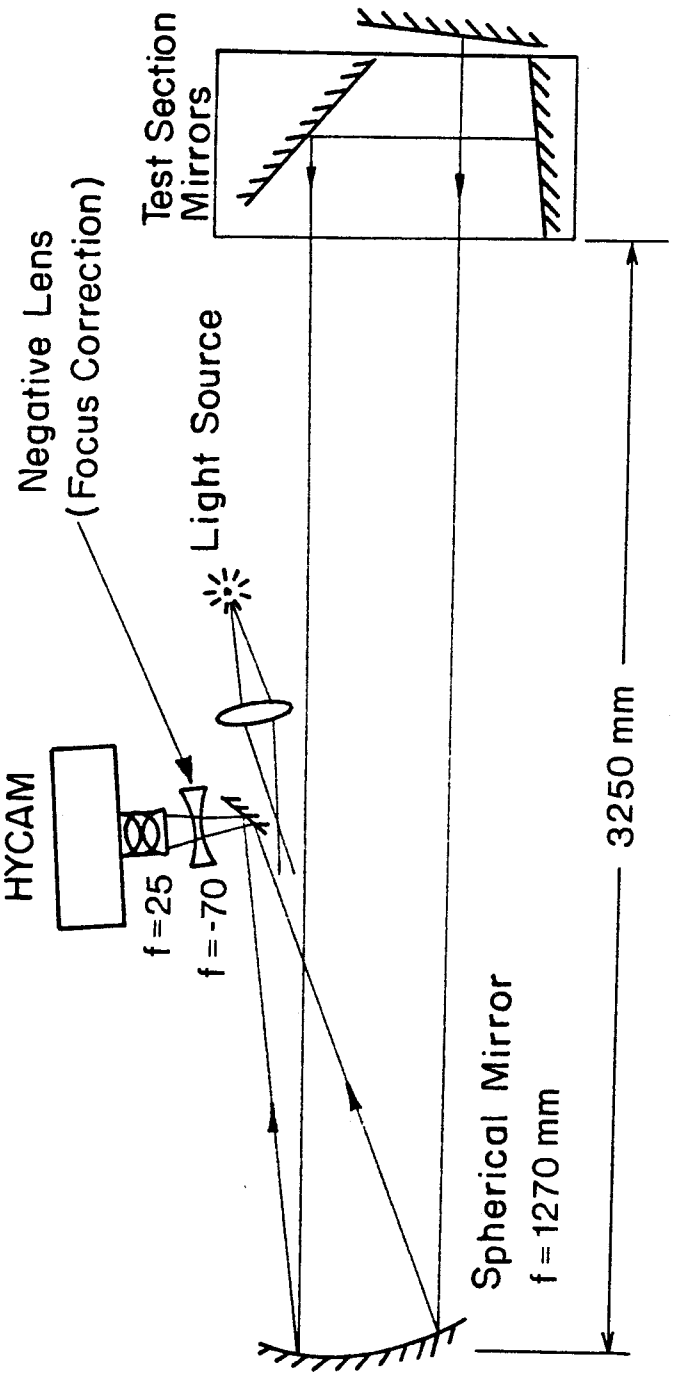

Fig. 3.5 The double-pass focused shadowgraph system.

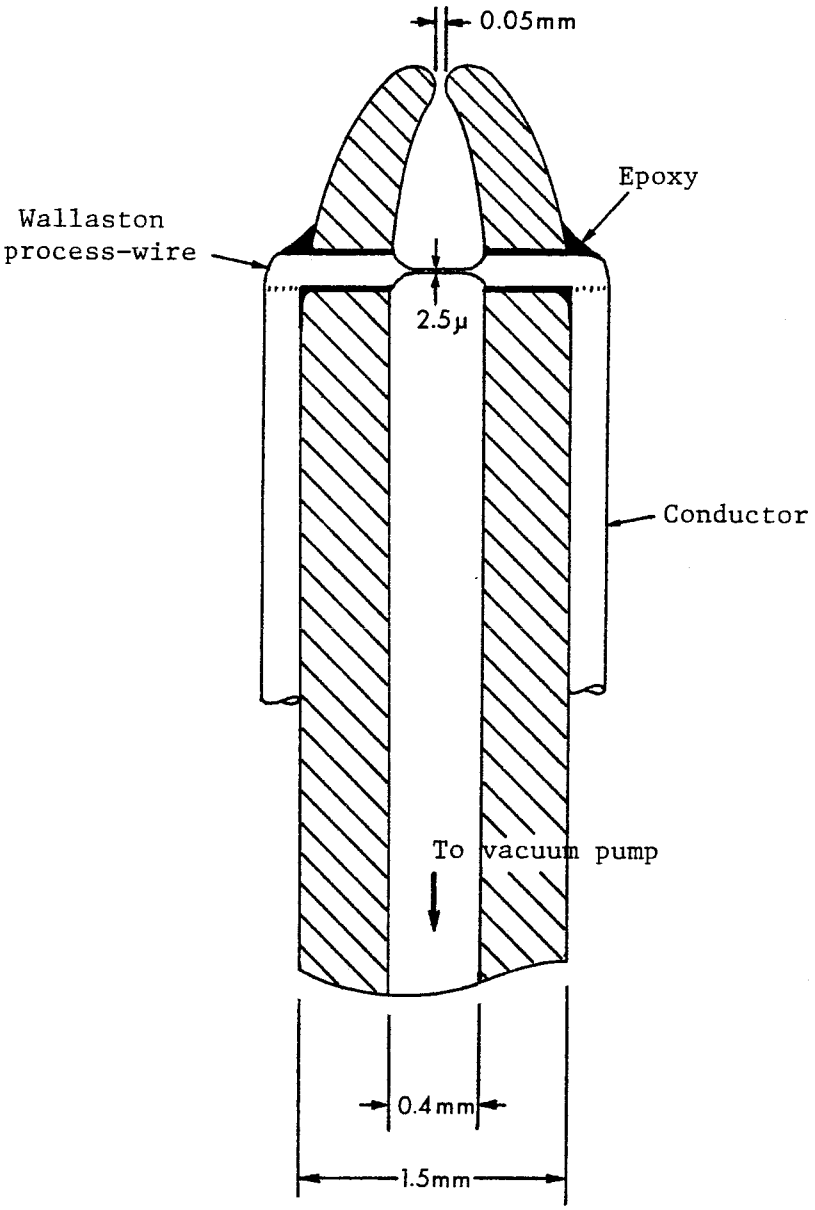

Fig. 3.6 Detail of the concentration probe.

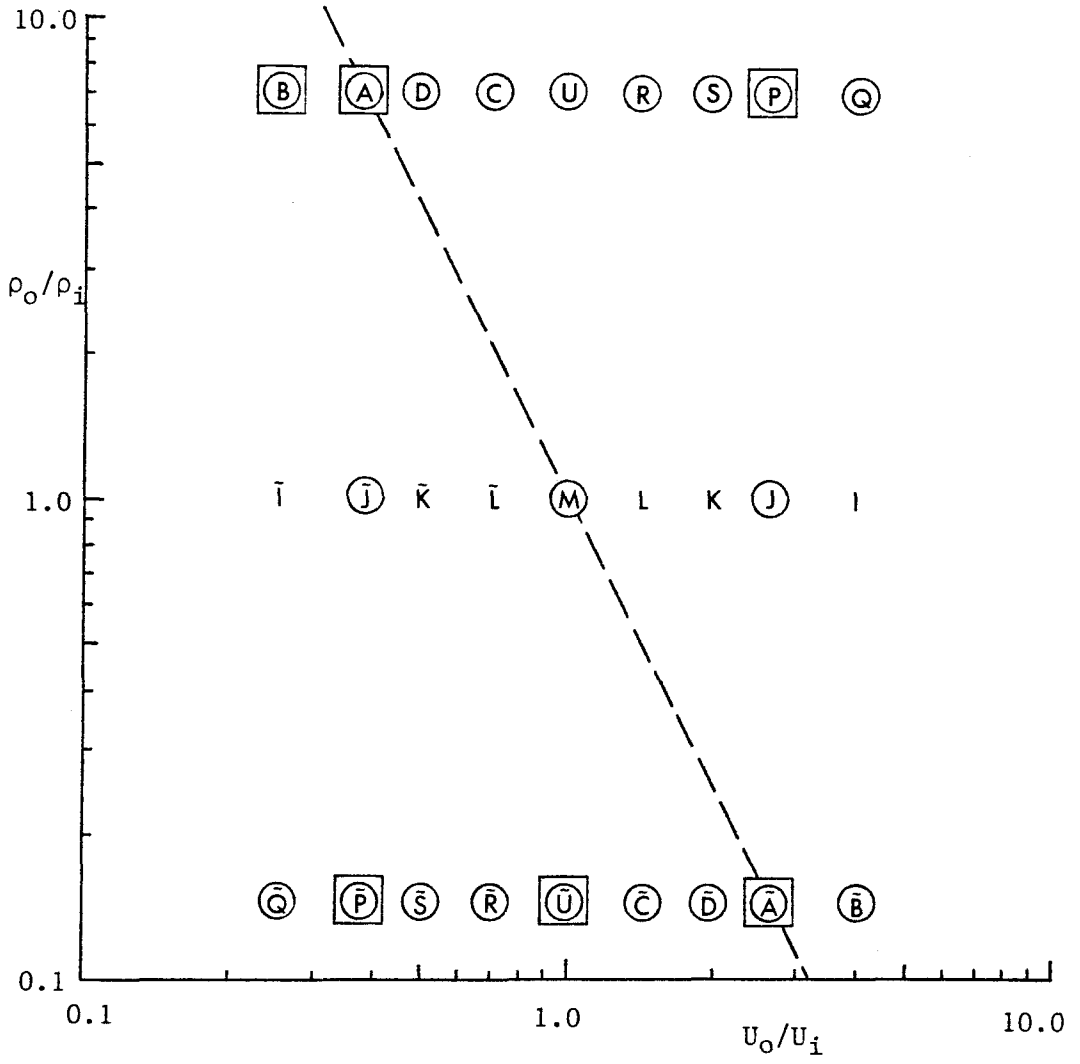

Fig. 4.1 Organization of the experiments. The capital letters correspond to the flow conditions listed in Table 1. ◯, movies are available; □, Profile measurements are available. Pairs like S and $\tilde{S}$ have the same velocity values and the same density values, except for the sense of the channel curvature. The dashed line represents the inviscid neutral stability boundary according to the Rayleigh-Synge criterion, $\rho_o U_o^2 = \rho_i U_i^2$.

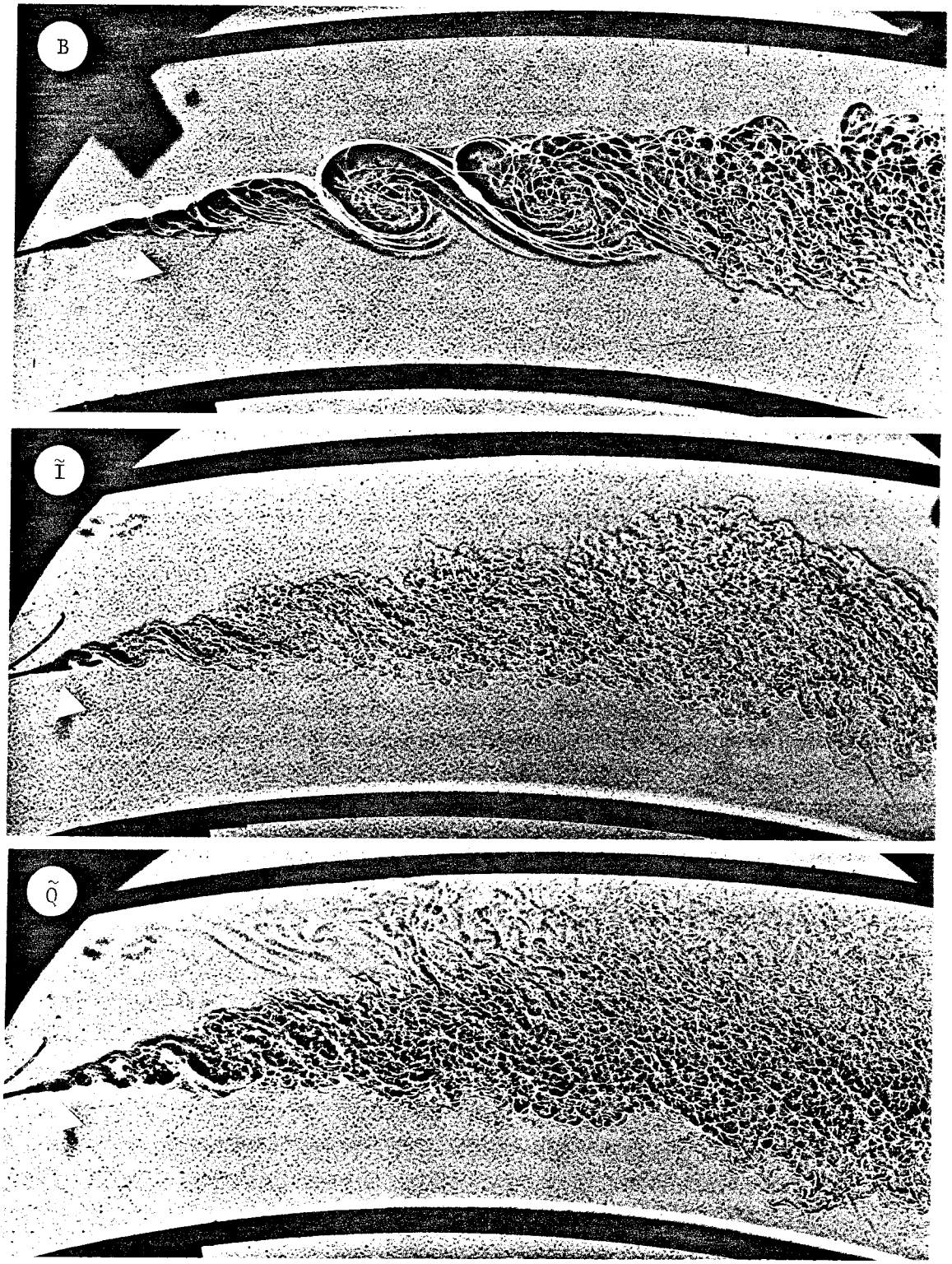

Fig. 5.1 (a) $U_o/U_i = 0.25$; $\rho_o/\rho_i = 7/1$ (top)
$\rho_o/\rho_i = 1/1$ (middle)
$\rho_o/\rho_i = 1/7$ (bottom).

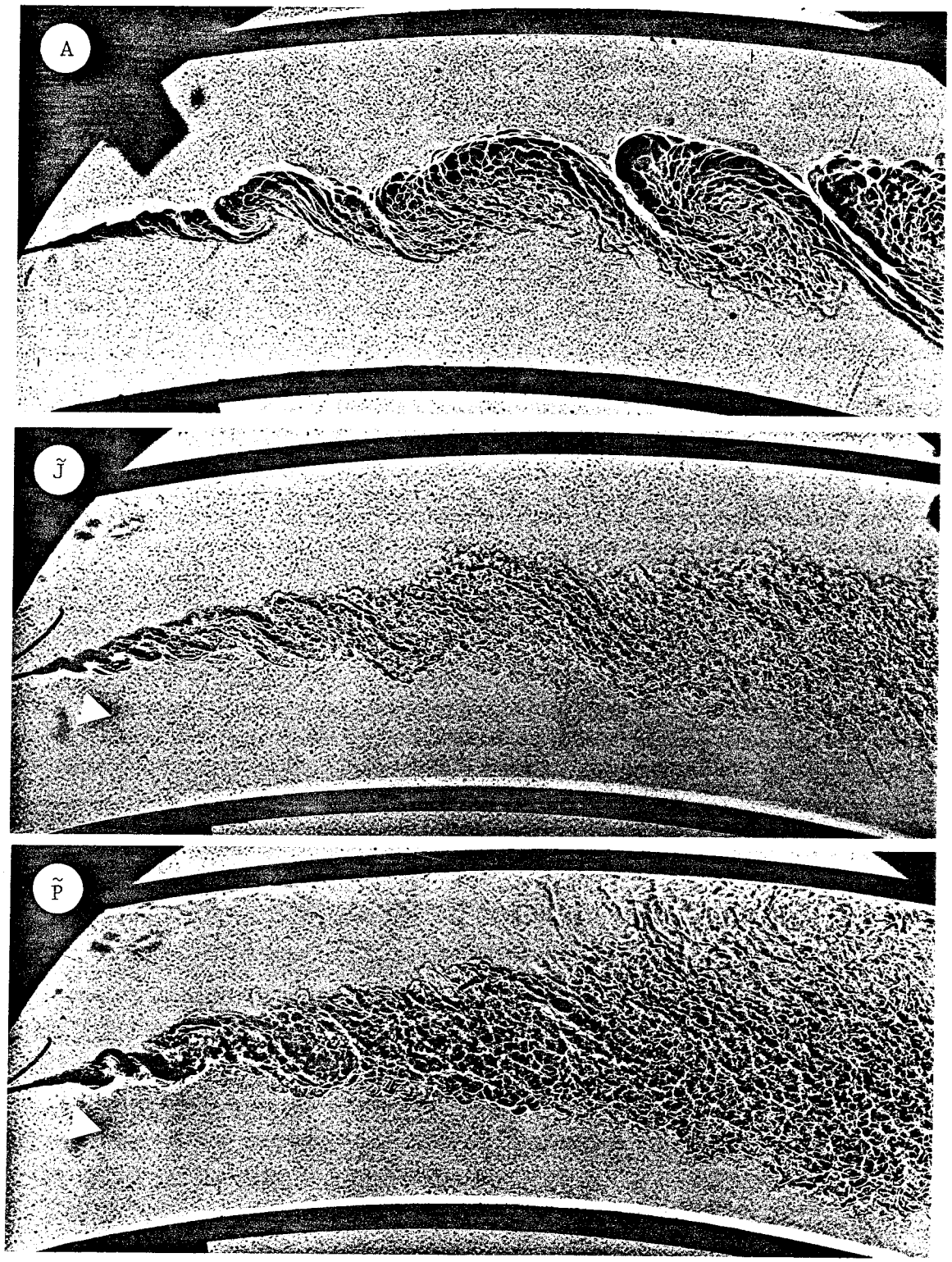

Fig. 5.1 (b) $U_o/U_i = 0.38$; $\rho_o/\rho_i = 7/1$ (top)
$\rho_o/\rho_i = 1/1$ (middle)
$\rho_o/\rho_i = 1/7$ (bottom).

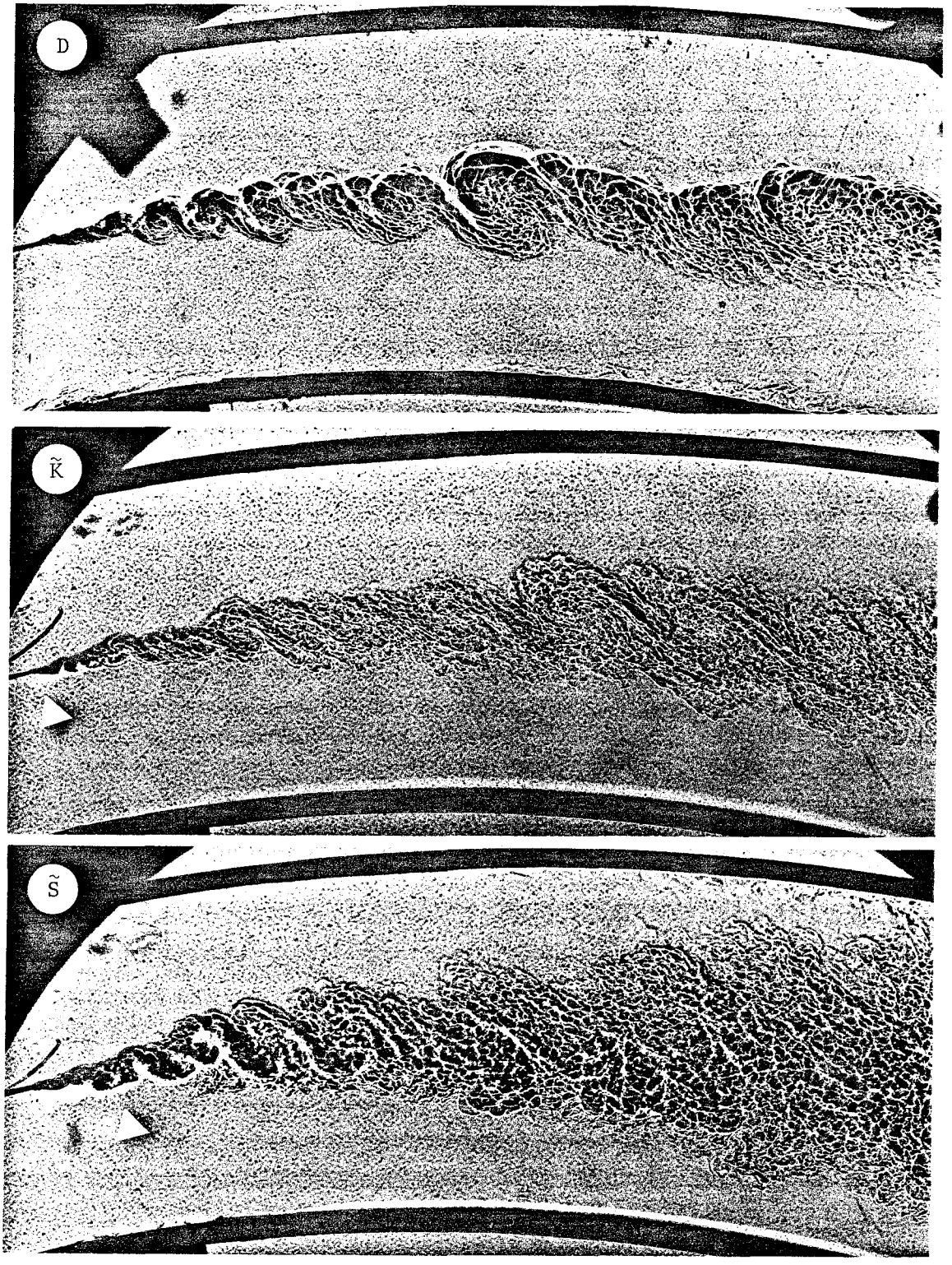

Fig. 5.1 (c) $U_o/U_i = 0.50$; $\rho_o/\rho_i = 7/1$ (top)
$\rho_o/\rho_i = 1/1$ (middle)
$\rho_o/\rho_i = 1/7$ (bottom).

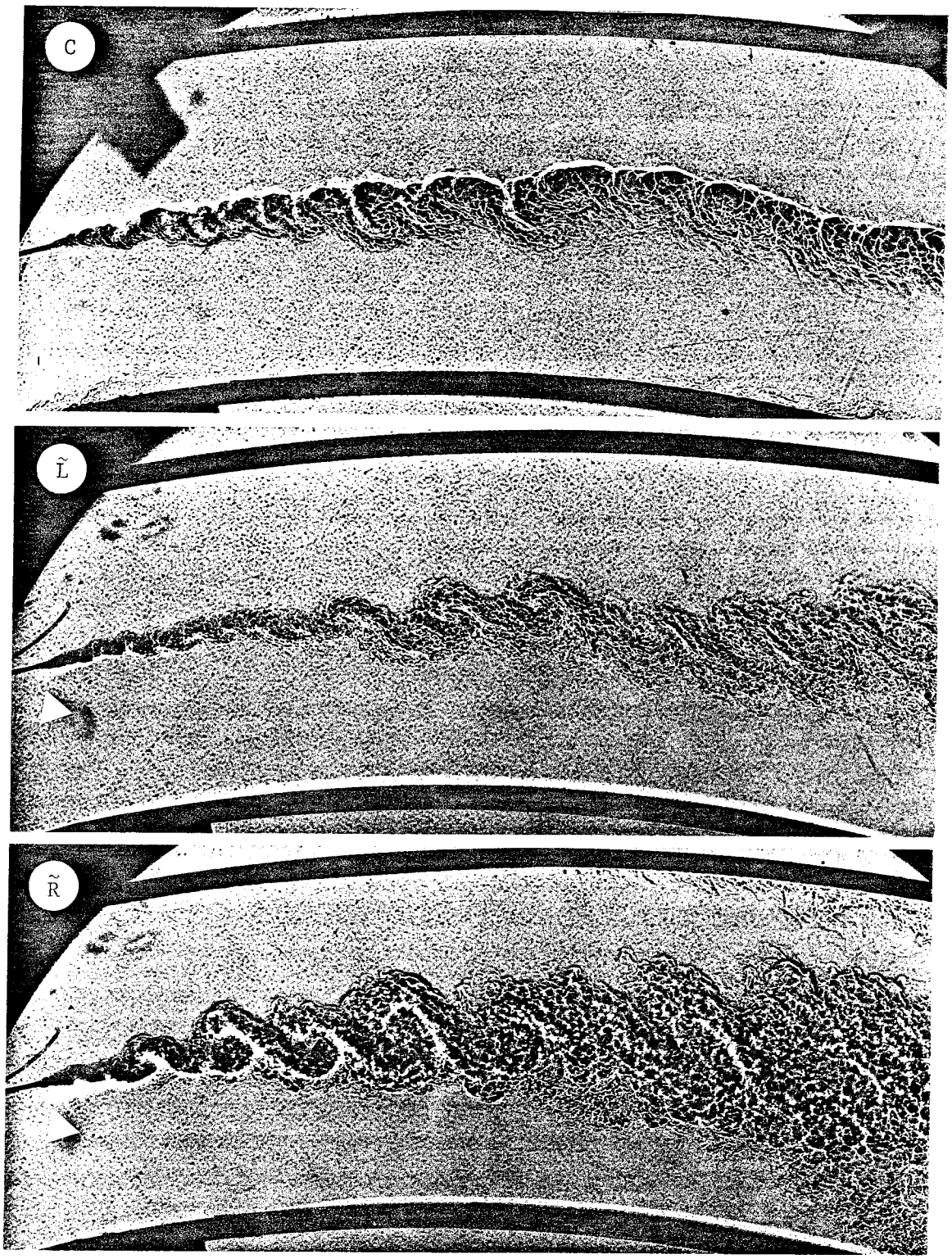

Fig. 5.1 (d) $U_o/U_i = 0.70$; $\rho_o/\rho_i = 7/1$ (top)
$\rho_o/\rho_i = 1/1$ (middle)
$\rho_o/\rho_i = 1/7$ (bottom).

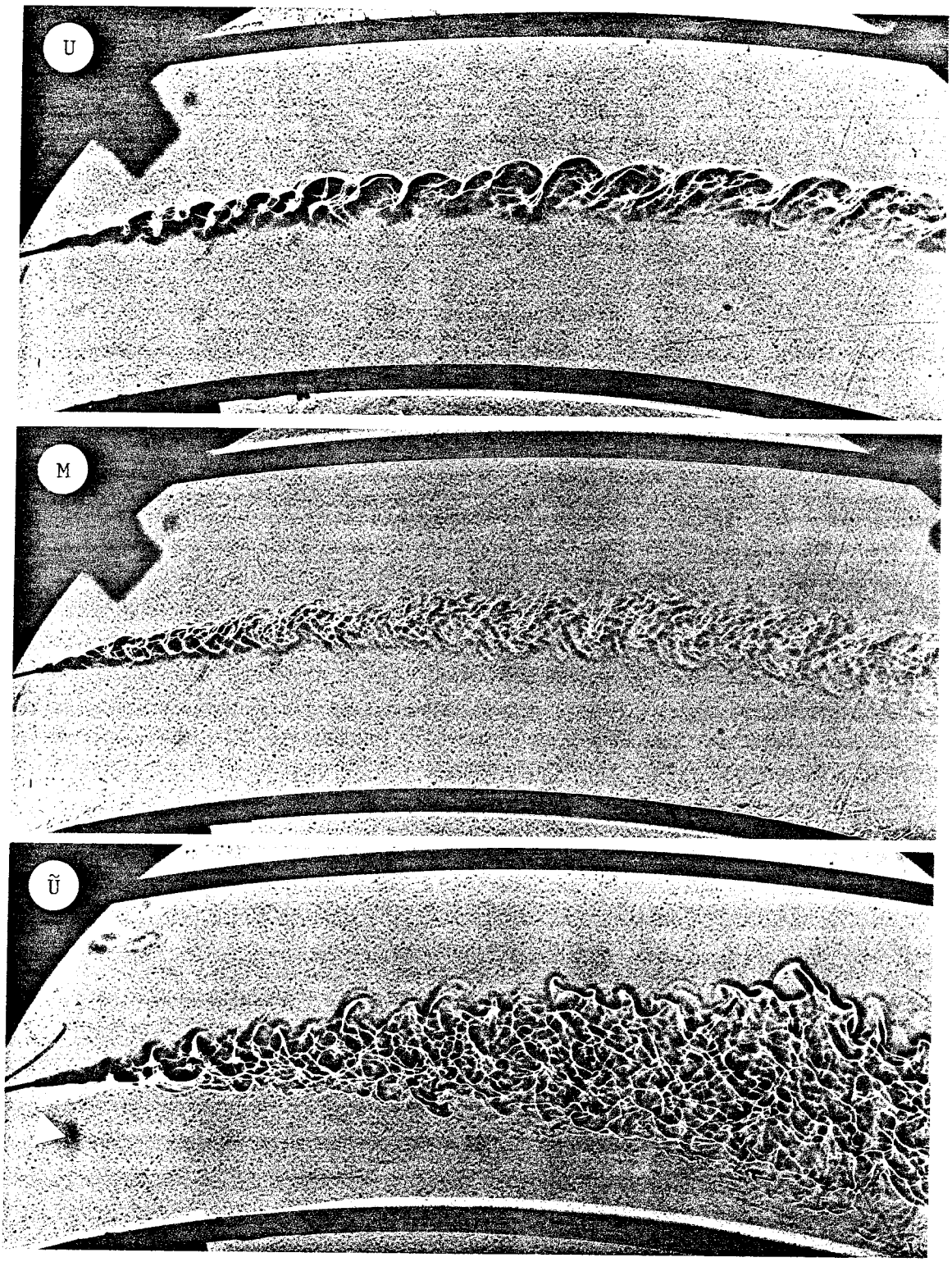

Fig. 5.1 (e) $U_o/U_i = 1.0$; $\rho_o/\rho_i = 7/1$ (top)
$\rho_o/\rho_i = 1/1$ (middle)
$\rho_o/\rho_i = 1/7$ (bottom).

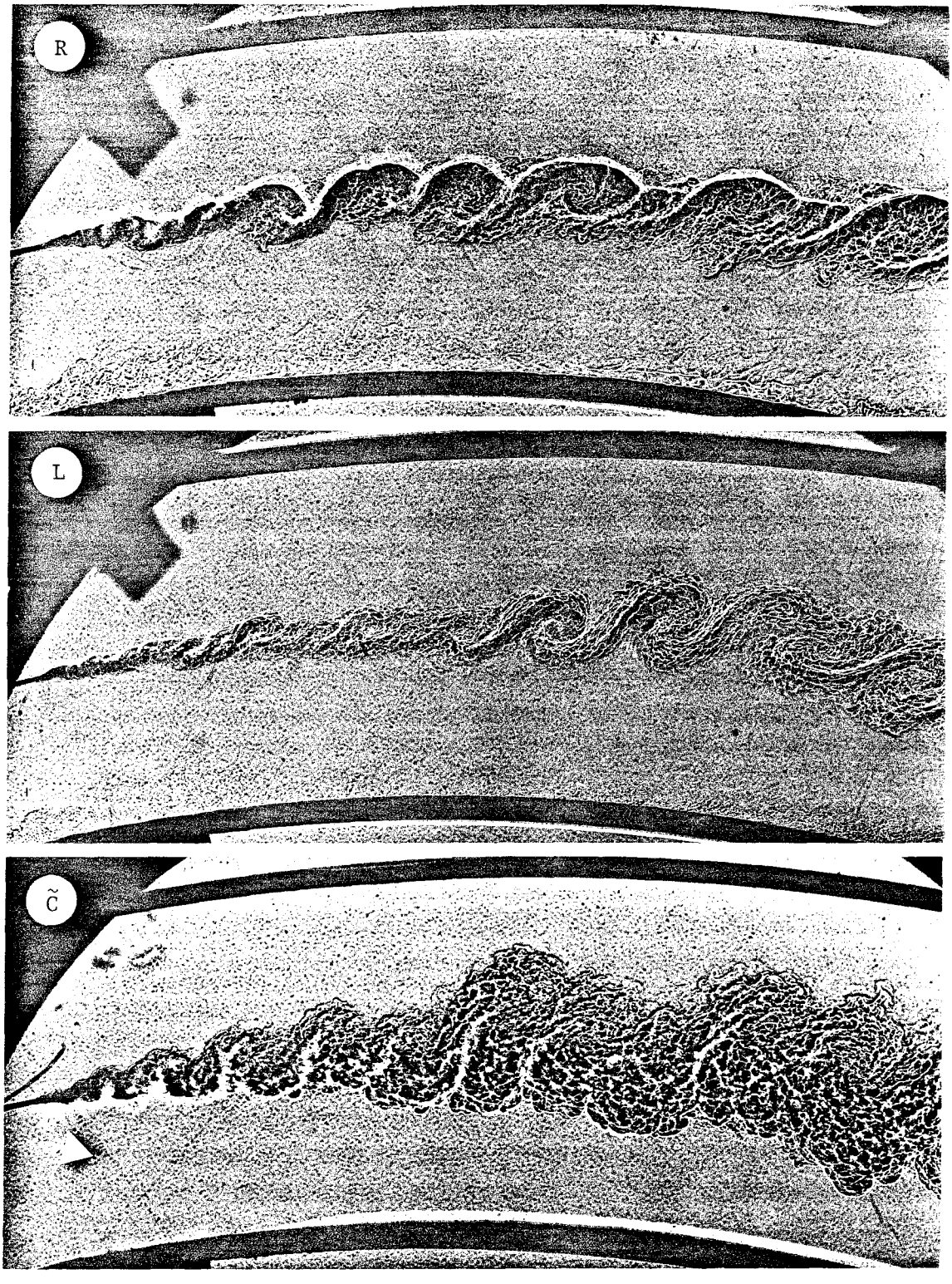

Fig. 5.1 (f) $U_o/U_i = 1.43$; $\rho_o/\rho_i = 7/1$ (top)
$\rho_o/\rho_i = 1/1$ (middle)
$\rho_o/\rho_i = 1/7$ (bottom).

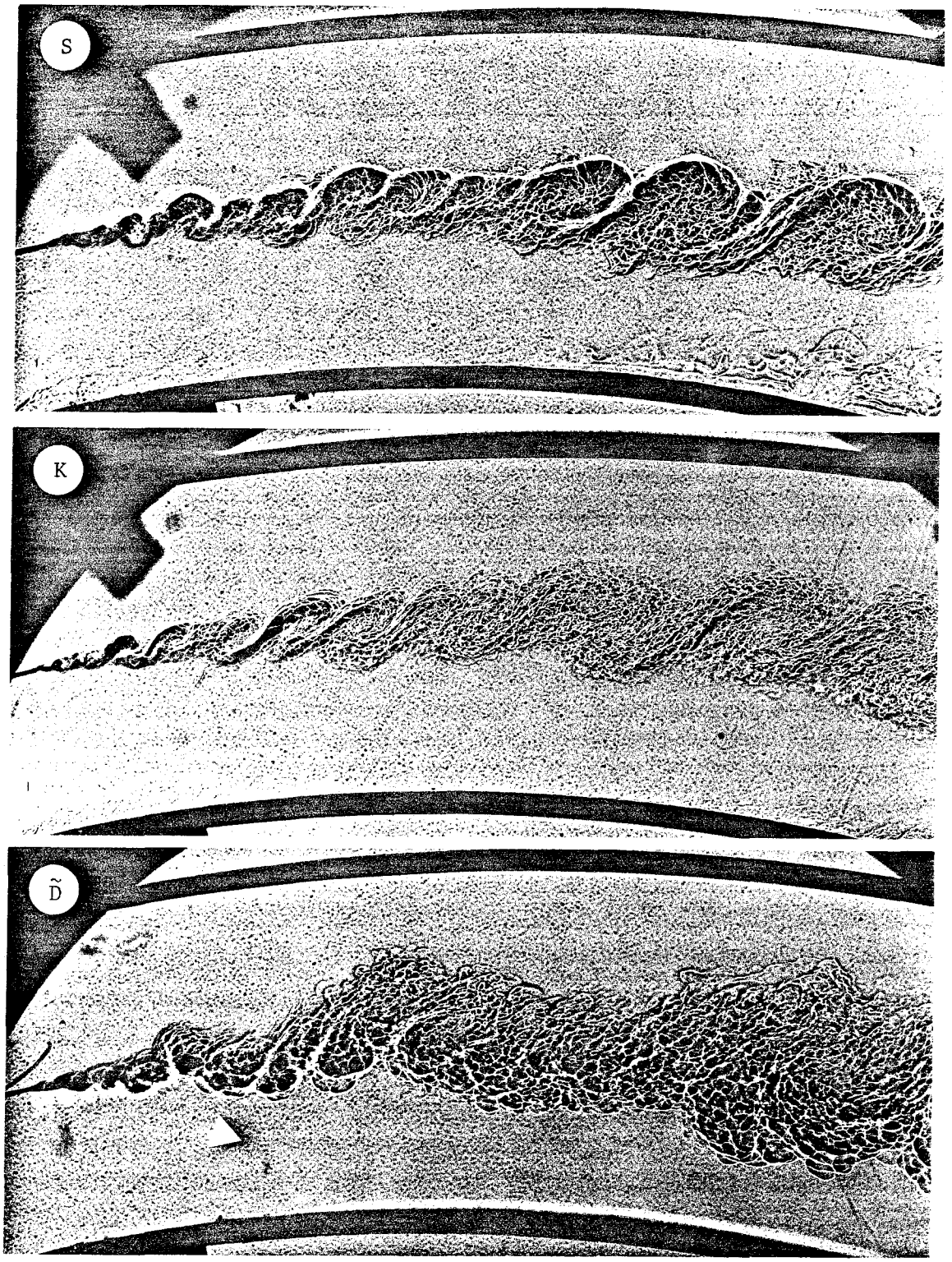

Fig. 5.1 (g) $U_o/U_i = 2.00$; $\rho_o/\rho_i = 7/1$ (top)
$\rho_o/\rho_i = 1/1$ (middle)
$\rho_o/\rho_i = 1/7$ (bottom).

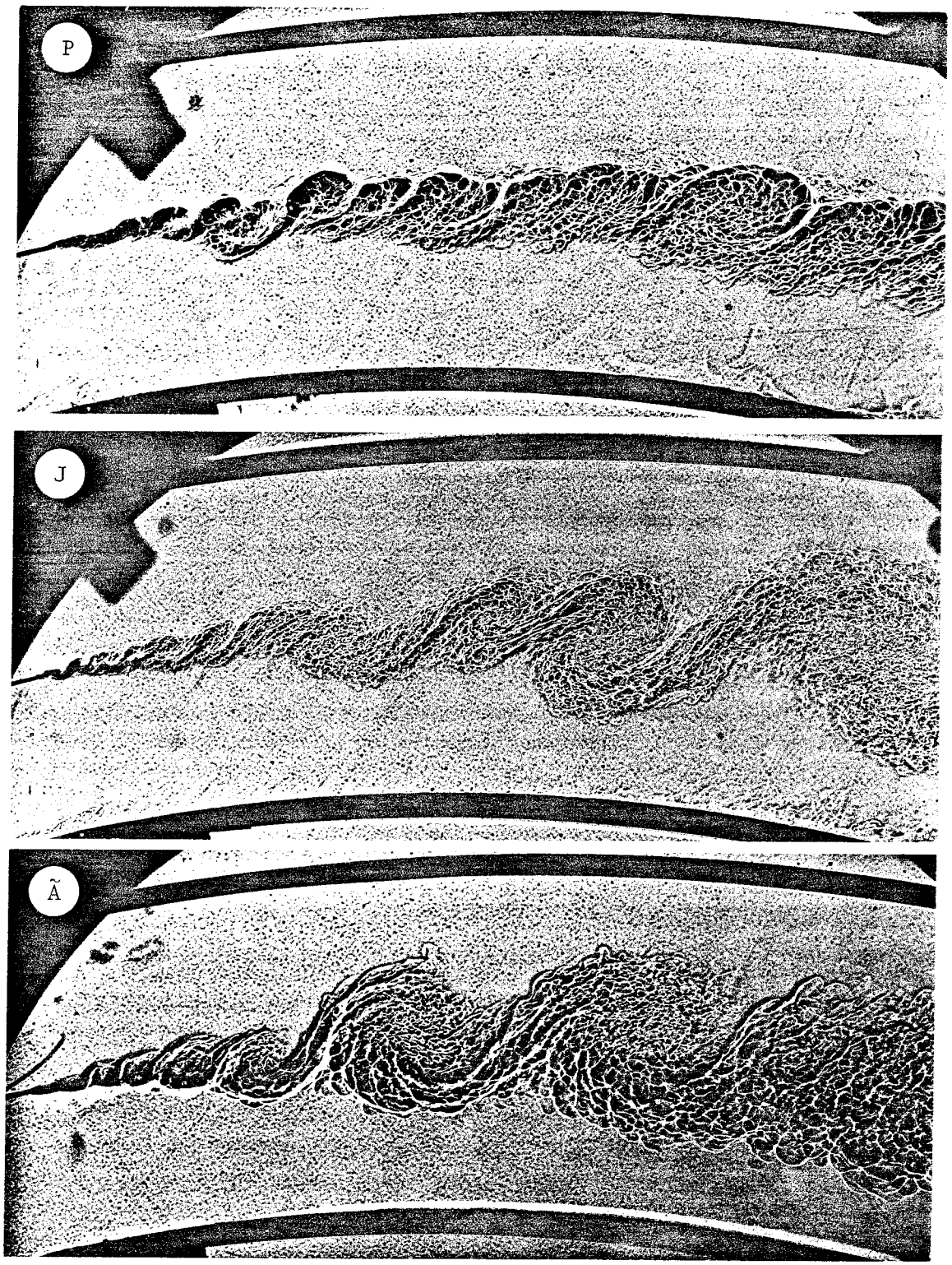

Fig. 5.1 (h) U_o/U_i = 2.63; ρ_o/ρ_i = 7/1 (top)
ρ_o/ρ_i = 1/1 (middle)
ρ_o/ρ_i = 1/7 (bottom).

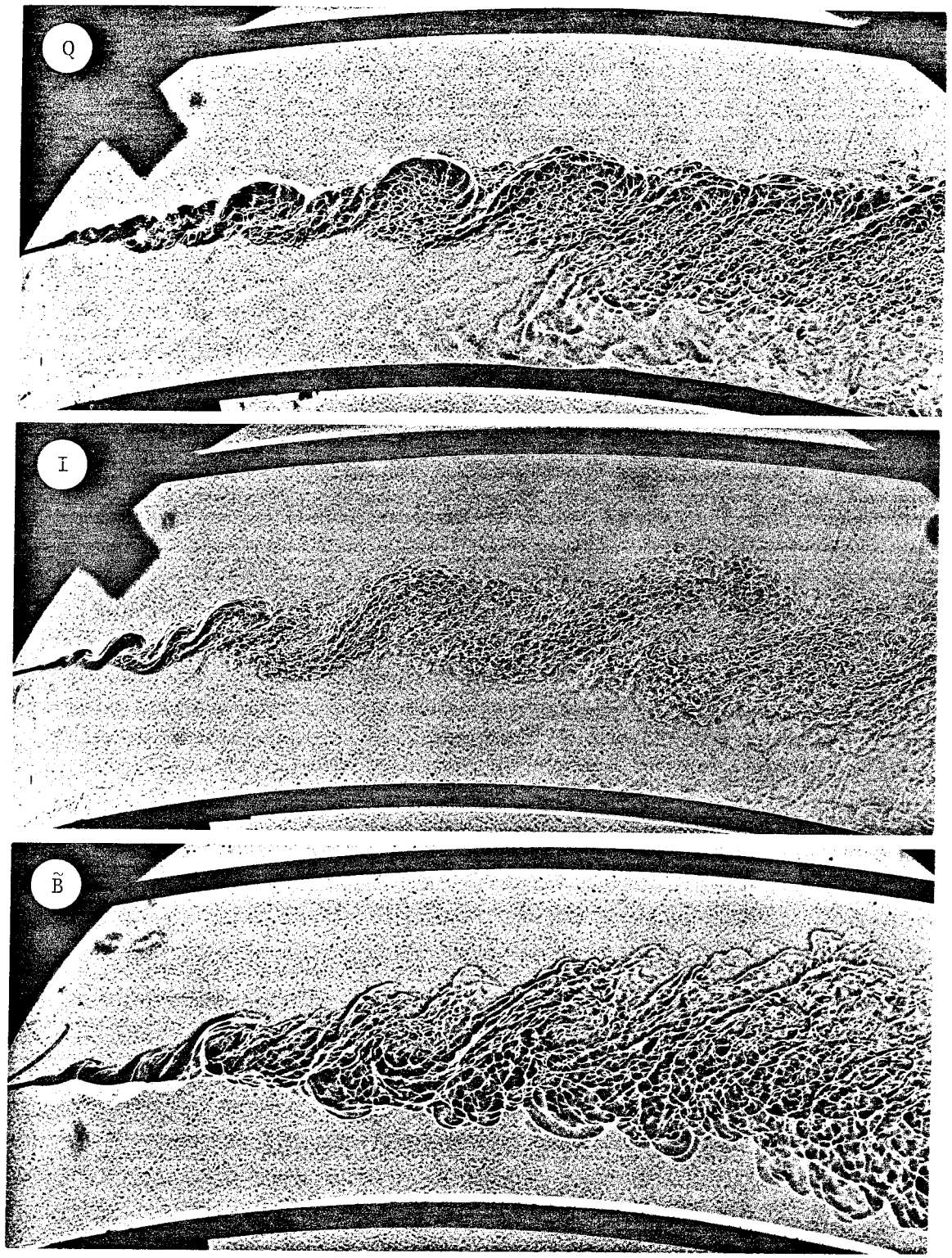

Fig. 5.1 (i) $U_o/U_i = 3.95$; $\rho_o/\rho_i = 7/1$ (top)
$\rho_o/\rho_i = 1/1$ (middle)
$\rho_o/\rho_i = 1/7$ (bottom).

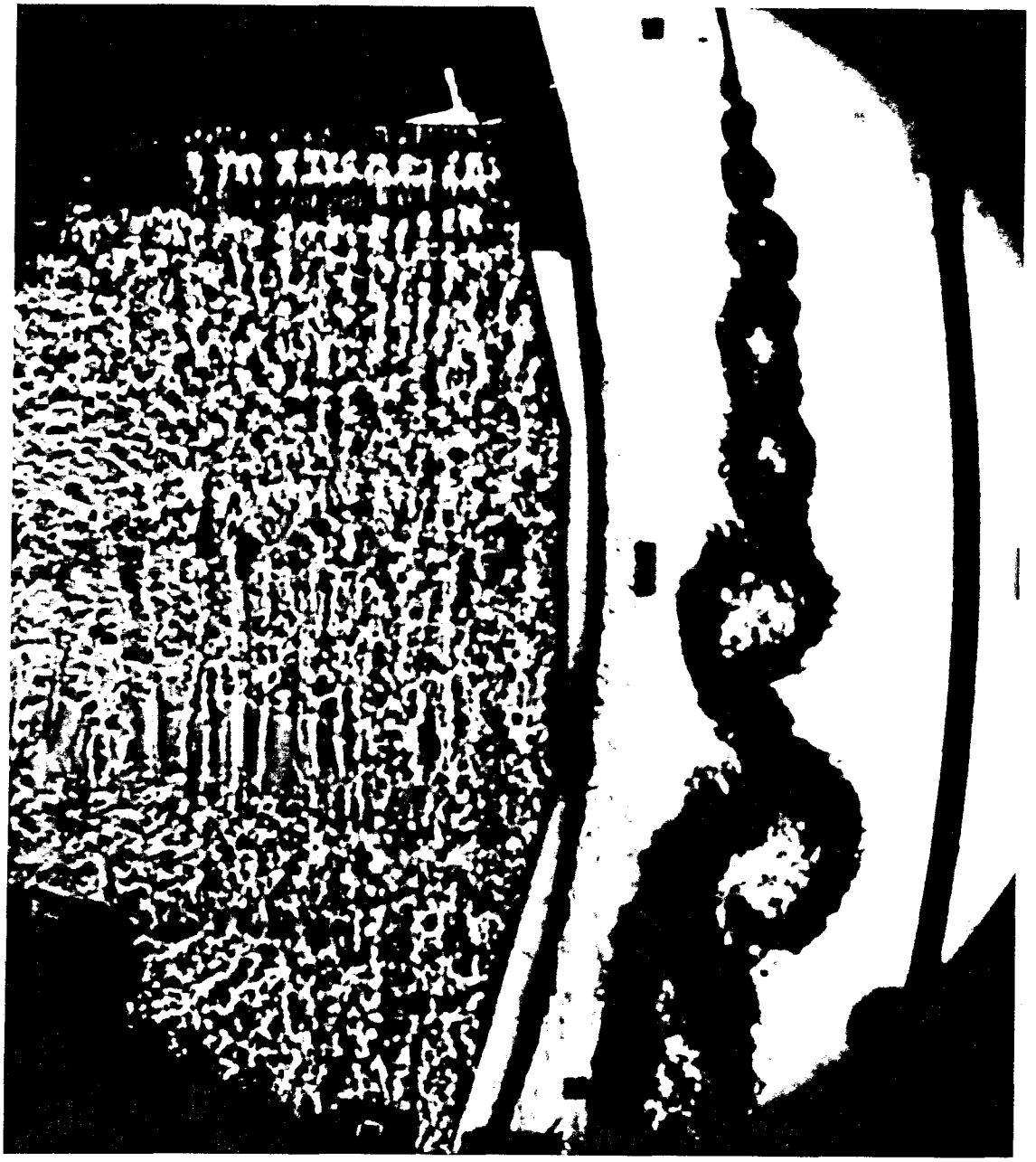

Fig. 5.2 Flow J. $U_o/U_i = 2.63$, constant density. One frame from the high-speed movie. Kelvin-Helmholtz instability is dominant.

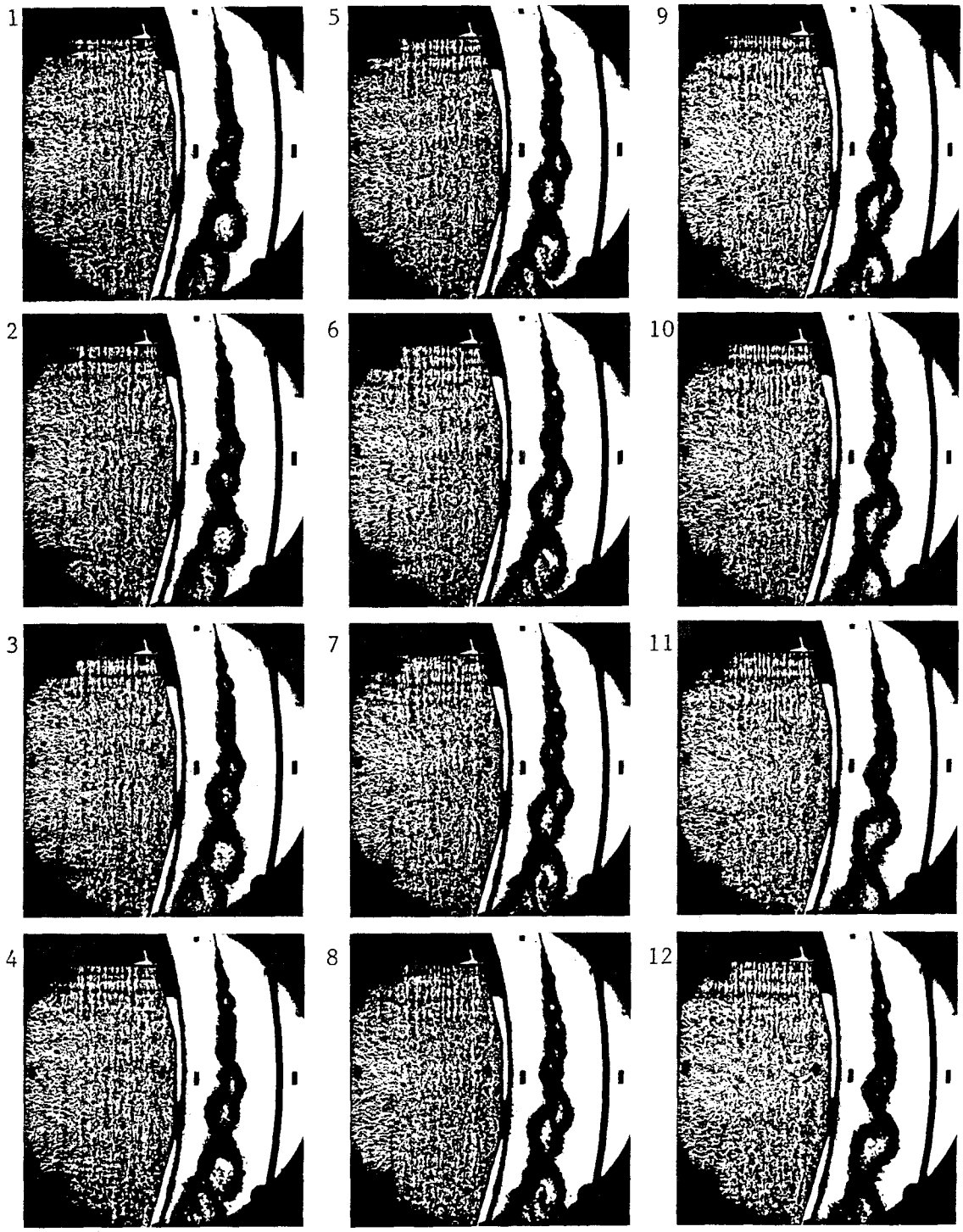

Fig. 5.3 Flow J. U_o/U_i = 2.63, constant density. A sequence of frames from the high-speed movie. Kelvin-Helmholtz instability is dominant. A pairing process is visible in frames 6 to 11.

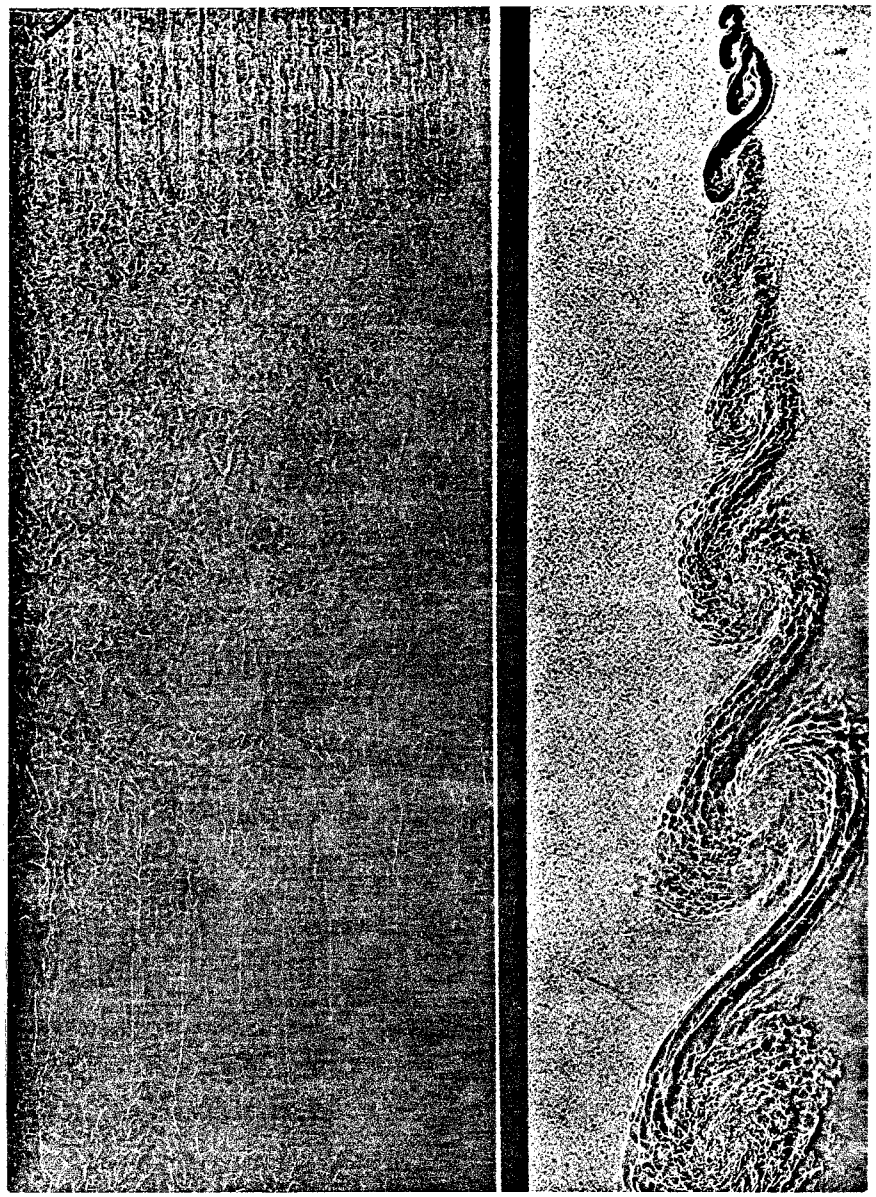

Fig. 5.4 Plane mixing layer (Konrad 1976). $U_o/U_i = 2.63$, constant density. The corresponding curved flow is J in Figs. 5.2 and 5.3.

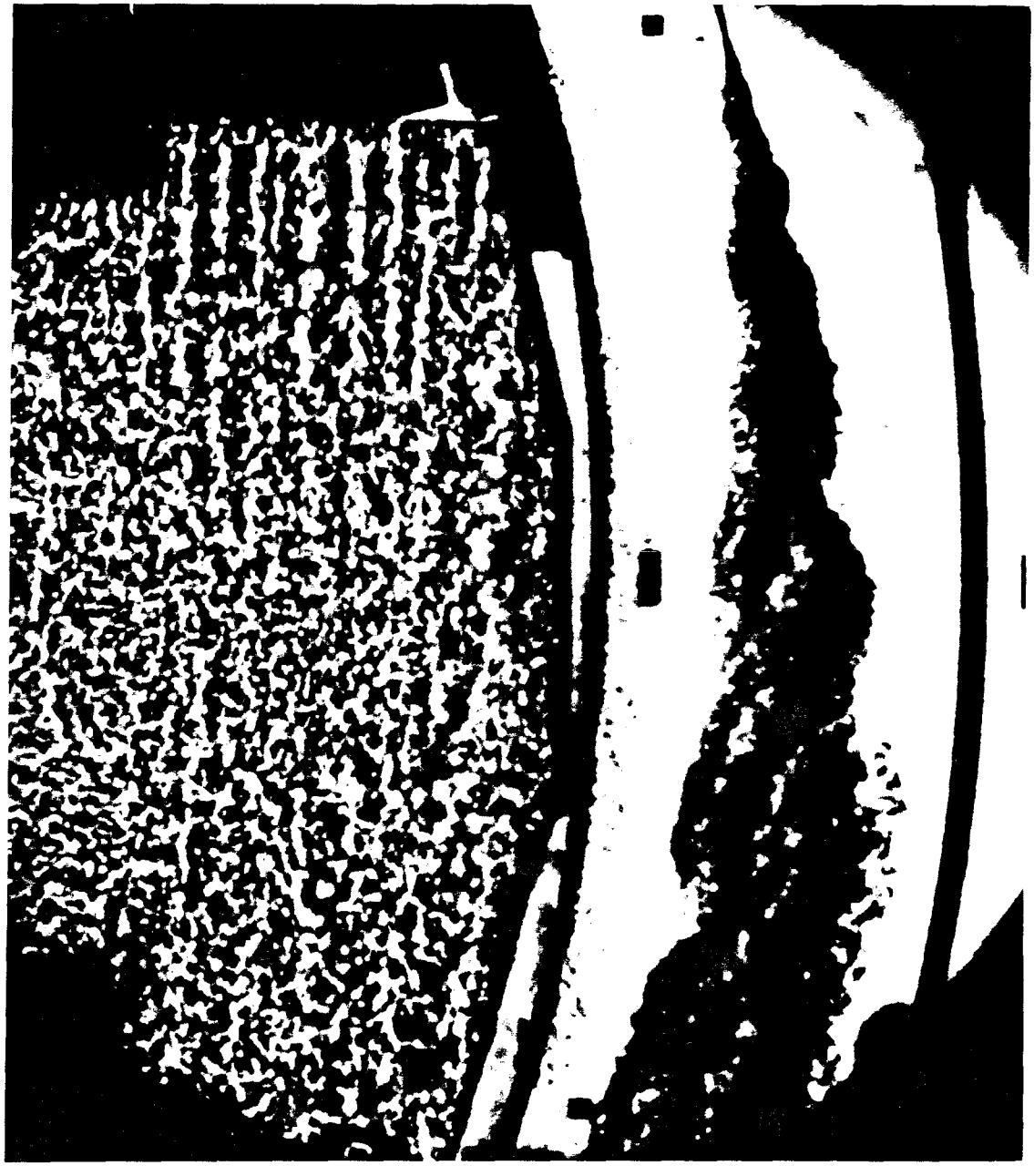

Fig. 5.5 Flow $\tilde{J}$. $U_o/U_i = 0.38$, constant density. One frame from the high-speed movie. Taylor-Görtler instability is dominant.

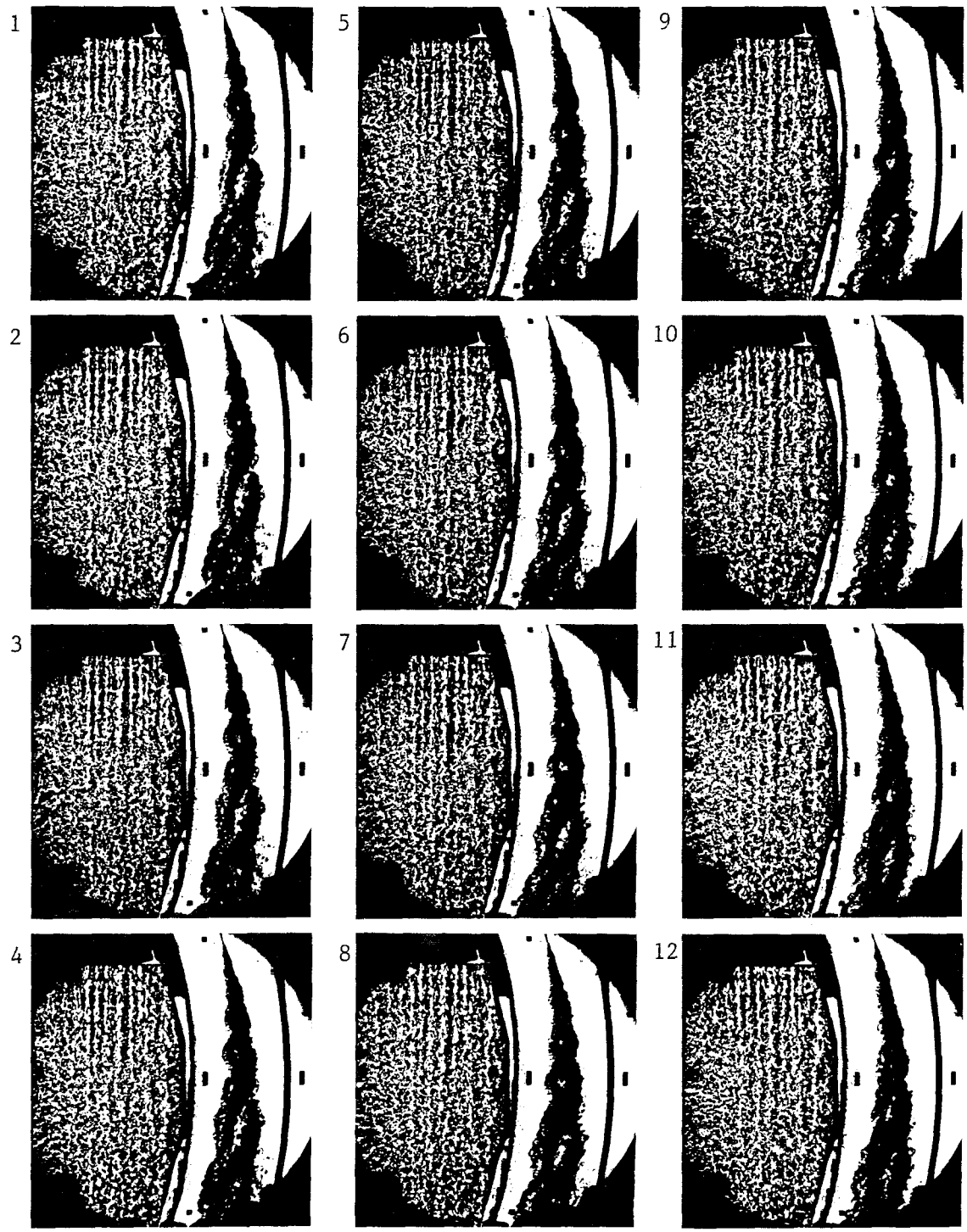

Fig. 5.6 Flow $\tilde{J}$. U_o/U_i = 0.38, constant density. A sequence of frames from the high-speed movie. Taylor-Görtler instability is important. No pairing process was observed throughout the movie for this flow.

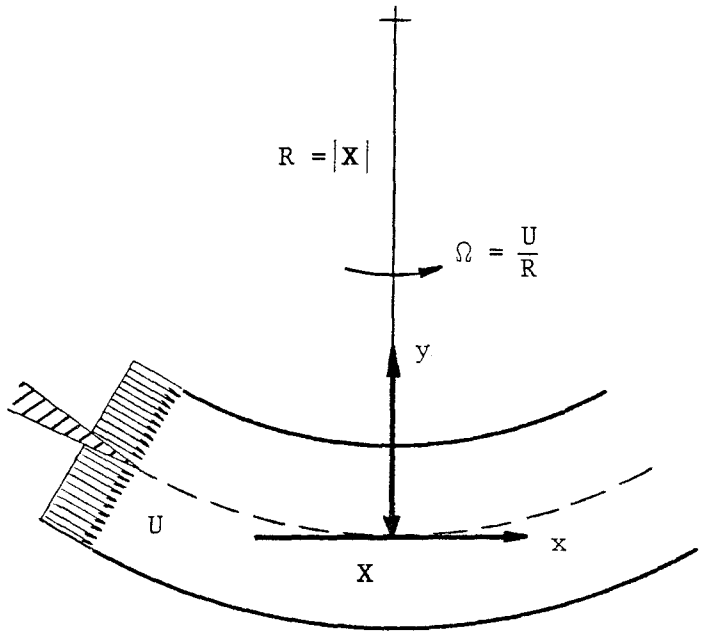

Moving coordinates

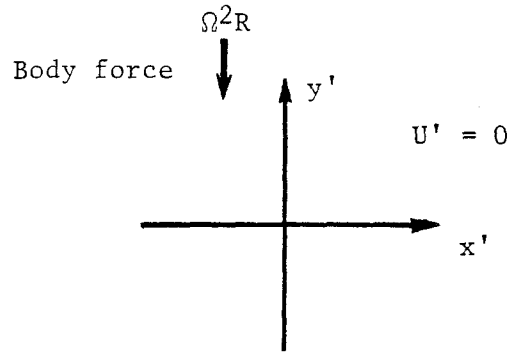

Inertial coordinates

Fig. 5.7 The body force in a moving coordinate system for two streams having equal velocities; **X** is the position vector of the origin of coordinates.

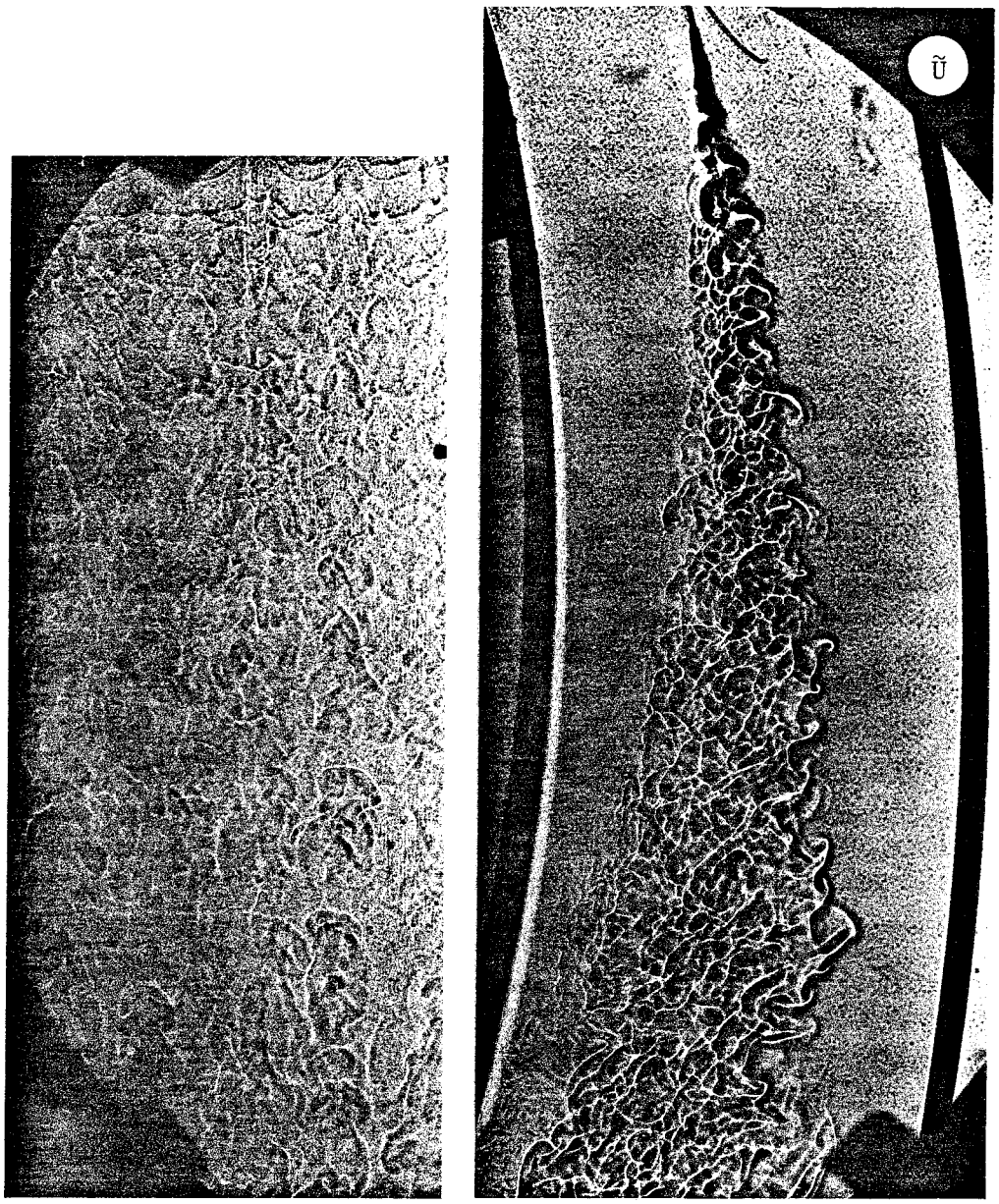

Fig. 5.8 Flow Ũ. $U_o/U_i = 1.0$, $\rho_o/\rho_i = 1/7$. Rayleigh-Taylor instability is important. In the plane view, the small scale structures appear to be well organized.

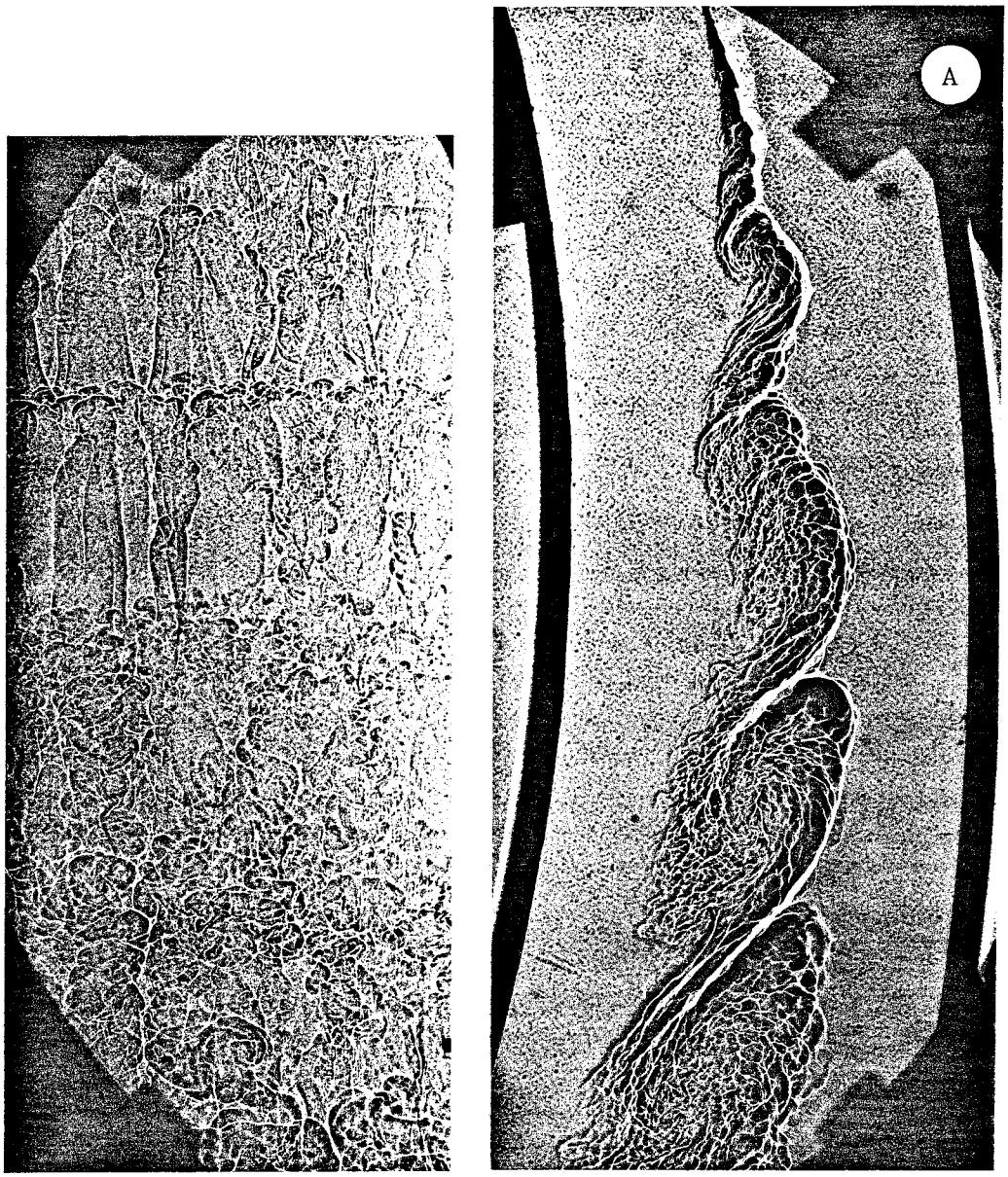

Fig. 5.9 Flow Ã. $U_o/U_i = 2.63$, $\rho_o/\rho_i = 1/7$. The flow is neutral to Taylor-Görtler instability, but Rayleigh-Taylor instability may be important. Streamwise structures have thickened the bridges between the two-dimensional vortices compared to flow A in Fig. 5.11, where the sense of the curvature is reversed.

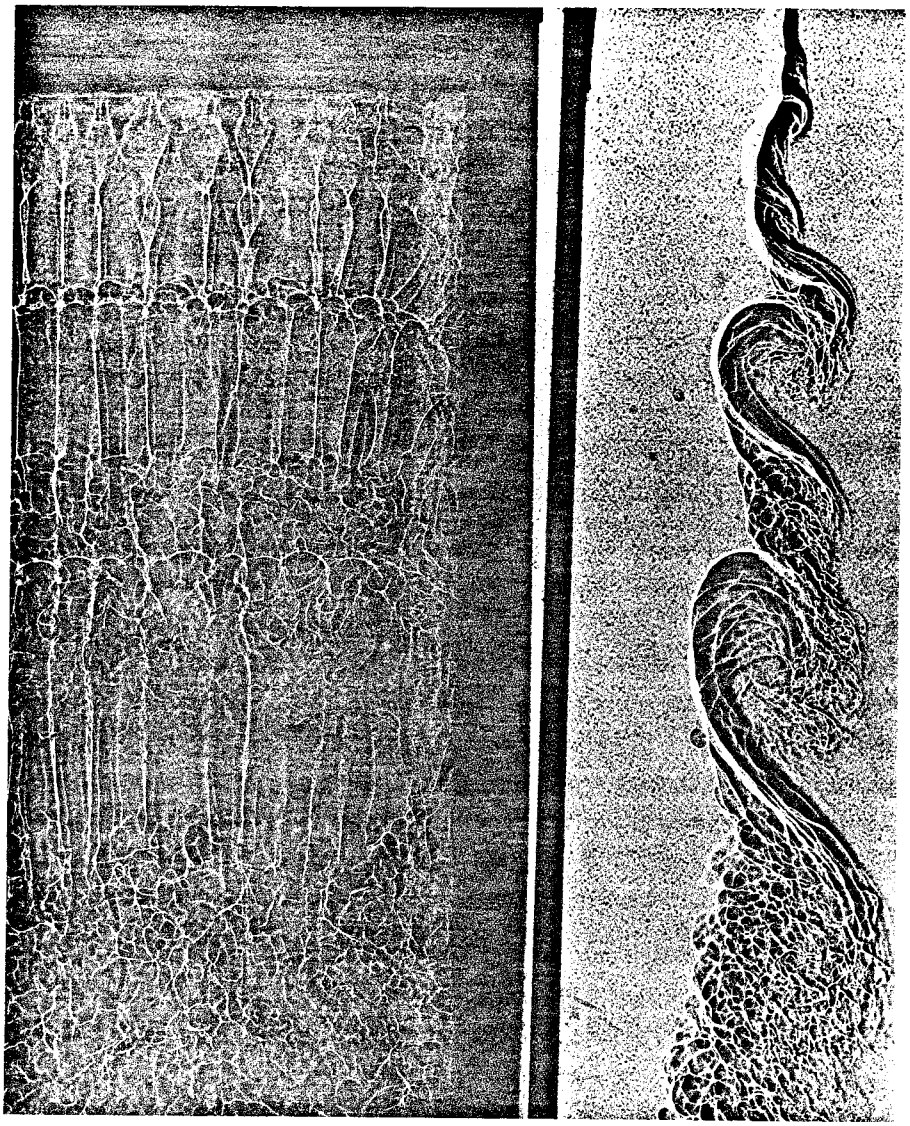

Fig. 5.10 Plane mixing layer (Konrad 1976). $U_o/U_i = 2.63$, $\rho_o/\rho_i = 1/7$. The corresponding curved flows are Ã in Fig. 5.9 and A in Fig. 5.11.

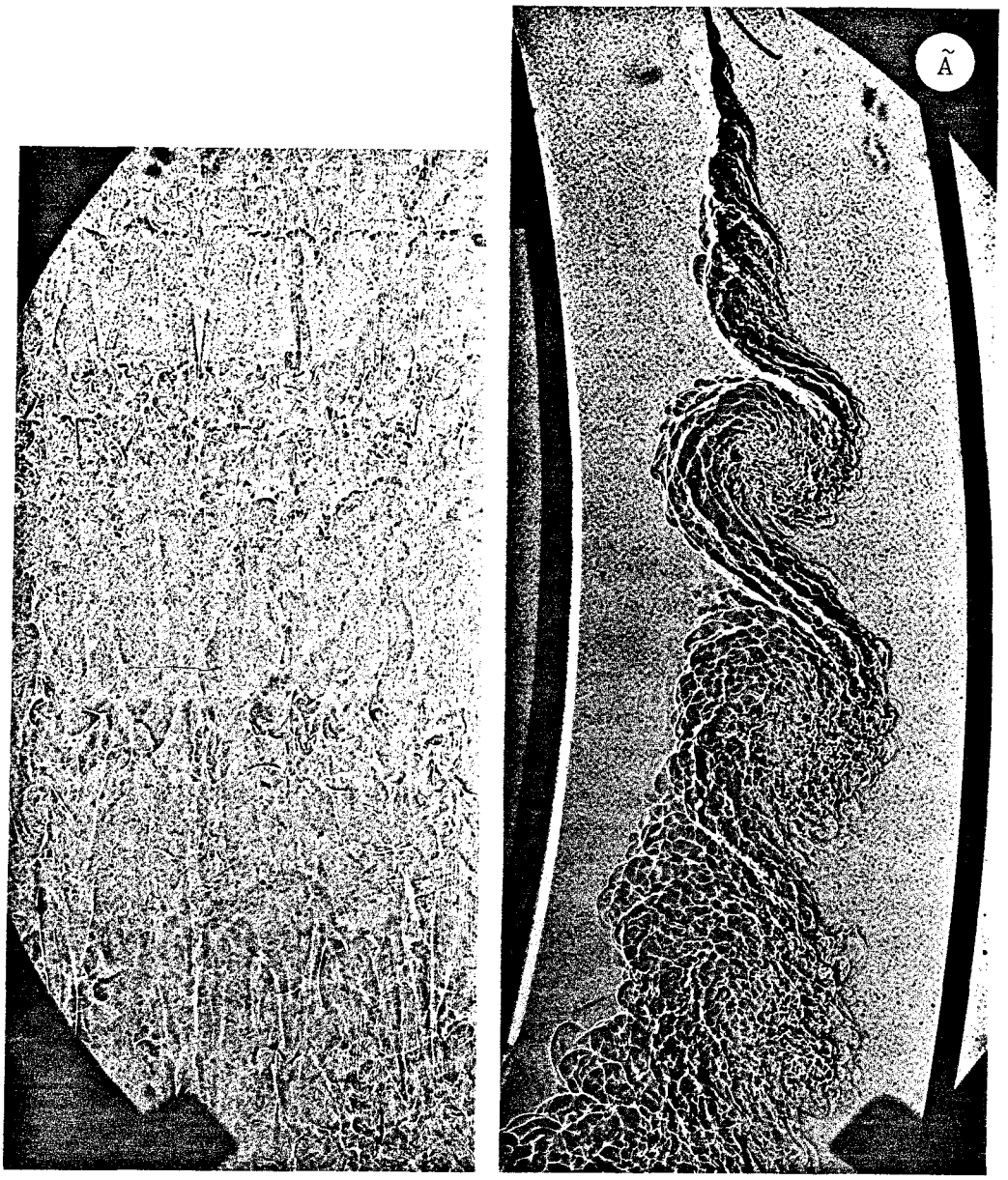

Fig. 5.11 Flow A. U_o/U_i = 0.38, ρ_o/ρ_i = 7/1. The flow is neutral to Taylor-Görtler instability; Kelvin-Helmholtz instability is dominant. The contrast is poor for the streamwise structures in the plan view compared to flow Ã in Fig. 5.9, suggesting that the amplitude of these disturbances may be smaller.

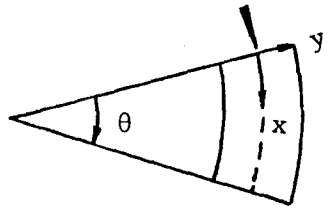

Symbols:

- · virtual origin according to concentration profile
- · virtual origin according to ur profile
- ⅄ 10 percent boundary
- Y 90 percent boundary
- △ data for θ = 10°
- □ data for θ = 15°
- \+ data for θ = 20°
- × data for θ = 25°

$$\bar{y} = \frac{y-y_v}{x-x_v}$$

$$\Gamma = \frac{(ur)-(ur)_{min}}{(ur)_{max}-(ur)_{min}}$$

c_{He} = molar concentration of helium

x_v = x-coordinate of virtual origin

y_v = y-coordinate of virtual origin

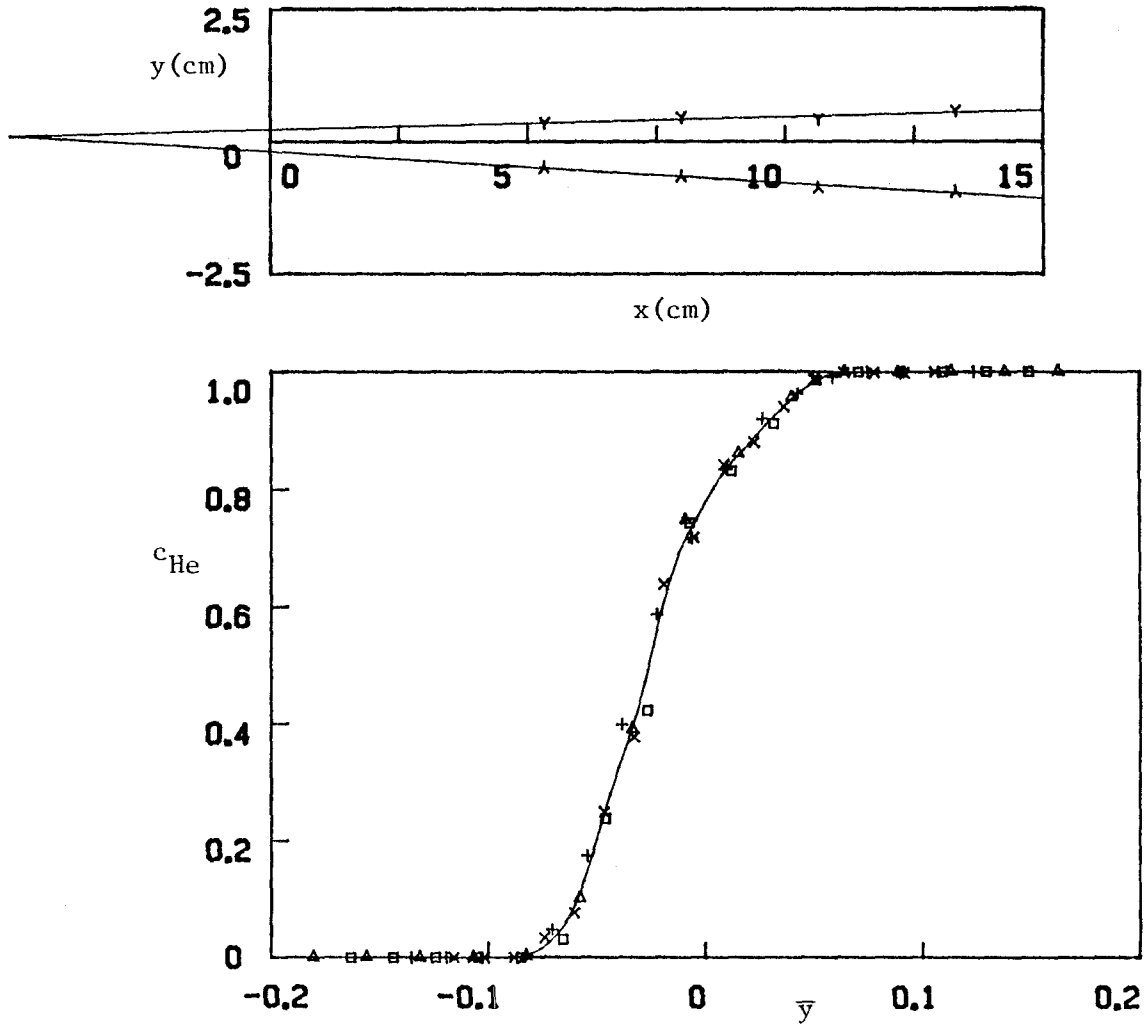

Fig. 6.1 Flow Ã. U_o/U_i = 2.63, ρ_o/ρ_i = 1/7. Profiles of helium concentration. The flow is neutral to Taylor-Görtler instability, but Rayleigh-Taylor instability may be important. The virtual origin in this figure is determined according to profiles of concentration.

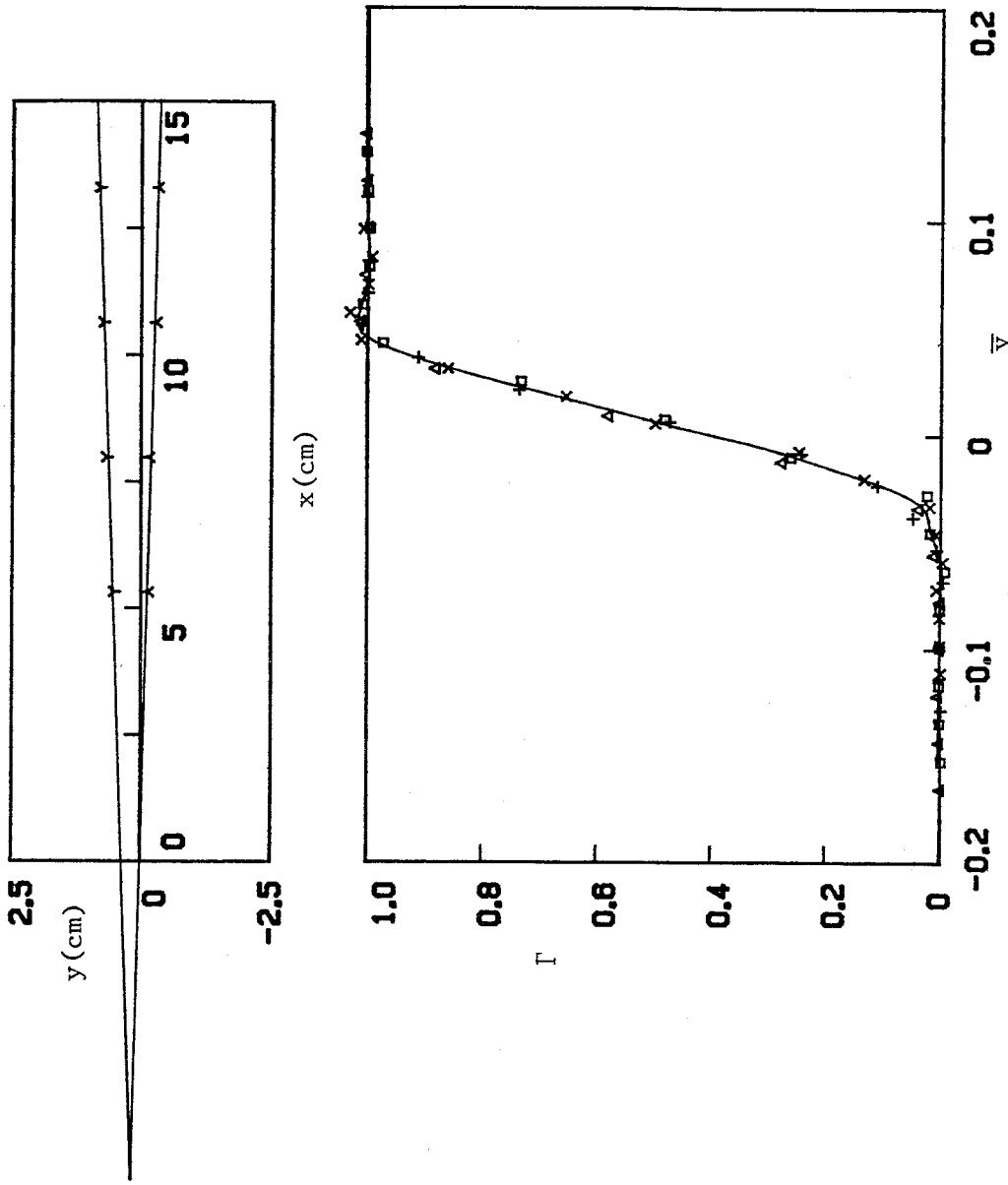

Fig. 6.2 Flow Ã. U_o/U_i = 2.63, ρ_o/ρ_i = 1/7. Profiles of circulation ur. The flow is neutral to Taylor-Görtler instability, but Rayleigh-Taylor instability may be important. The virtual origin in this figure is determined according to ur profiles. For legend, see Fig. 6.1.

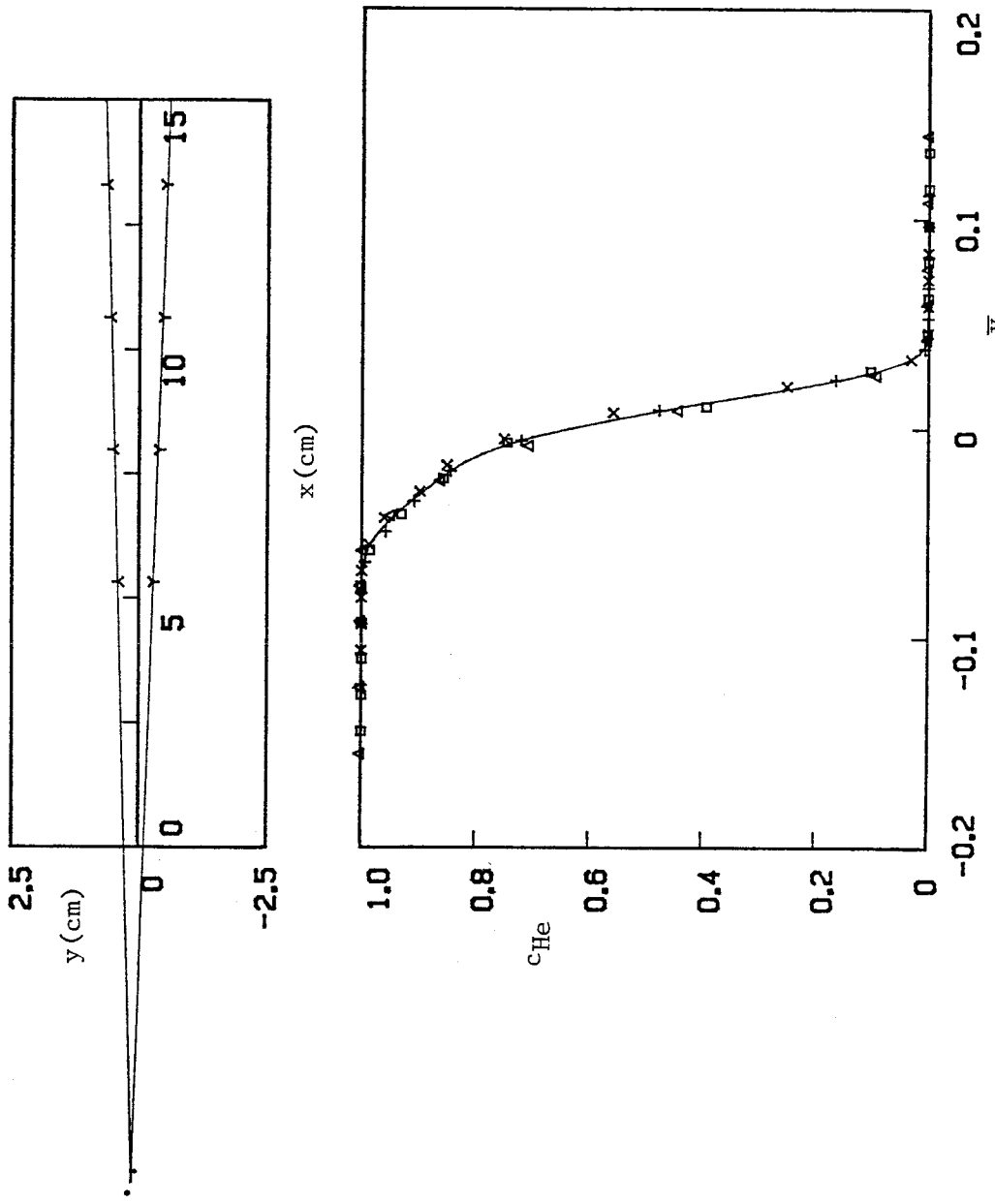

Fig. 6.3 (a) Flow A. $U_o/U_i = 0.38$, $\rho_o/\rho_i = 7/1$. Profiles of helium concentration. The flow is neutral to Taylor-Görtler instability. For legend, see Fig. 6.1.

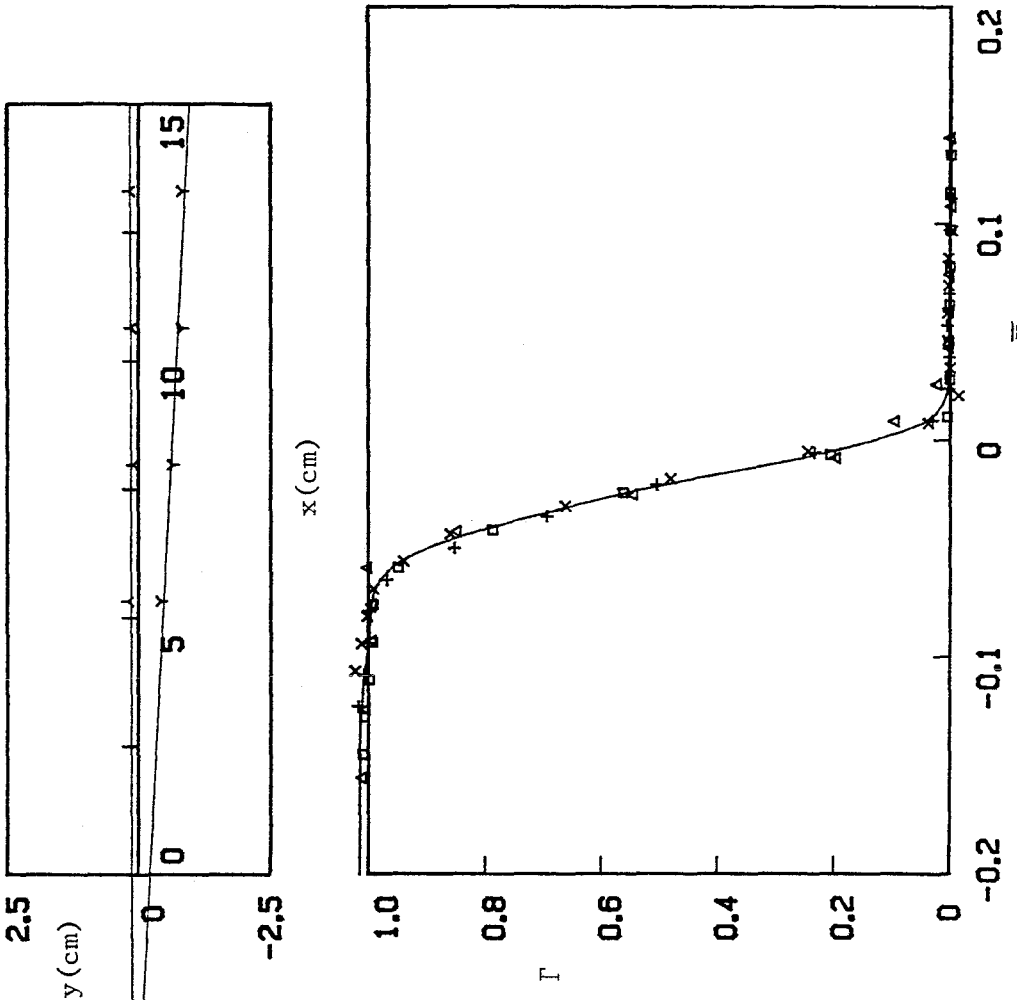

Fig. 6.3 (b) Flow A. $U_o/U_i = 0.38$, $\rho_o/\rho_i = 7/1$. Profiles of circulation ur. The flow is neutral to Taylor-Görtler instability. For legend, see Fig. 6.1.

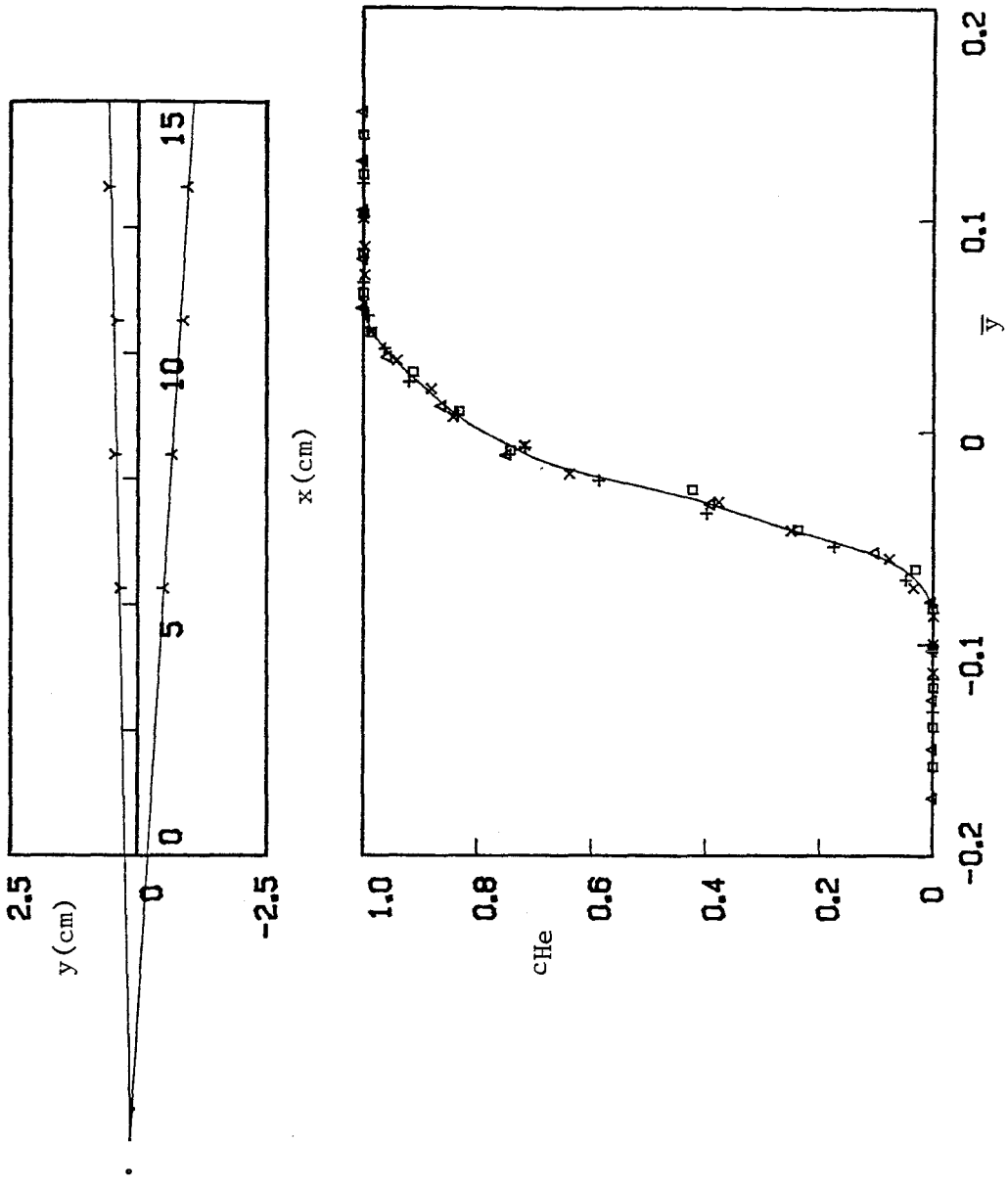

Fig. 6.4 (a) Flow Ã. $U_o/U_i = 2.63$, $\rho_o/\rho_i = 1/7$. Profiles of helium concentration. The flow is neutral to Taylor-Görtler instability, but Rayleigh-Taylor instability may be important. For legend, see Fig. 6.1.

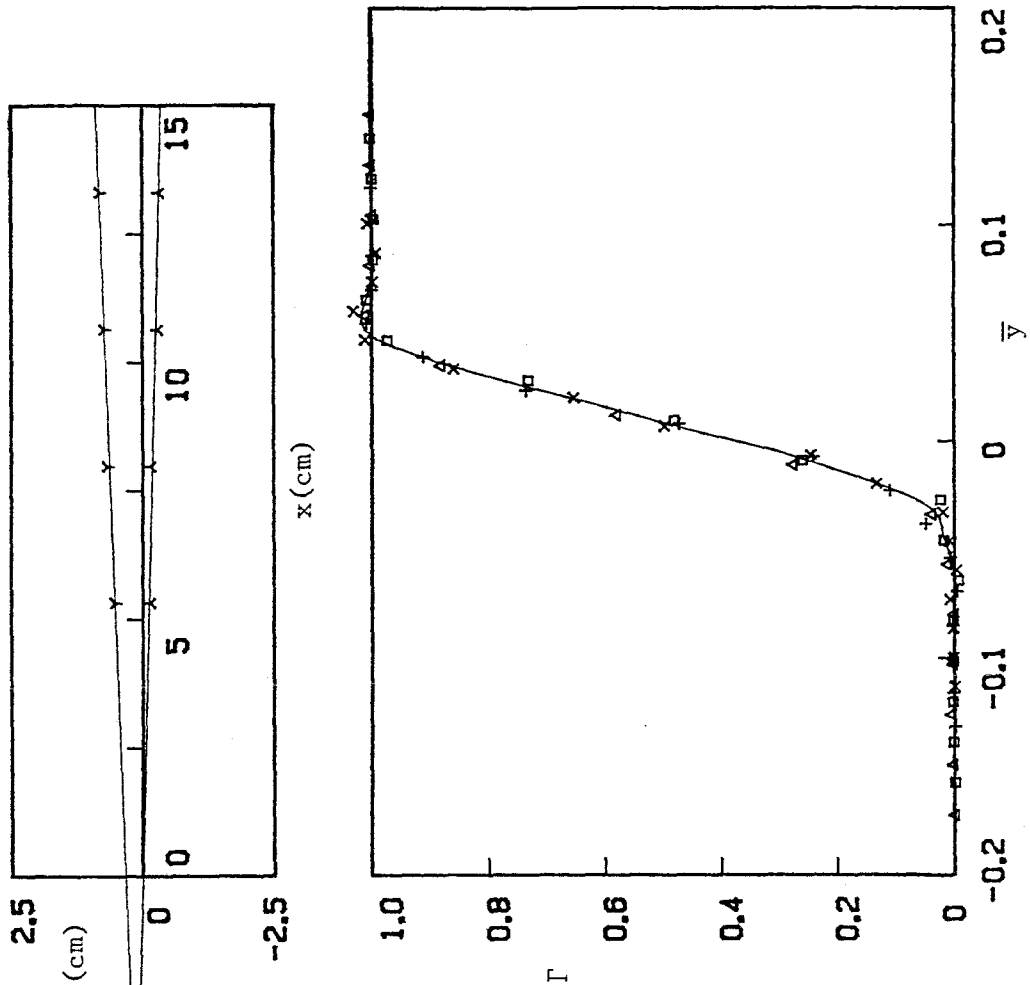

Fig. 6.4 (b) Flow Ã. U_o/U_i = 2.63, ρ_o/ρ_i = 1/7. Profiles of circulation ur. The flow is neutral to Taylor-Görtler instability, but Rayleigh-Taylor instability may be important. For legend, see Fig. 6.1.

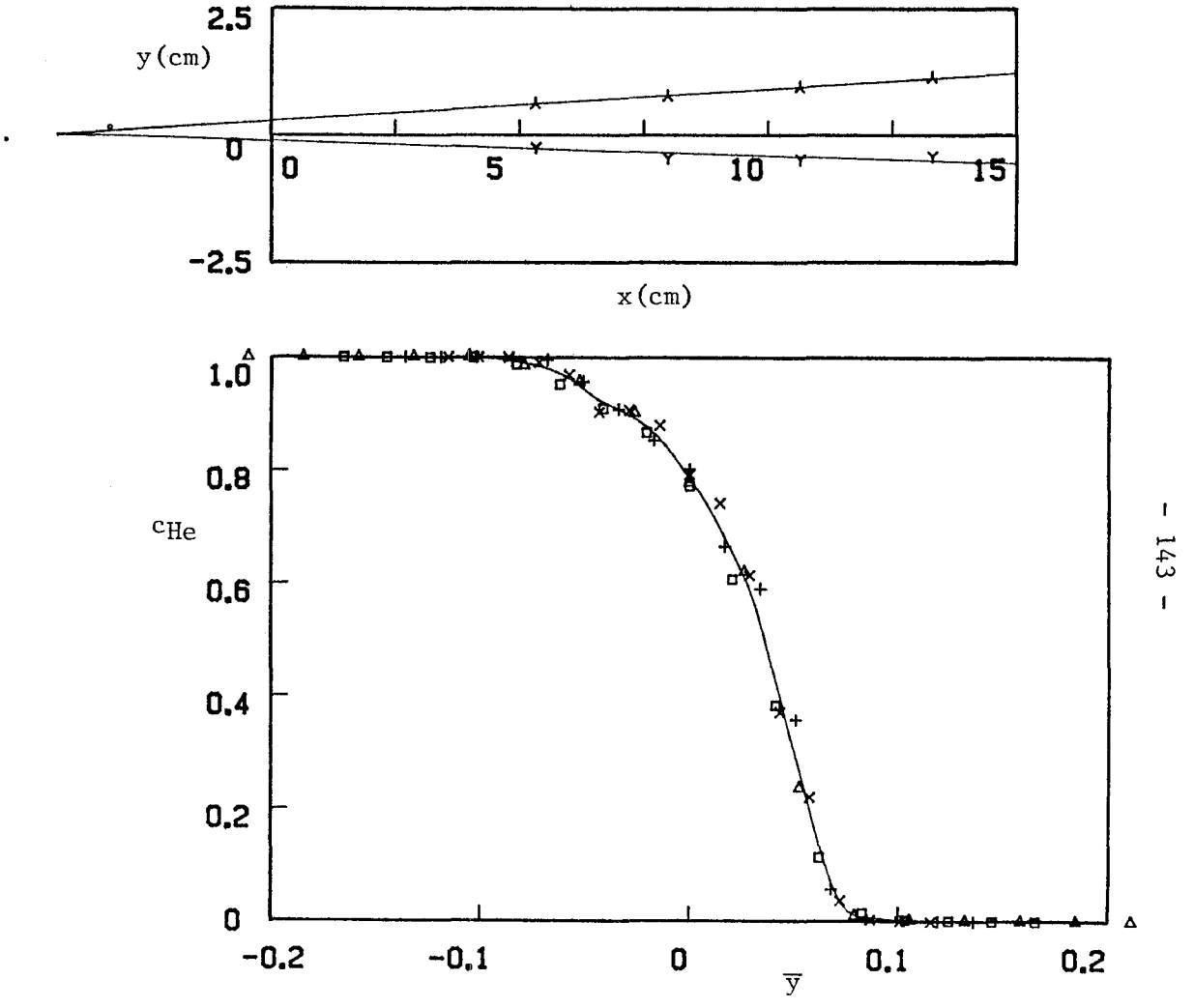

Fig. 6.5 (a) Flow B. $U_o/U_i = 0.25$, $\rho_o/\rho_i = 7/1$. Profiles of helium concentration. Weak Taylor-Görtler instability may be present. For legend, see Fig. 6.1.

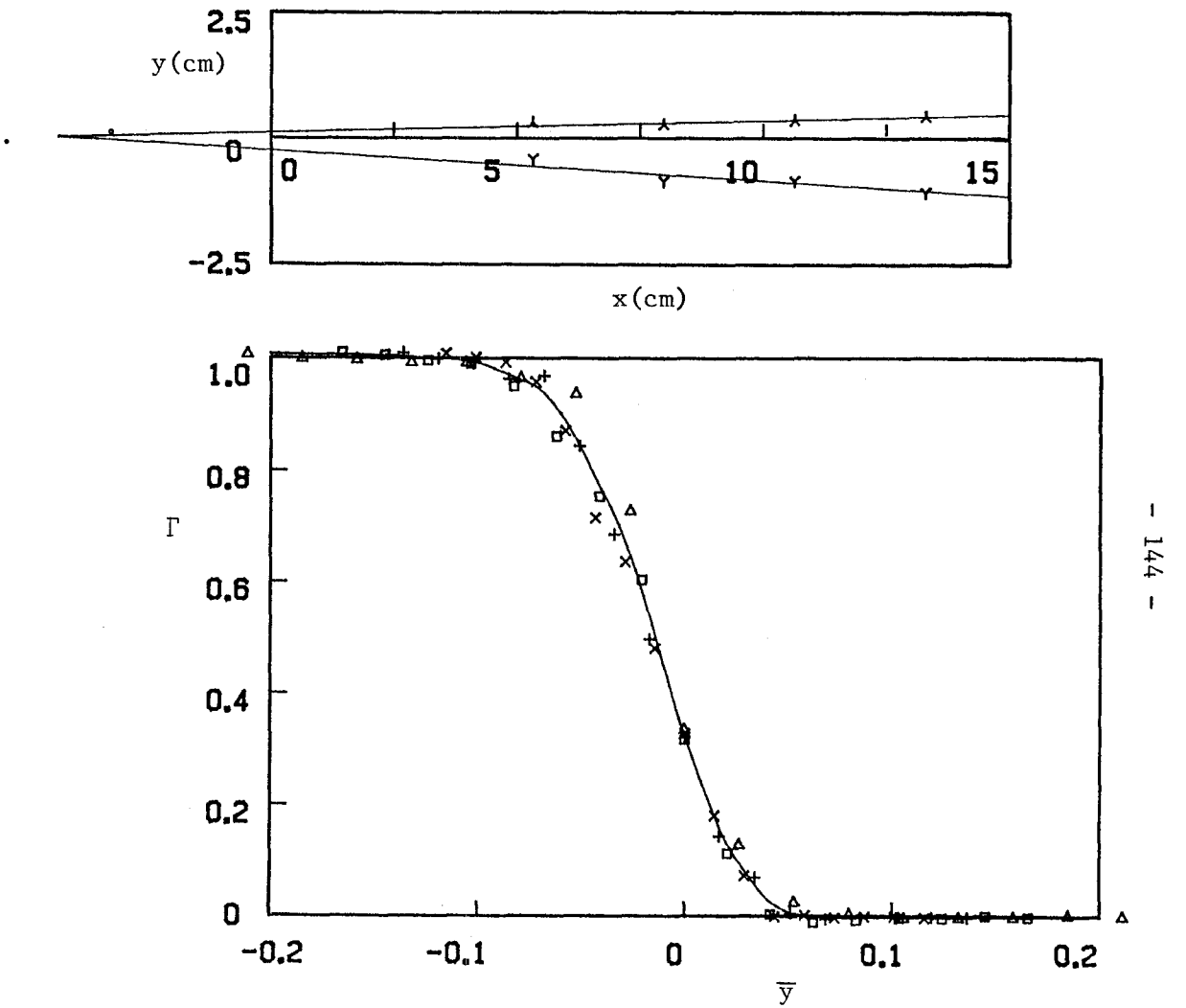

Fig. 6.5 (b) Flow B. U_o/U_i = 0.25, ρ_o/ρ_i = 7/1. Profiles of circulation ur. Weak Taylor-Görtler instability may be present. For legend, see Fig. 6.1.

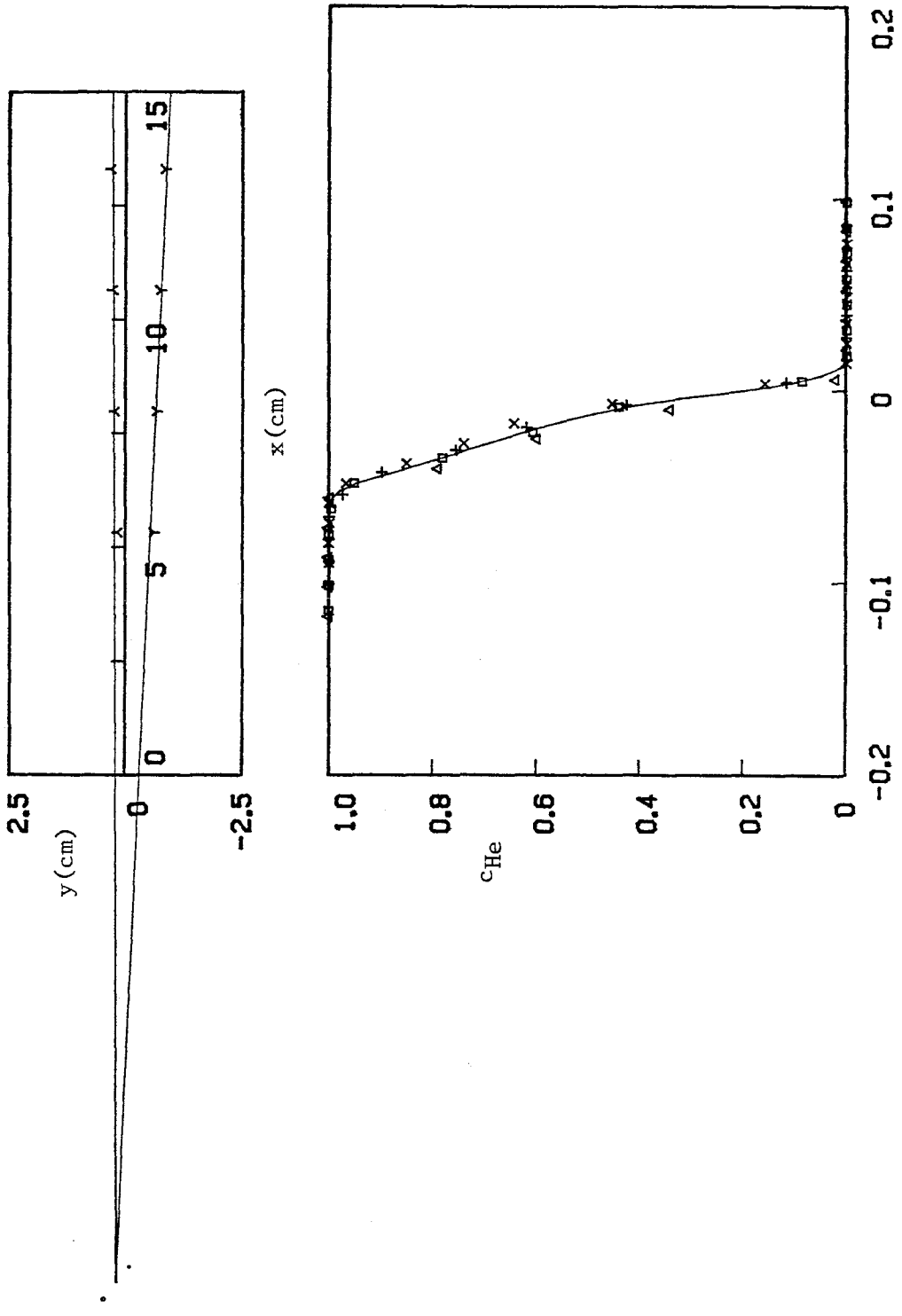

Fig. 6.6 (a) Flow P. U_o/U_i = 2.63, ρ_o/ρ_i = 7/1. Profiles of helium concentration. The flow is very stable. For legend, see Fig. 6.1.

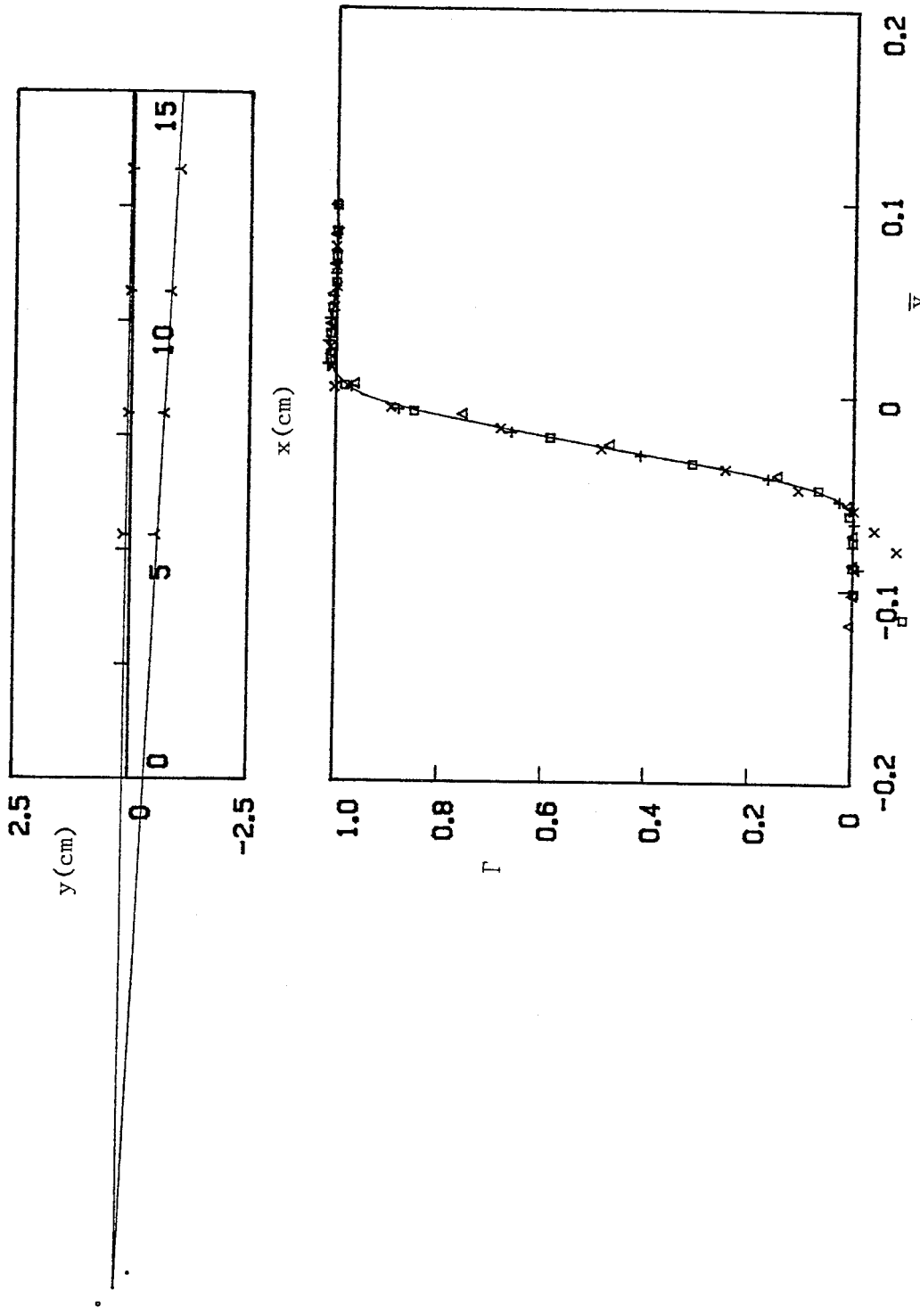

Fig. 6.6 (b) Flow P. $U_o/U_i = 2.63$, $\rho_o/\rho_i = 7/1$. Profiles of circulation ur. The flow is very stable. For legend, see Fig. 6.1.

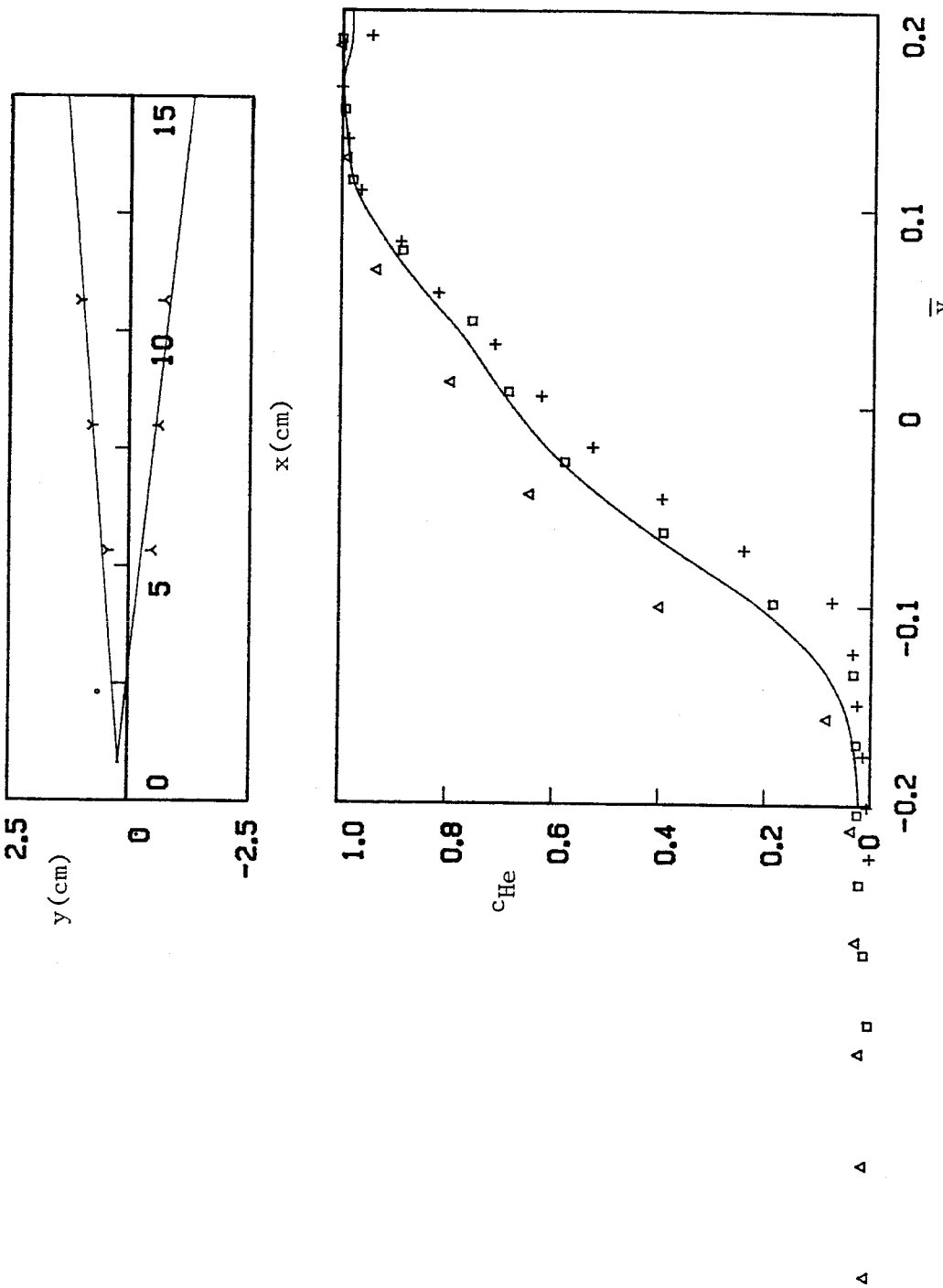

Fig. 6.7 (a) Flow $\tilde{P}$. $U_o/U_i = 0.38$, $\rho_o/\rho_i = 1/7$. Profiles of helium concentration. Both Taylor-Görtler instability and Rayleigh-Taylor instability are important. For legend, see Fig. 6.1.

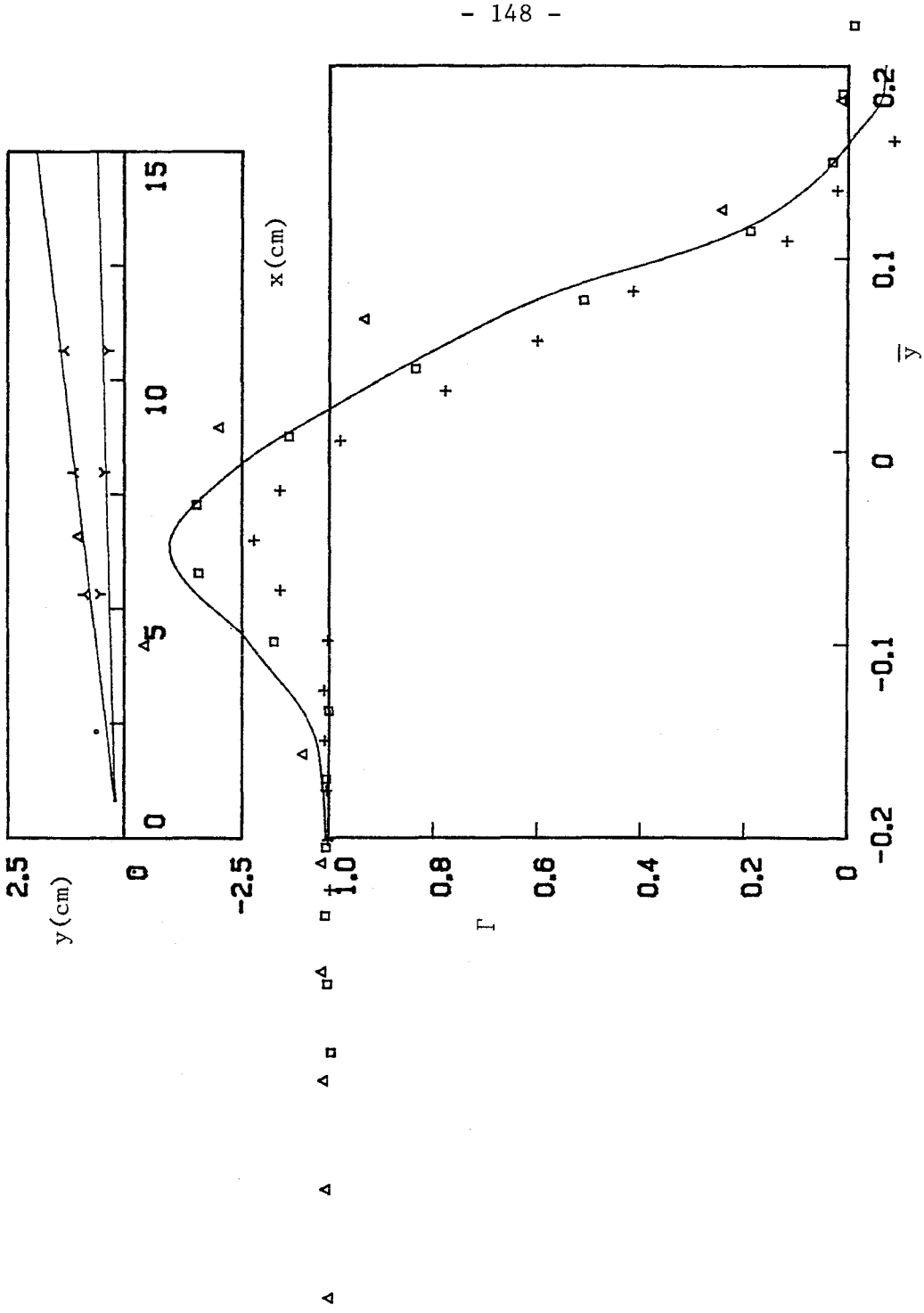

Fig. 6.7 (b) Flow $\tilde{P}$. $U_o/U_i = 0.38$, $\rho_o/\rho_i = 1/7$. Profiles of circulation ur. Both Taylor-Görtler instability and Rayleigh-Taylor instability are important. For legend, see Fig. 6.1.

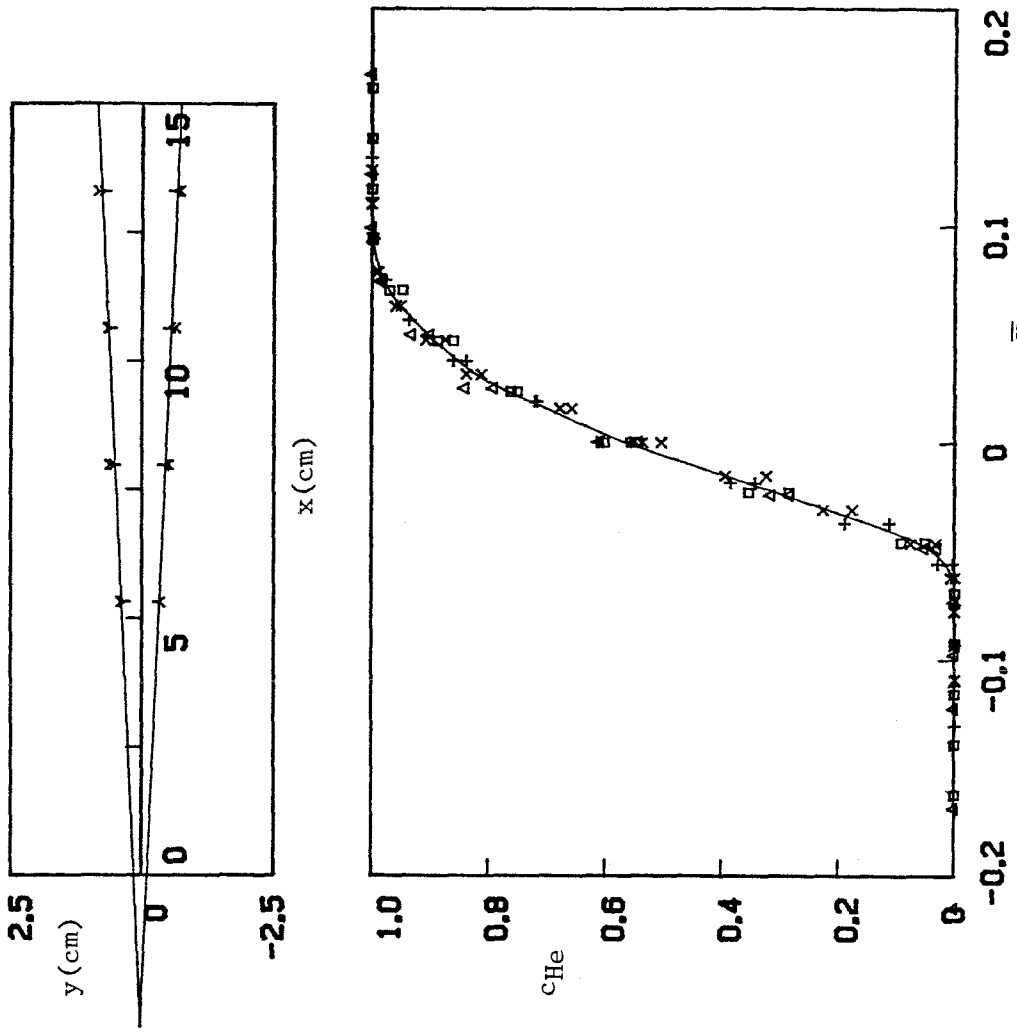

Fig. 6.8 Flow $\tilde{U}$. $U_o/U_i = 1.00$, $\rho_o/\rho_i = 1/7$. Profiles of helium concentration. Rayleigh- Taylor instability is important. For legend, see Fig. 6.1.

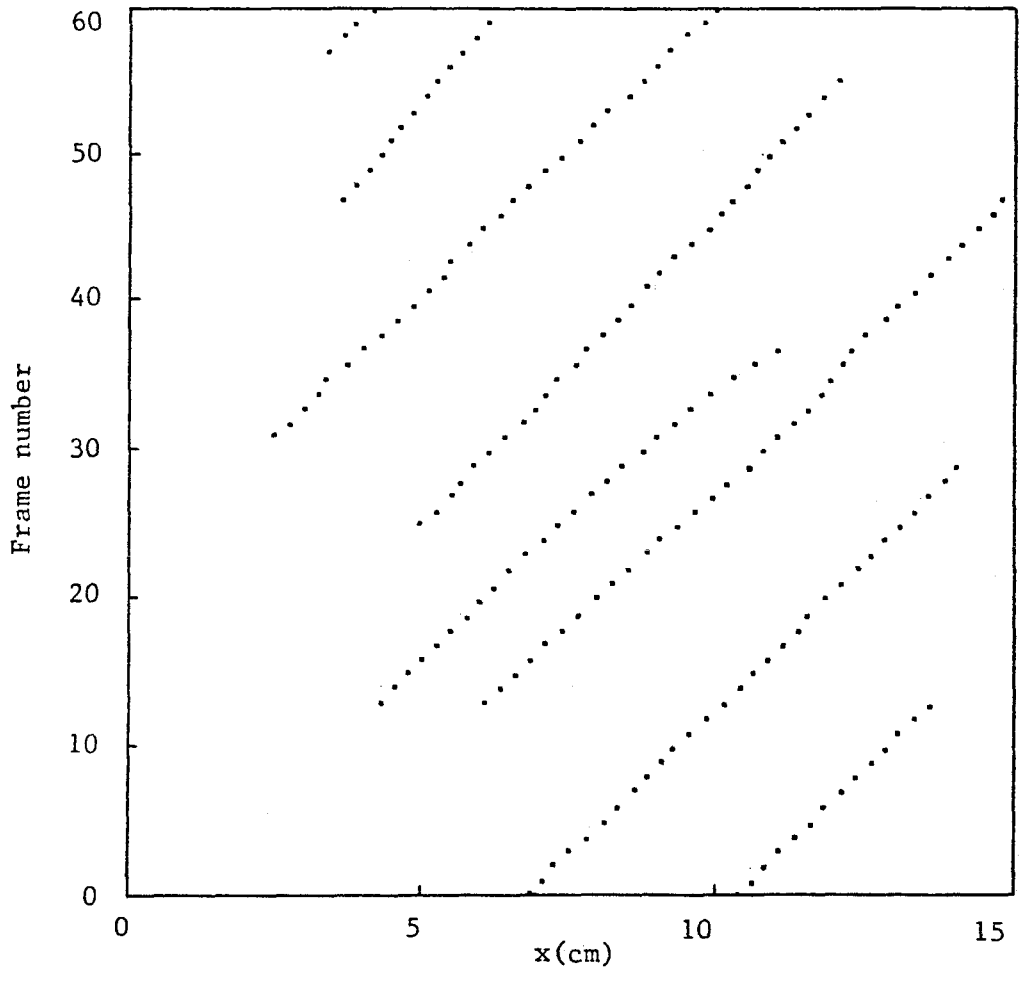

Fig. 7.1 Flow A. U_o/U_i = 380/1000, ρ_o/ρ_i = 7/1. Sample record of the trajectories for the trailing edges of vortices, taken from high-speed movies. A pairing process can be seen in frames 30 to 40 at about x = 12 cm.

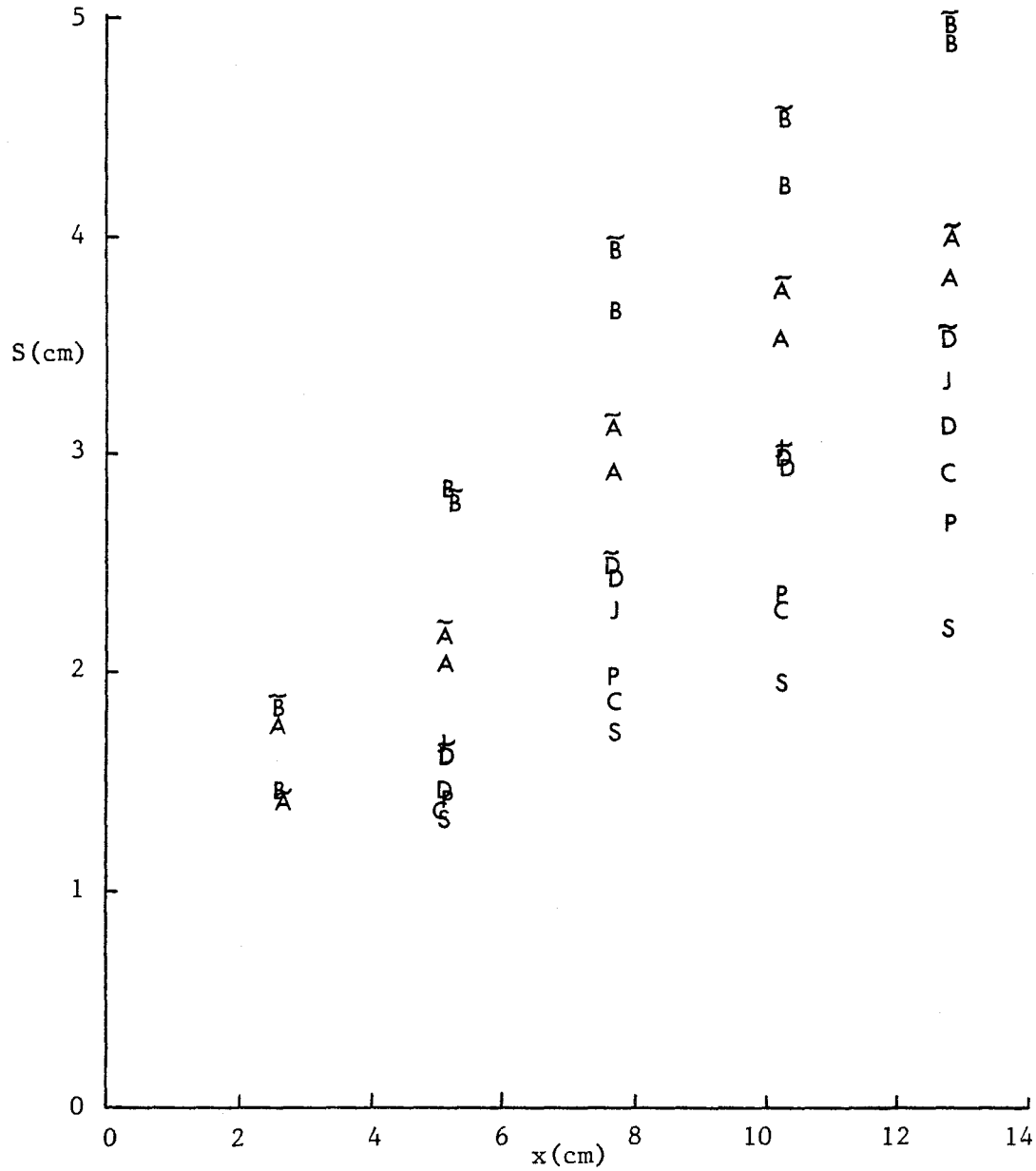

Fig. 7.2 The spacing S between spanwise vortices as a function of the downstream distance x. The data from each flow are identified by the corresponding capital letter.

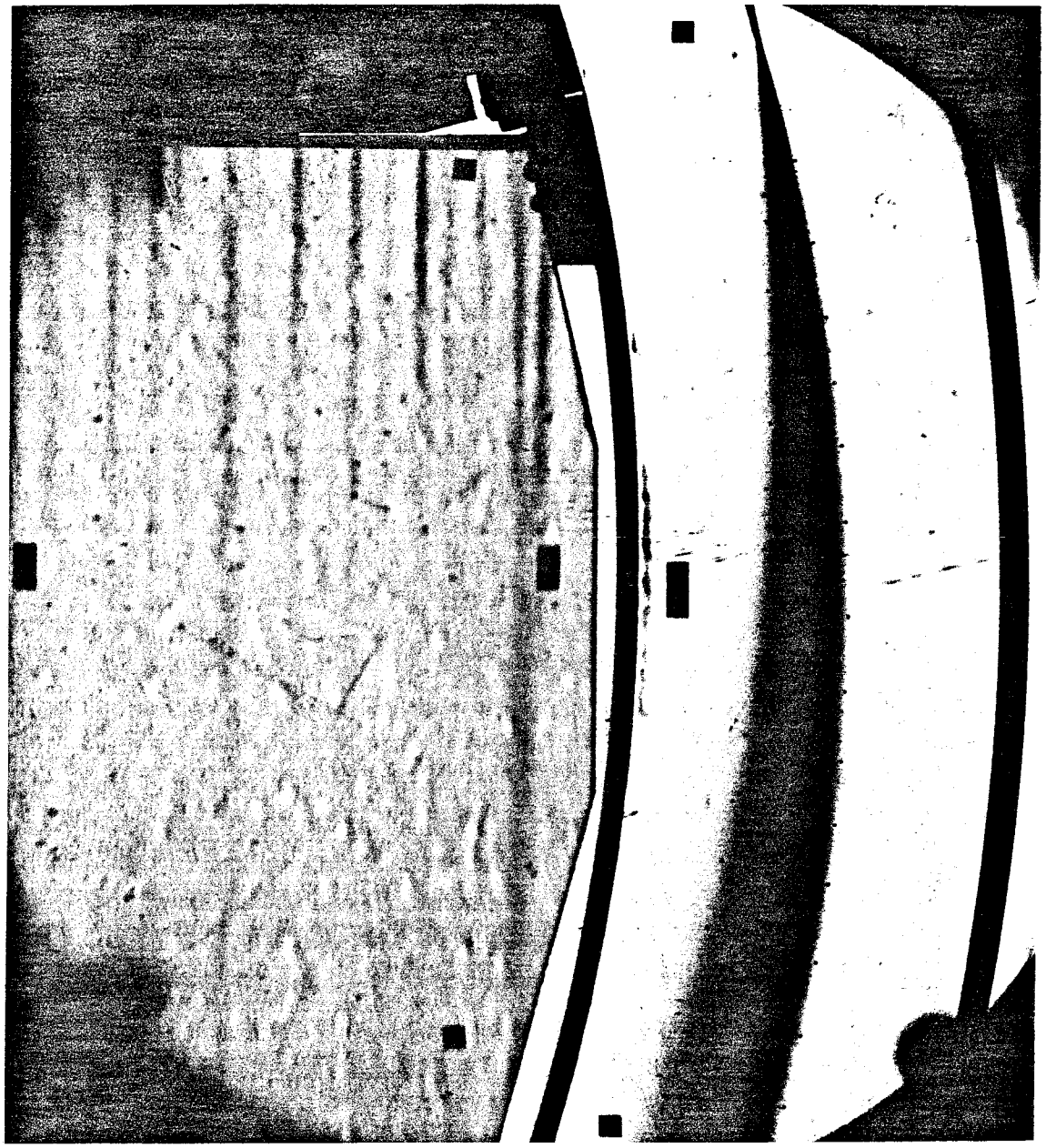

Fig. 7.3 Flow P. $U_o/U_i = 2.63$, $\rho_o/\rho_i = 7/1$. Long-time-exposure schlieren photograph (1 sec). This flow is very stable. The small dots on the edges of the mixing layer are placed by inspection and are used for defining the visual thickness.

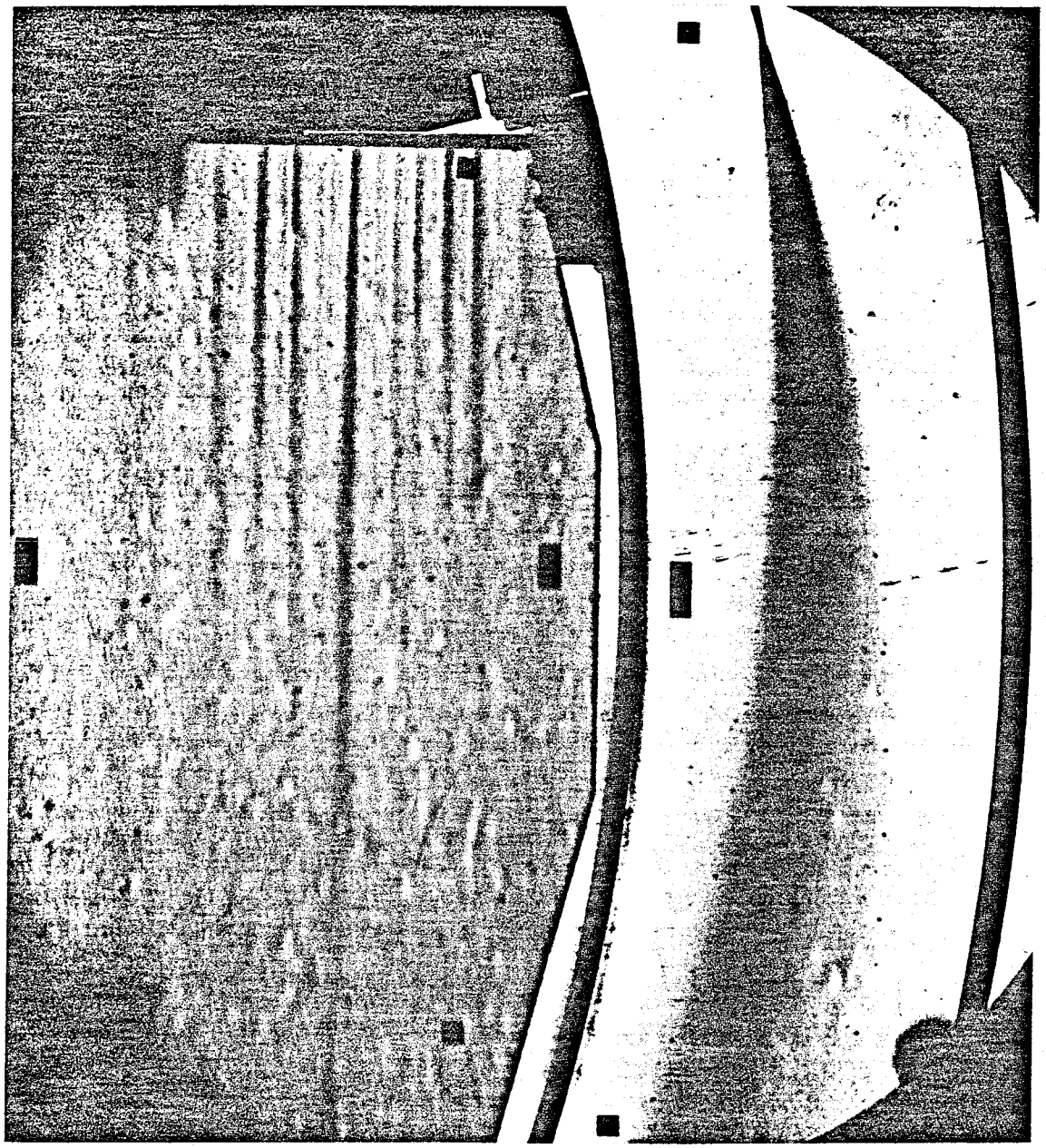

Fig. 7.4 Flow $\tilde{D}$. $U_o/U_i = 2.00$, $\rho_o/\rho_i = 1/7$. Long-time-exposure schlieren photograph (1 sec). Both Taylor-Görtler instability and Rayleigh-Taylor instability may be important. The outer boundary of the mixing layer is difficult to define accurately.

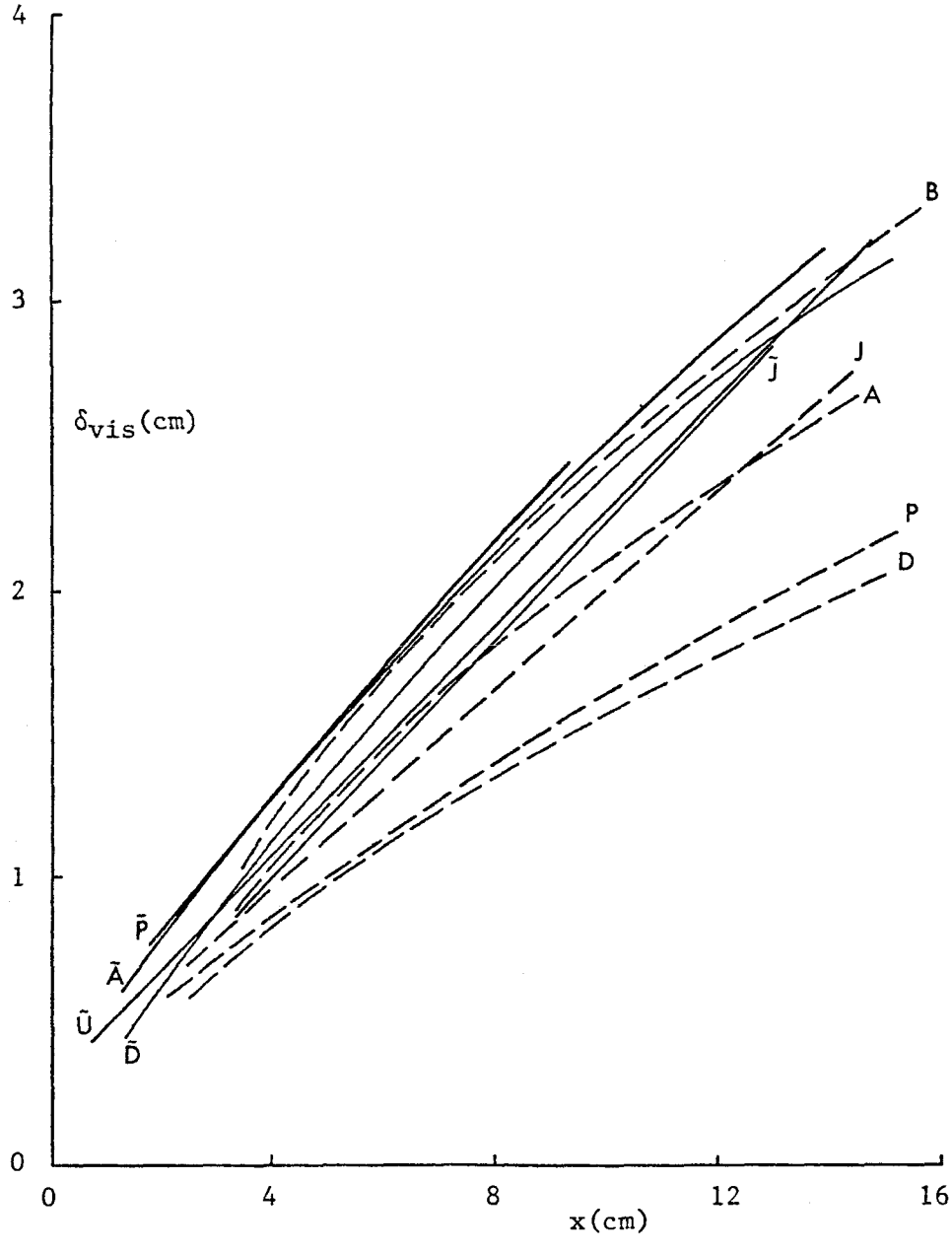

Fig. 7.5 The visual thickness δ_{vis} as a function of the downstream distance x for various curved mixing layers.

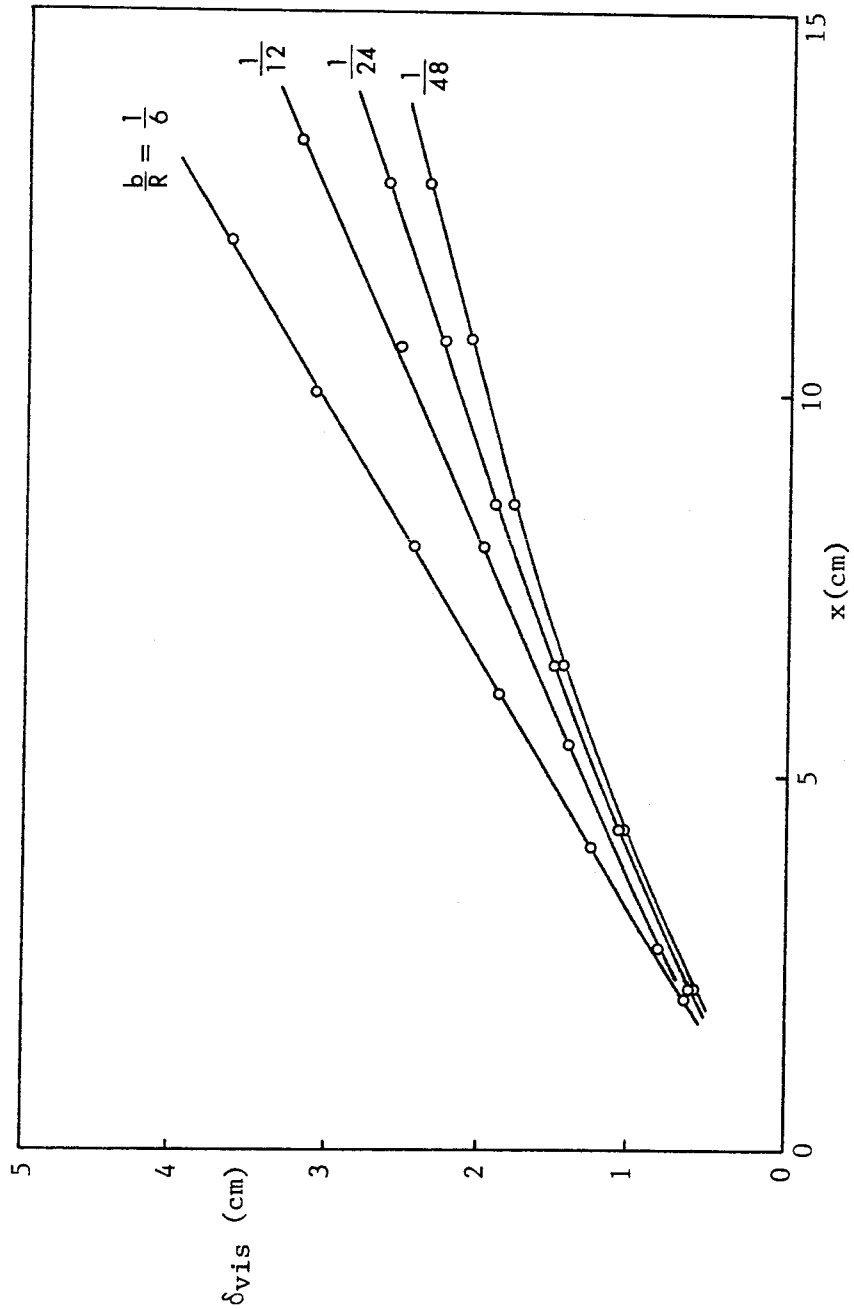

Fig. 7.6 $U_o/U_i = 1.0$, $\rho_o/\rho_i = 1/7$. The visual thickness of a heterogeneous wake/mixing layer as a function of the distance x for different curvatures.

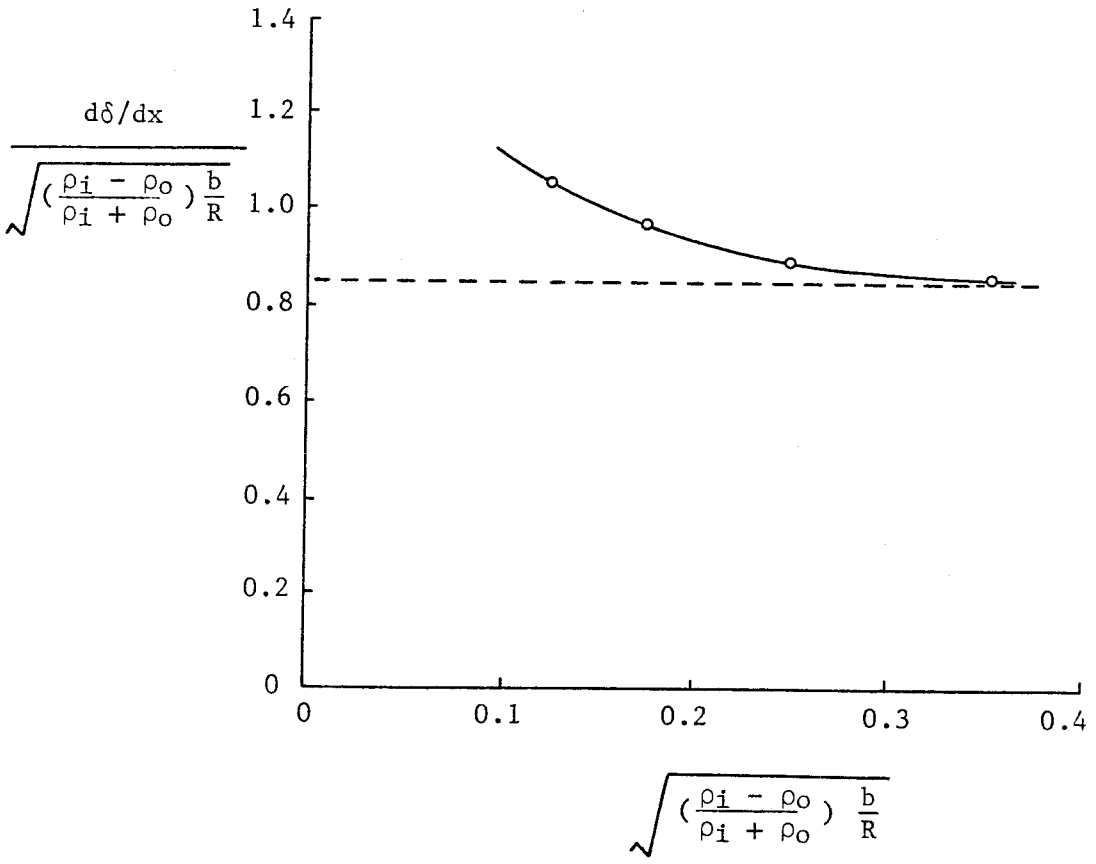

$$\frac{d\delta}{dx} \approx K \sqrt{\left(\frac{\rho_i - \rho_o}{\rho_i + \rho_o}\right)\frac{b}{R}}$$

$$K \approx 0.85$$

Fig. 7.7 The dependence of growth rate on channel curvature for a heterogeneous wake/mixing layer. The values plotted are measured from the straight portions of the thickness plots in Fig. 7.6.

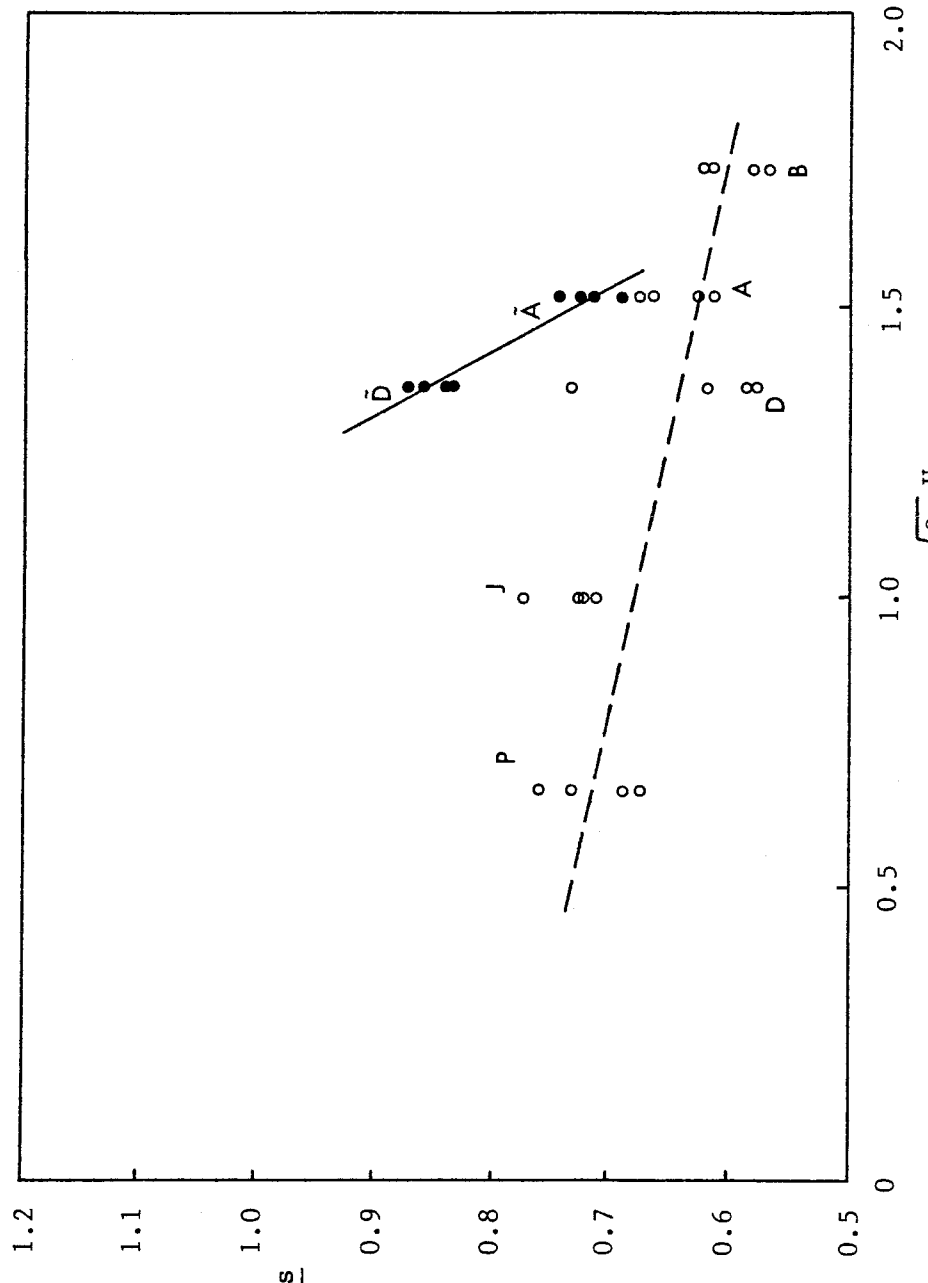

Fig. 7.8 The shape factor δ_{vis}/S for the spanwise vortices as a function of a mixed velocity-density variable.

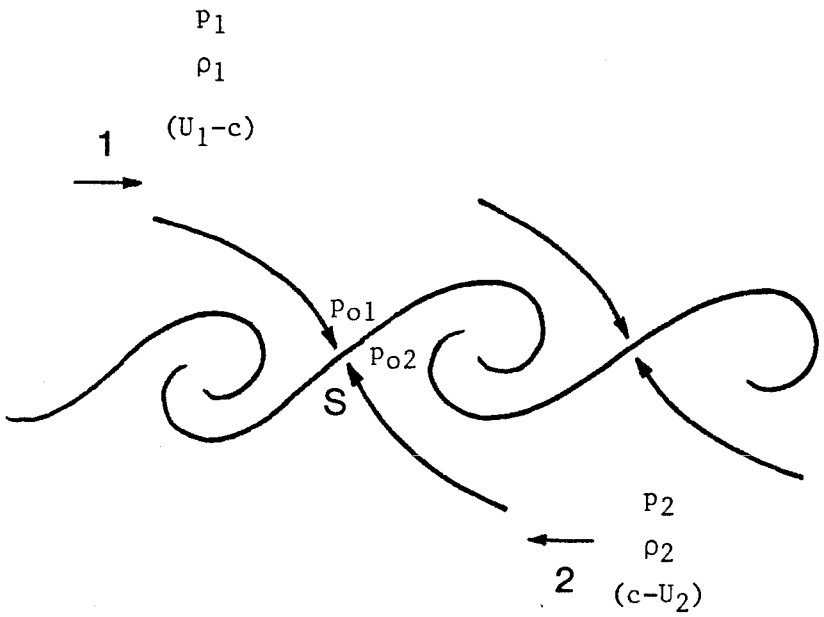

Fig. 7.9 Coles's conjecture for the topology of the spanwise vortical structure in a mixing layer. The observer is moving with the large structure, particularly the saddle point at S (Coles 1981).

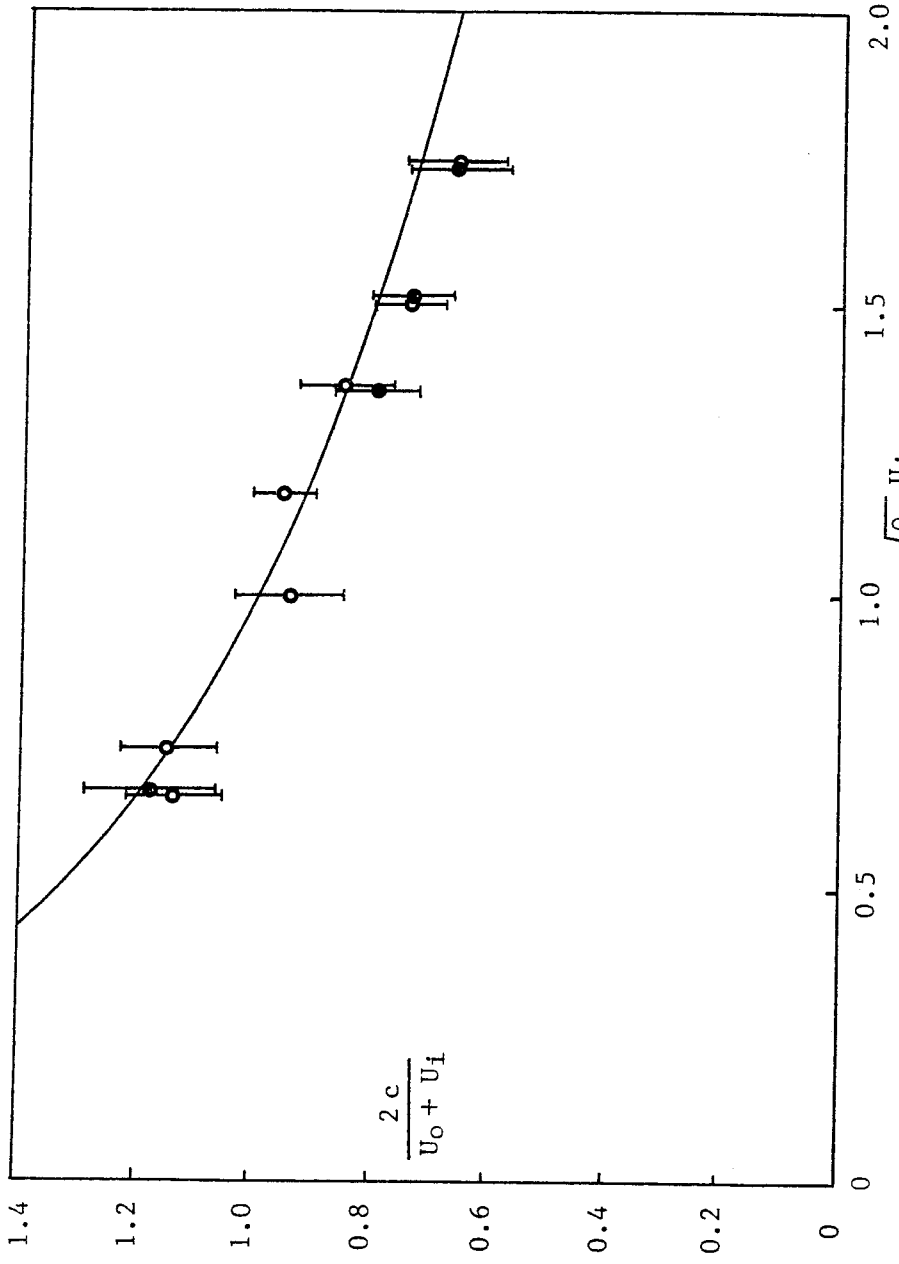

Fig. 7.10 Comparison of experimental celerity data with the formula based on Coles's conjecture. Open (closed) symbols refer to flows which are stable (unstable) according to the Rayleigh-Synge criterion.

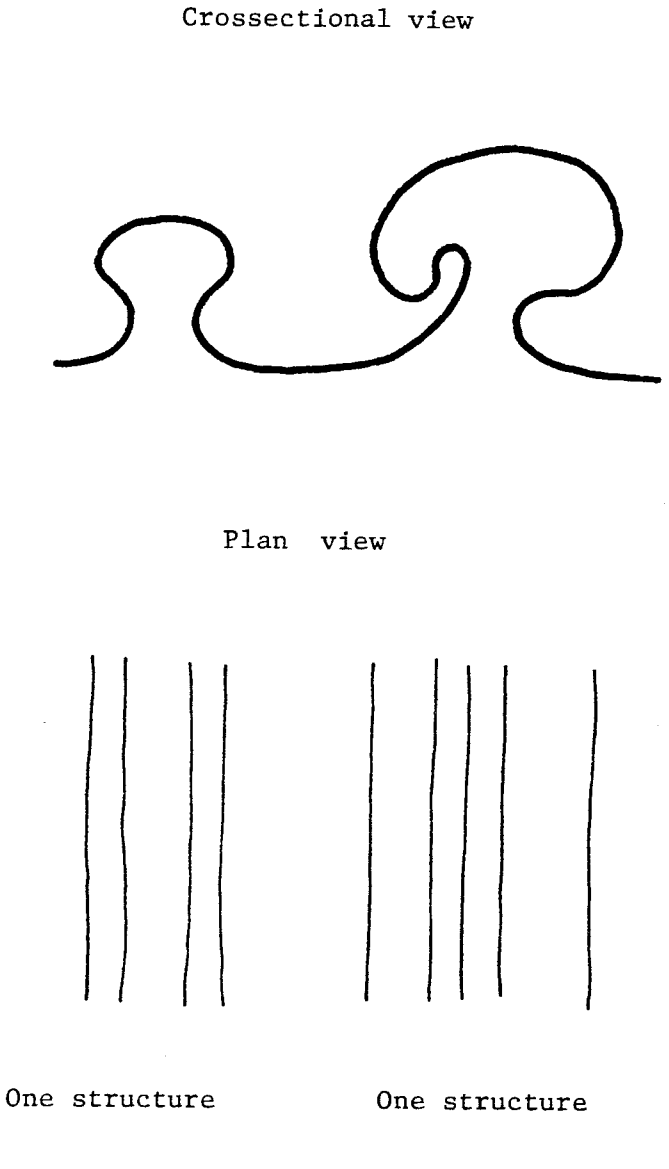

Fig. 7.11 Guide to interpretation of shadowgraph pictures of the streamwise structure in a mixing layer.

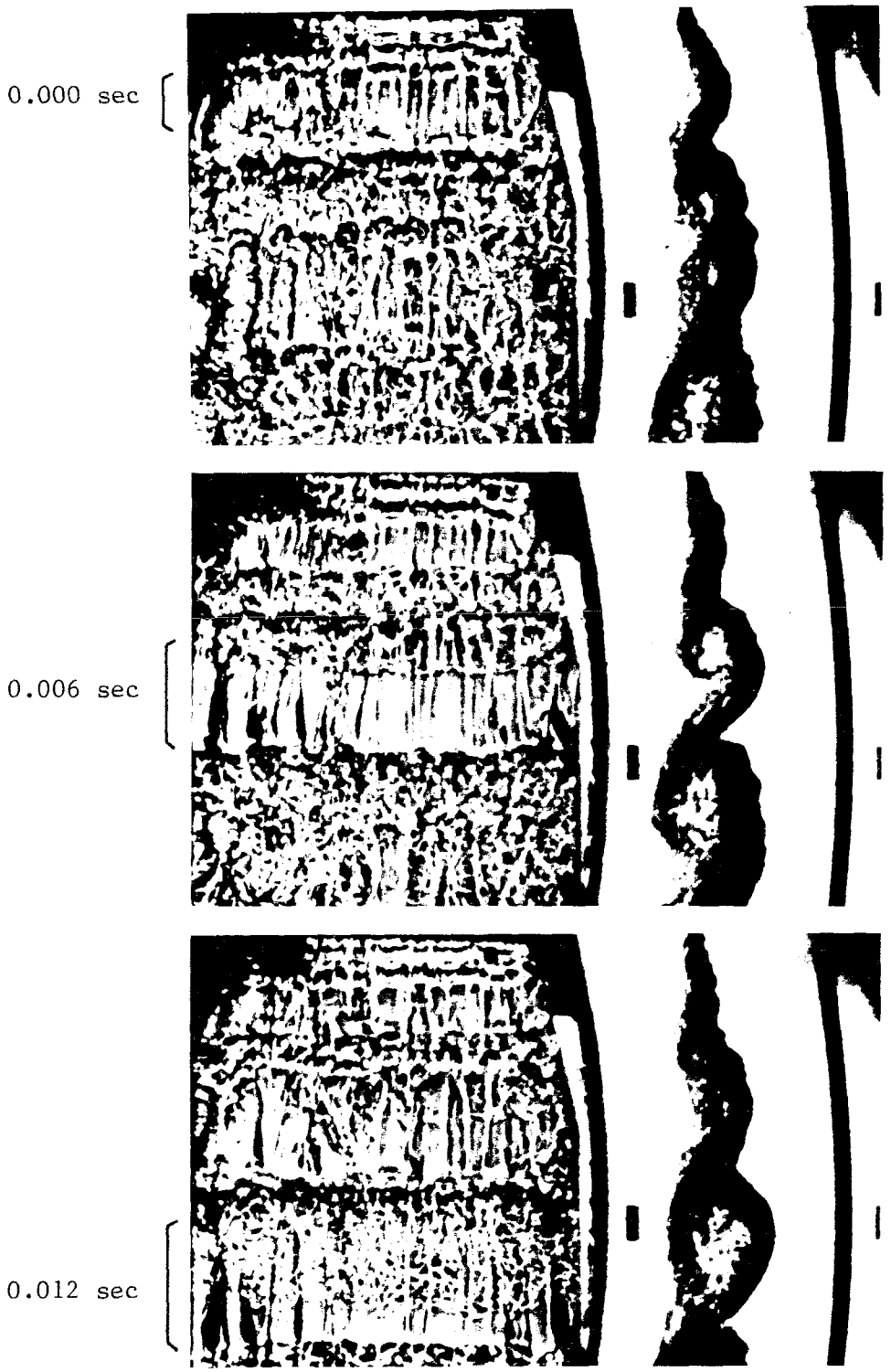

Fig. 7.12 Flow A. U_o/U_i = 0.38, ρ_o/ρ_i = 7/1. Evolution of the streamwise structures. Three non-adjacent frames from the high-speed movie.

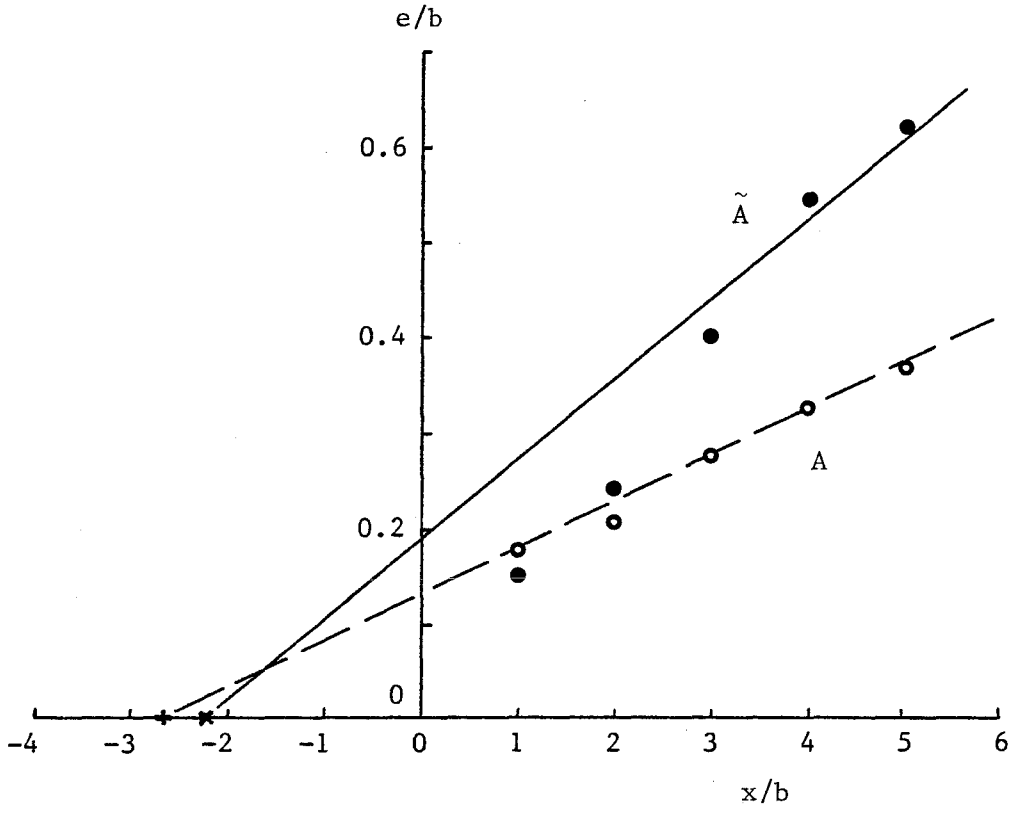

\+ virtual origin for flow A, based on profile measurements

× virtual origin for flow $\tilde{A}$, based on profile measurements

Fig. 7.13 (a) The spacing of visible streamwise structures as a function of dimensionless downstream distance. Both e and x are nondimensionalized by b, the half height of the channel.

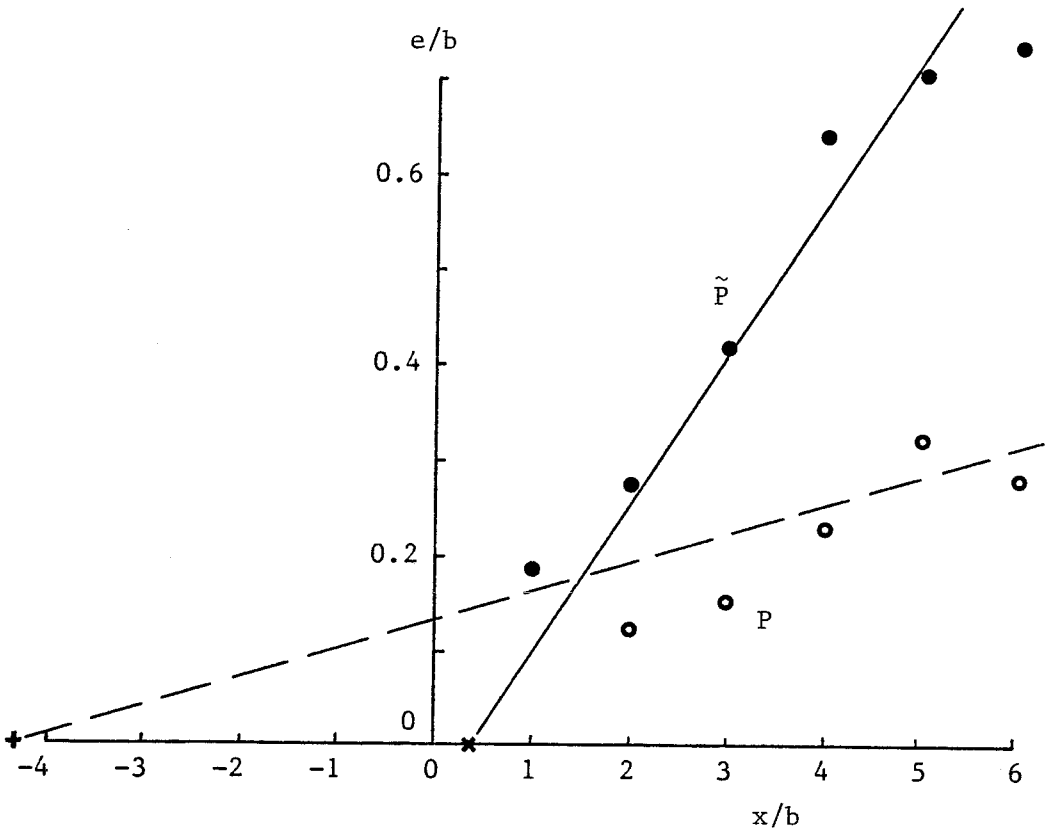

+ virtual origin for flow P, based on profile measurements

× virtual origin for flow $\tilde{P}$, based on profile measurements

Fig. 7.13 (b) For title, see Fig. 7.13 (a).

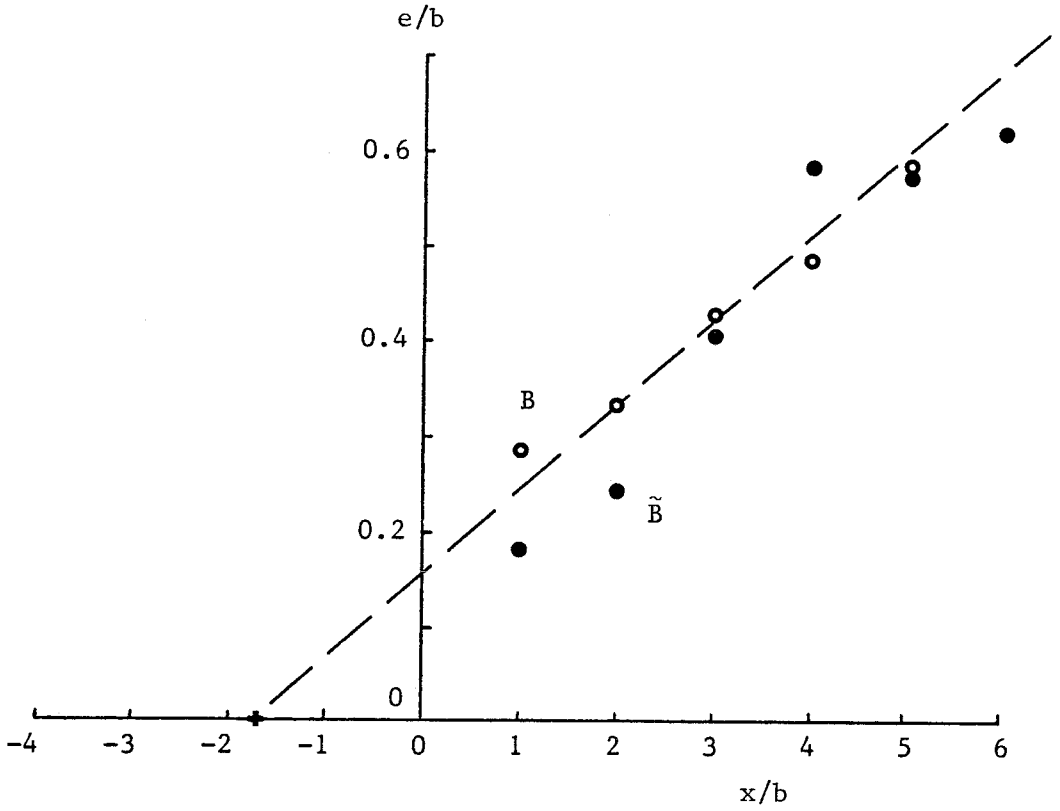

\+ virtual origin for flow B, based on profile measurements

Fig. 7.13 (c) For title, see Fig. 7.13 (a).

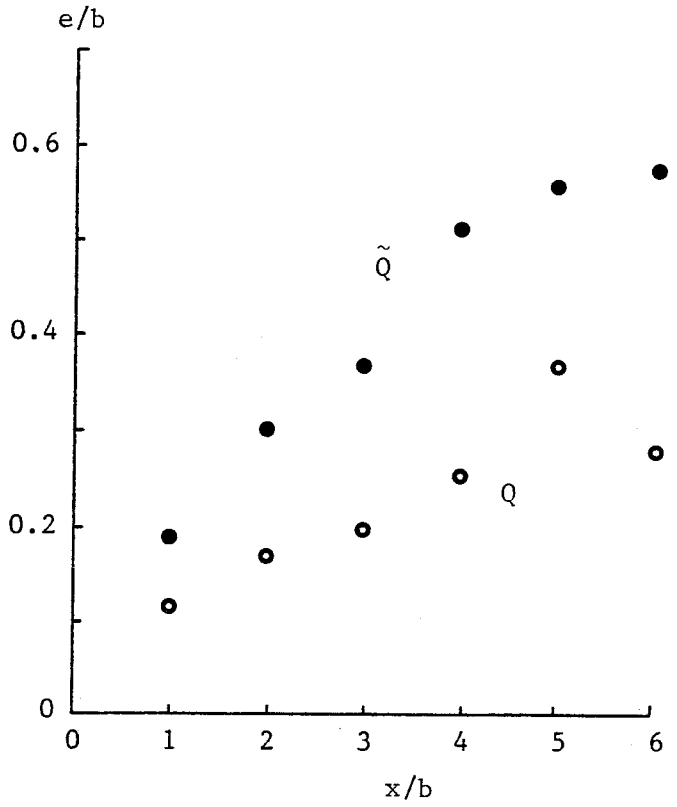

Fig. 7.13 (d) For title, see Fig. 7.13 (a).

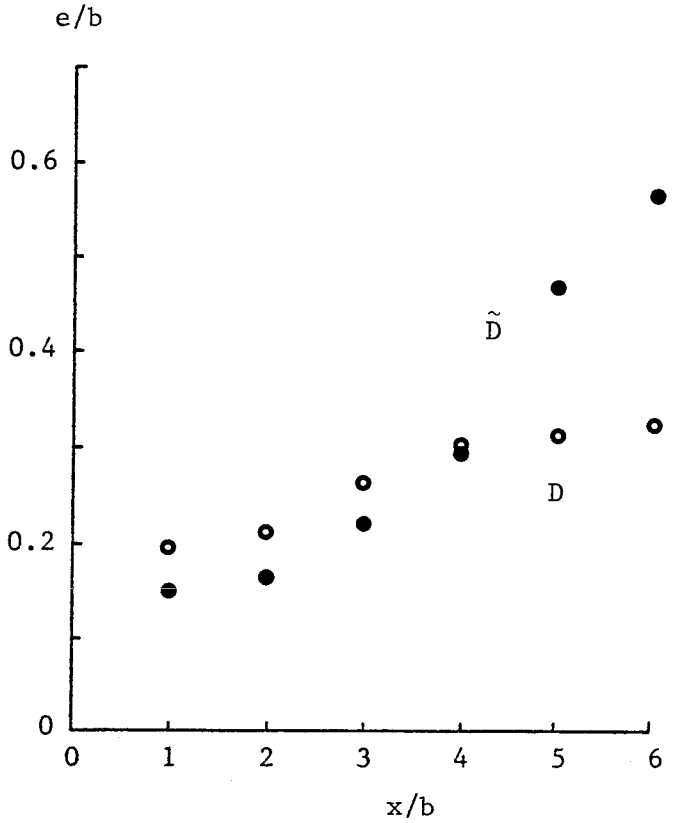

Fig. 7.13 (e) For title, see Fig. 7.13 (a).

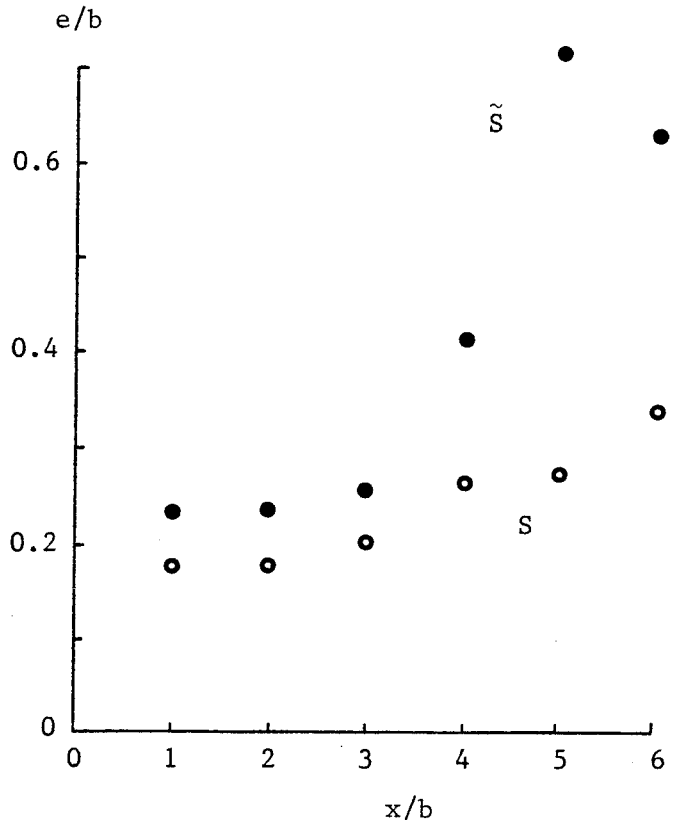

Fig. 7.13 (f) For title, see Fig. 7.13 (a).

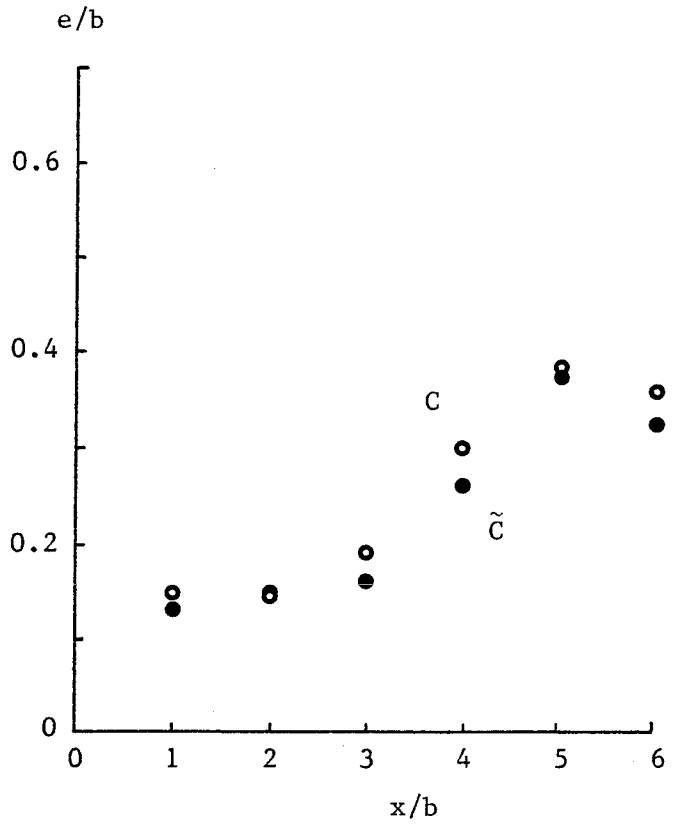

Fig. 7.13 (g) For title, see Fig. 7.13 (a).

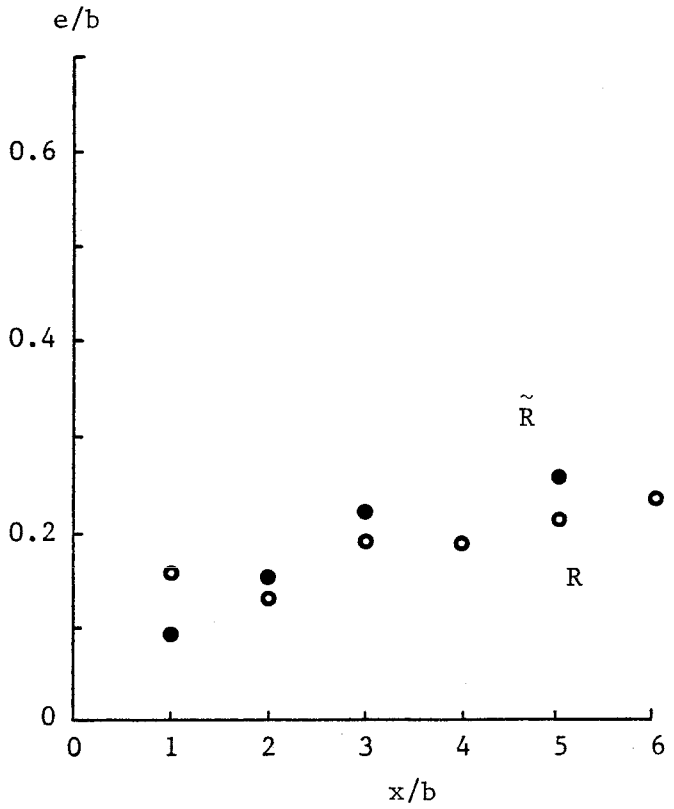

Fig. 7.13 (h) For title, see Fig. 7.13 (a).

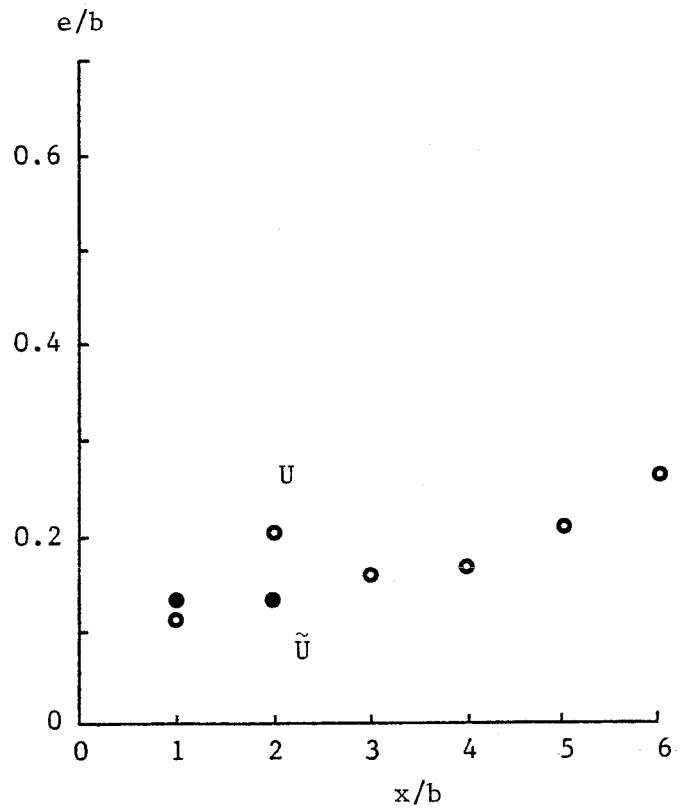

Fig. 7.13 (i) For title, see Fig. 7.13 (a).

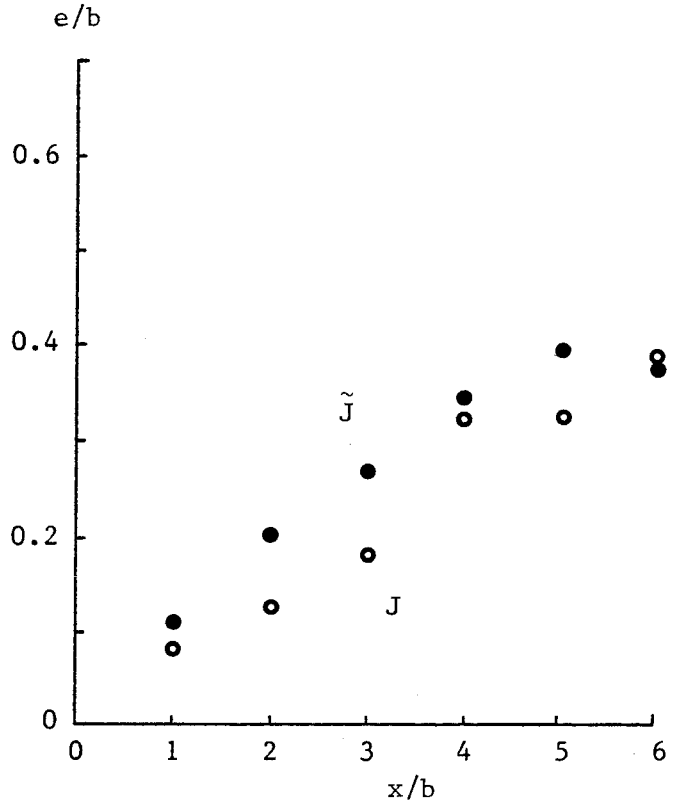

Fig. 7.13 (j) For title, see Fig. 7.13 (a).

Run	Stills U_o/U_i (cm/sec)	Movies U_o/U_i (cm/sec)	U_o/U_i	ρ_o/ρ_i	Celerity (cm/sec)
B	210/830	380/1500	0.25	7	626 ± 84
A	380/1000	380/1000	0.38	7	514 ± 41
D	620/1240	380/760	0.50	7	486 ± 47
C	1440/2060	380/543	0.70	7	442 ± 24
U	400/400	400/400	1.00	7	
R	2060/1440	543/380	1.43	7	
S	1240/620	760/380	2.00	7	652 ± 46
P	1000/380	1000/380	2.63	7	782 ± 55
Q	830/210	1500/380	3.95	7	
I	830/210	1500/380	3.95	1	
J	1000/380	1000/380	2.63	1	650 ± 66
K	1240/620	760/380	2.00	1	
L	2060/1440	543/380	1.43	1	
M	400/400	400/400	1.00	1	
$\tilde{L}$	1440/2060	380/543	0.70	1	
$\tilde{K}$	620/1240	380/760	0.50	1	
$\tilde{J}$	380/1000	380/1000	0.38	1	
$\tilde{I}$	210/830	380/1500	0.25	1	
$\tilde{Q}$	210/830	380/1500	0.25	1/7	
$\tilde{P}$	380/1000	380/1000	0.38	1/7	811 ± 80
$\tilde{S}$	620/1240	380/760	0.50	1/7	
$\tilde{R}$	1440/2060	380/543	0.70	1/7	
$\tilde{U}$	400/400	400/400	1.00	1/7	
$\tilde{C}$	2060/1440	543/380	1.43	1/7	
$\tilde{D}$	1240/620	760/380	2.00	1/7	454 ± 39
$\tilde{A}$	1000/380	1000/380	2.63	1/7	511 ± 48
$\tilde{B}$	830/210	1500/380	3.95	1/7	628 ± 85

Table 1. List of experimental conditions and celerity data. The reference velocities U_o and U_i are measured at the exit of the nozzles. All experiments are carried out at 4 atmospheres.